UNIVERSITY OF LATVIA
FACULTY OF PHYSICS AND MATHEMATICS

Andris Anspoks

STUDIES OF LOCAL STRUCTURE RELAXATION IN NANOMATERIALS

Doctoral Thesis

Promotion to the Degree of Doctor of Physics
Subbranch: Solid State Physics

Scientific advisor:
Dr. phys. **Aleksejs Kuzmins**

Riga 2014

This work has been supported by the European Social Fund within the project Support for Doctoral Studies at University of Latvia

Type of the thesis: **Doctoral thesis**
Scientific advisor: *Dr. phys.* **Aleksejs Kuzmins**

Reviewers:

Dr. **Manfred Dubiel**, Privatdozent (PD), Institut für Physik, Martin-Luther-Universität Halle-Wittenberg, Germany

Dr. phys. **Vyacheslavs Kashcheyevs**, Senior Researcher, University of Latvia

Dr. habil. phys. **Donats Millers**, Senior Researcher, Institute of Solid State Physics, University of Latvia

The defense of the doctoral thesis will take place in an open session of the Doctoral Committee of Physics, University of Latvia on **25 of April, 2014, at 16:30** in the conference hall of the Institute of Solid State Physics, University of Latvia.

The doctoral thesis and its summary are available at the Library of the University of Latvia (4 Kalpaka Blvd, Riga) and Latvian Academic Library (10 Rupniecibas Str, Riga).

Chairperson of the Specialized Promotion Council of the scientific section of the Physics at the University of Latvia: *Dr. habil. phys.* **Linards Skuja**.

To my wife Ilze

Acknowledgements

I am grateful to my supervisor Dr. Alexei Kuzmin who guided me during the whole period of my PhD studies and provided great atmosphere for our scientific research. I would like to thank Dr. Juris Purans for his helpful discussions and advices throughout the research.

I would like to thank my family, especially my wife Ilze for support of my return to the science.

I would like to thank Dr. Andris Sternbergs for inviting me in the Institute of Solid State Physics again.

Abstract

The X-ray absorption spectroscopy is a unique tool for direct local structure determination which is suitable for any material starting from bulk crystals ending with nanomaterials, liquids and gasses.

In this study we have applied the extended x-ray absorption fine structure (EXAFS) spectroscopy to probe the atomic structure of nanocrystalline NiO, $CoWO_4$, $CuWO_4$ and PbS. We have compared the atomic structure of these nanomaterials with that of the corresponding bulk compounds, in order to identify the atomic structure relaxation (changes in atomic structure) caused by a reduction of the particle size down to nanoscale.

We have adopted a recently developed complex modeling approach, combining *ab initio* multiple-scattering EXAFS calculations with classical molecular dynamics (MD), further referenced as MD-EXAFS, to the nanomaterials. The advantage of the MD-EXAFS method is a significant reduction of a number of free model parameters, which are required to describe the structure and dynamics of nanoobjects. Thus, a set of the parameters is restricted to that related to the geometry of the nanoobject and to the force-field model utilized in the MD simulations. The novel approach has been tested on NiO nanoparticles and thin films. The obtained results allowed us to identify the amount and the role of the Ni vacancies in the structure relaxation of NiO.

Contents

List of Figures xiii

List of Tables xxi

Glossary xxiii

1 Introduction 1

1.1 Motivation . . . 1
1.2 Aim and objectives of the work . . . 2
1.3 Scientific novelty of the work . . . 3
1.4 Author's contribution . . . 4
1.5 Contents of the thesis . . . 4

2 Atomic structure of nanomaterials: an overview 7

2.1 Metals, metal oxides and other compounds . . . 7
2.2 State of the art in the atomic structure analysis of nanoobjects . . . 11

3 X-ray absorption spectroscopy 13

3.1 Basics of X-ray absorption . . . 13
3.2 Gaussian approximation . . . 17
3.3 Cumulant approximation . . . 20
3.4 Radial distribution function reconstruction . . . 20

4 EXAFS data analysis and simulations 23

4.1 Extraction of EXAFS data . . . 23
4.2 Conventional EXAFS analysis in the single-scattering approximation . . . 25
4.3 Advanced methods for EXAFS data analysis . . . 29

4.4 MD-EXAFS approach for bulk crystals and nanoparticles 31
4.4.1 Development of the nanoparticle model 31
4.4.2 Details of the MD-EXAFS modeling 33
4.4.3 Details of the MD and EXAFS calculations 35

5 Experimental **37**
5.1 Sample preparation 37
5.2 X-ray powder diffraction 38
5.3 Scanning electron microscopy 38
5.4 Micro-Raman spectroscopy 38
5.5 X-ray absorption spectroscopy 38

6 Results and Discussion **41**
6.1 Local structure of microcrystalline and nanosized NiO 41
6.1.1 XRD studies of NiO nanoparticles and surface morphology of thin films 44
6.1.2 X-ray absorption spectroscopy 45
6.1.2.1 XANES 45
6.1.2.2 Conventional analysis of the EXAFS data 48
6.1.2.3 Modeling of NiO crystal and ideal nanoparticles with MD-EXAFS 55
6.1.2.4 Modeling of NiO nanoparticles with nickel vacancies . . 62
6.1.3 Conclusions 70
6.2 Microcrystalline and nanosized $MeWO_4$ 71
6.2.1 X-ray diffraction 75
6.2.2 Raman scattering spectroscopy 76
6.2.3 X-ray absorption spectroscopy 77
6.2.4 Discussion 81
6.2.5 Conclusions 82
6.3 Microcrystalline and nanosized PbS 83
6.3.1 X-ray absorption spectroscopy 83
6.3.2 Conclusions 88

7 Conclusions **89**

Main theses 91

Bibliography 93

Author's publication list 103

Participation in conferences 105

Participation in schools with posters 107

List of Figures

2.1 Lattice parameter dependence on nanoparticle diameter D for gold nanoclusters [4] (upper panel) and $BaTiO_3$ [39] (lower panel). As one can see, oxides have different behaviour compared with metals. 8

3.1 Photon absorption cross-section components and total attenuation for Ni atom (on the left) and W atom (on the right). K is the absorption edge due to the electron transitions from the core 1s level, L is the absorption edge for 2s and 2p levels, and M is that for 3s, 3p, 3d levels [48]. 14

3.2 (Upper panel) The experimental x-ray absorption spectrum (μ) at the Ni K-edge in microcrystalline NiO. (Lower panel) Ni K-edge EXAFS spectrum $\chi(k)k^2$ extracted from the experimental absorption coefficient shown in the upper panel. 15

3.3 The mean free path $\lambda(E)$ of photoelectron depending on the energy for the Ni K-edge including the core-hole effect. $\Gamma_{\mathrm{core-hole}}$ is the core-hole broadening parameter [22]. 18

4.1 Example of the EXAFS extraction procedure for the Ni K-edge in NiO. See text for details. 24

4.2 Theoretical Ni K-edge EXAFS spectra for NiO calculated with all multiple-scattering (MS) and only single-scattering (SS) contributions. Contirubtions from the first seven coordination shells are indicated by arrows in lower panel. As one can see from the Fourier transform (FT) of the EXAFS spectra, the multiple-scattering contributions do not contribute into the first and second coordination shell of Ni atoms. The calculations were performed without accounting for thermal damping (all MSRD parameters σ^2=0) and setting S_o^2=1. 26

4.3 The dependence of the number of scattering paths on the cluster size for NiO. Note the logarithmic scale on the number of scattering paths axis. 30

4.4 The scheme of MD-EXAFS calculations. The goal of the first stage is to find force-field (FF) parameters which give the mean values of interatomic distances for the first coordination shells being in agreement with those obtained from the conventional analysis of the experimental EXAFS spectrum or other structural analysis. Only those model nanoparticles which give this agreement within the desired precision are passed to the second step. The goal of the second step is to fine-tune FF parameters in order to minimize the residual between configuration-averaged multiple-scattering EXAFS spectrum of the model nanoparticle and experiment. One should find the model nanoparticle which gives the minimal residual value. After second phase one can use MD data to find all necessary properties of the selected model nanoparticle. 32

4.5 The calculated distance R(Ni–O_1) between the atoms in the first coordination shell of NiO model nanoparticle as a function of the Ni ion charge Z_{Ni}. Force-field parameters used in MD calculations come from [32]. Line represents linear fit of the modeled data. 34

5.1 Schematic view of the EXAFS experiment at C beamline DORIS III storage ring. The setup consists of the x-ray source (the storage ring), variable entrance and exit slits, double-crystal monochromator, three ionization chambers (I1, I2 and I3), beam stopper. The position of the unknown and reference samples and the optional fluorescence detector (not used in the present work) are also shown (http://www.hasylab.de). 39

6.1 Dependence of the unit cell volume on the nanoparticle size (data taken from XRD studies, solid circles from [113], empty circles from [114], empty box from [115], solid triangles from [116]). Dashed line corresponds to the fitted formula $V = V_0 + A\exp(-L/B)$, where V is the unit cell volume (in Å^3), L is the particle size (in nm), $V_0 = 72.874$ Å^3, $A = 3.9419$ Å^3, B =3.8009 nm. 42

6.2 Left panel: XRD patterns of NiO nanopowder (nano-NiO) and microcrystalline NiO (c-NiO). Right panel: XRD patterns of $Ni_{1-x}O$ thin films prepared at three Ar/O_2 gas ratios equal to 0/100 (TF1), 50/50 (TF2) and 90/10 (TF3). 45

6.3 SEM images of $Ni_{1-x}O$ thin films with Ar/O_2=90/10 simultaneously sputtered on (a) silicon, (b) glass and (c) polyimide film. 45

6.4 Upper panel: Experimental Ni K-edge XANES in c-NiO (solid lines), nano-NiO (blue dashed lines) and TF3 (red dotted line) at 300 K. The position of the pre-edge peak A (quadrupole transition to 3d(Ni)) and next feature B (dipole transition to hybrid 4p(Ni) and 3d($Ni_{4th\ shell}$)) are indicated by arrows. Lower panel: enlarged region of the pre-edge peak A. 47

6.5 Low temperature (T = 10 K) Ni K-edge EXAFS spectra $\chi(k)k^2$ and their Fourier transforms (FTs) for c-NiO, nano-NiO and TF3. There is noticeable signal damping upon a decrease of the size of particles (going from c-NiO to nano-NiO and, next, to TF3). Note also a small shift of the peak positions in FTs to larger distances upon a decrease of the particle size. 49

6.6 The Ni K-edge EXAFS spectra $\chi(k)k^2$ for nano-NiO at selected temperatures. Thermal disorder is responsible for the oscillation damping at high-k values. 50

6.7 Theoretical Ni K-edge EXAFS spectra for c-NiO calculated using all multiple-scattering (MS) contributions and only single-scattering (SS) contributions. These calculations were performed without accounting for thermal damping (all MSRD parameters $\sigma^2 = 0$) and setting $S_o^2 = 1$. As one can see from the comparison of Fourier transforms, the MS contributions are not present in the first and second coordination shells of Ni atoms. 50

6.8 Temperature dependence of the mean-square relative displacements (MSRD) $\Delta\sigma^2 = \sigma^2(T) - \sigma^2(\text{c-NiO}, T = 6\text{ K})$ for the first (Ni–O_1) and second (Ni–Ni_2) coordination shells in c-NiO, nano-NiO and TF3 relative to the MSRD value in c-NiO at $T = 6$ K. The Debye models are shown by lines. See text for the values of the characteristic Debye temperatures. 51

6.9 Temperature dependence of the average interatomic distances in the first (Ni–O_1, labeled with full markers) and second (Ni–Ni_2 labeled with open markers) coordination shells of nickel in c-NiO (squares), nano-NiO (circles) and TF3 (triangles). 52

6.10 Dependence of the average coordination number N_{Ni_2} in the second shell of nickel on the cubic nanoparticle size ($L = la_0$). The parameters for nanocrystalline samples are indicated. The inset shows the relaxed nanoparticle model with $l = 3$ ($3 \times 3 \times 3$ unit cells). 54

6.11 Example of the single MD snapshot of a nanoparticle with the size $l =$ 9 unit cells. Small red balls represent oxygen atoms, large gray balls represent nickel atoms. 56

6.12 Experimental Ni K-edge EXAFS spectra for microcrystalline NiO (c-NiO) compared with the model spectra, obtained using MD-EXAFS procedure described in Sec. 4.4 and the optimized value of the nickel ion charge Z_{Ni}=+2.015. 57

6.13 Experimental Ni K-edge EXAFS spectra for nano-NiO compared with the model spectra of the ideal nanoparticle (no vacancies) with ion charges used from the bulk NiO model (Z_{Ni}=+2.0 and Z_{O}=-2.0) and optimized ones (Z_{Ni}=+1.95 and Z_{O}=-1.95, obtained using MD-EXAFS procedure described in Sec. 4.4. The size of the model nanoparticle is 6×6×6 unit cells. 58

6.14 The dependence of the residual between the experimental and MD-EXAFS signals (see Sec. 4.4 for detailes of calculations) on the nanoparticle size equal to the $l \times l \times l$ unit cells. The results for the two series of simulations are shown: red squares are for NiO nanocrystalline powder (nano-NiO) and blue triangles are for NiO thin film (TF1) sputtered in pure oxygen atmosphere. In both cases, there is a clear minimum at l=8 for nano-NiO and at l=5 for TF1. 61

6.15 Schematic view of the nearest-neighbor relaxation around nickel vacancy in the bulk of nickel oxide according to our molecular dynamics simulations. Note that oxygen atoms move outwards, but nickel atoms move inwards to the nickel vacancy. 63

6.16 The dependence of the residual modulus value $|\Delta R(\text{Ni–O}_1)|$ between the first shell interatomic distances, obtained for cubic NiO nanoparticles by conventional analysis method (Fig. 6.9) and from the MD simulation, on the nickel vacancy concentration C_{vac} and on the nanoparticle size L=Na_0 under imposed requirement that the second shell interatomic distance $R(\text{Ni–Ni}_2)$ should coincide with the value, obtained by the conventional modeling procedure (Fig. 6.9) within ±0.001 Å. 65

6.17 Comparison of the experimental (solid lines) and configuration-averaged (dashed lines) Ni K-edge EXAFS spectra $\chi(k)k^2$ and their Fourier transforms (FTs) for nano-NiO and TF3. The theoretical data correspond to the nanoparticle models which give the best fit to the experimental spectra (nano-NiO: N=9 corresponding to L ≈3.6 nm, C_{vac}=0.4% corresponding to 12 vacancies, Z_{Ni}=+1.976, Z_{O}=–1.968; tf-NiO: N=4 corresponding to L ≈1.5 nm, C_{vac}=1.6% corresponding to 4 vacancies, Z_{Ni}=+1.925, Z_{O}=–1.895). 67

6.18 Crystal structure of $CoWO_4$. Red balls represent oxygen atoms, green balls - tungsten atoms, and blue balls - cobalt atoms. Co and W atoms are surrounded by six oxygen atoms, forming distorted octahedral coordination. Metal–oxygen octahedra of one type share edges and form zig-zag chains along the c-axis. Metal–oxygen octahedra of different type share single oxygen atom. 73

6.19 X-ray diffraction (XRD) patterns of microcrystaline and nanoscale $CuWO_4$ and $CoWO_4$. 75

6.20 Left panel: Raman scattering spectra of microcrystaline and nanocrystaline $MeWO_4$ (Me = Co, Ni, Cu, Zn) powders. The position of the main band at 955 cm^{-1} in nanosized tungstates is indicated by dashed vertical line. Measurements were performed at 20°C. Right panel: the dependence of the main Raman band for microcrystaline $MeWO_4$ from the type of the Me atom. 76

6.21 The experimental W L_3 and Co(Cu) K edge EXAFS spectra $\chi(k)k^2$ and their Fourier transforms for microcrystalline and nanocrystaline $CoWO_4$ and $CuWO_4$ at $T = 300$ K. Both modulus and imaginary parts of FTs are shown. Note that the positions of the FT peaks in Fig. 6.21 are shifted from their true crystallographic values because the FTs were calculated without phase-shift corrections. 78

6.22 The experimental W L_3 and Co(Cu) K edge EXAFS spectra $\chi(k)k^2$ and their Fourier transforms for microcrystalline and nanocrystaline $CuWO_4$ at $T = 10$ K and 300 K. The range of the first coordination shell is indicated by arrows in FTs. 79

6.23 The reconstructed RDFs $G(R)$ for the first coordination shell of tungsten and transition metals in microcrystalline (solid lines) and nanocrystaline (dashed lines) $MeWO_4$ (Me = Co, Ni, Cu, Zn). The data for $NiWO_4$ and $ZnWO_4$ are taken from [94, 184]. 80

6.24 Optical absorption spectrum of nano-PbS. The energy of the first exciton peak is about 1.63 eV. 83

6.25 Size dependence of the exciton energy on the diameter of nanosized PbS according to [195]. Arrows indicate the position of the exciton peak and the corresponding size for our nano-PbS sample. 84

6.26 The experimental Pb L_3-edge EXAFS spectra $\chi(k)k^2$ and their Fourier transforms (FTs) for c-PbS and nano-PbS at $T = 300$ K. 85

6.27 Experimental (empty circles) and best fitted Pb L_3-edge EXAFS spectra for the first two coordination shells of Pb. Solid line represents signal from RDF reconstruction and dashed line represents signal using Gaussian approximation. 87

6.28 Radial distribution function (RDF) reconstruction for c-PbS and nano-PbS obtained using theoretical phases and amplitudes. Dotted lines show RDF approximation with the Gaussian shape obtained by the standard EXAFS fitting procedure for the first two coordination shells. 87

List of Tables

2.1 Experimental probes of nanoscale structure from [1]. 12

6.1 Values of the structural parameters for the first two coordination shells in microcrystalline NiO (c-NiO), NiO nanoparticles (nano-NiO) and NiO thin films (TF1, TF2, TF3), obtained from the best-fit of the EXAFS signals within the Gaussian approximation. N_i is the coordination number, ΔR_i (± 0.002 Å) is the interatomic distance relative to c-NiO, $\Delta\sigma_i^2$ (± 0.0003 Å^2) is the MSRD relative to c-NiO, a_0 is the lattice parameter ($a_0 = \sqrt{2}R_2$), V is the unit cell volume calculated from a_0 ($V = a_0^3$), which allows to estimate the particle size $L(V)$ according to Eq. 6.2. For reference c-NiO a_0 is equal to 4.17693 Å and $V_0 = 72.874$ Å^3. 53

6.2 Force-field model parameters of the Buckingham potentials for the Ni–O and O–O atom pairs used in the molecular dynamics simulations. . . . 56

6.3 The size L of the NiO nanoparticles, estimated from EXAFS and XRD data. $L = la_0$ where l is the number of unit cells and a_0 is the lattice parameter. C_{vac} is the concentration of nickel vacancies. $L(N_{\text{Ni2}})$ is the particle size estimated from conventional EXAFS analysis using the Ni second shell coordination numbers and assuming cubic shape of the nanoparticles (Fig. 6.10). $L(V)$ is the particle size estimated using Eq. 6.2 and the second shell radius $R_2(\text{Ni} - \text{Ni}_2)$. $L(\text{Scherrer})$ is the particle size estimated from XRD data using Scherrer method. 66

6.4 Structural parameters (CN is the coordination number, R is the interatomic distance, and σ^2 is the MSRD) for the first six coordination shells in c-NiO, nano-NiO and TF3, calculated by decomposition of the Ni–O and Ni–Ni pair distribution functions, obtained at 300 K, into Gaussian components. 69

6.5 Relative to c-NiO values of the structural parameters (CN is the coordination number, R ($\pm$0.002 Å) is the interatomic distance, and σ^2 ($\pm$0.0003 Å^2) is the MSRD) for the first two coordination shells in nano-NiO and TF3, obtained from the best-fit of the EXAFS signals within the Gaussian approximation (Figs. 6.8 and 6.9) and from the MD-EXAFS analysis (Table 6.4). 70

6.6 Structural parameters (N is the coordination number ($\pm$0.5), R is the interatomic distance ($\pm$0.01 Å), and σ^2 is the mean-square relative displacement (MSRD) ($\pm$0.001 Å^2)) for the first two coordination shells in c-PbS and nano-PbS at $T = 300$ K, calculated by decomposition of the Pb–S and Pb–Pb pair distribution functions into Gaussian components. 86

Glossary

BFT	Back-Fourier transformation
EXAFS	Extended x-ray absorption fine structure
FF	Force-field
FT	Fourier transformation
FWHM	Full width half maximum
MC	Monte Carlo
MD	Molecular dynamics
MS	Multiple scattering
MSD	Mean square displacement
MSRD	Mean square relative displacement
PDF	Pair distribution function
PRDF	Partial radial distribution function
RDF	Radial distribution function
RMC	Reverse Monte Carlo
SS	Single scattering
XANES	X-ray absorption near edge structure
XAS	X-ray absorption spectroscopy
XPS	X-ray photoemission spectroscopy
XRD	X-ray diffraction

1

Introduction

1.1 Motivation

Nanomaterials are used in a broad range of applications, for example, in sensors, catalysts, fuel-cells, energy harvesting, nano-electronics, optoelectronic and photonics devices. It was noticed that physical properties of nanomaterials are different compared with that in the bulk. Since it is well known that most of the properties are determined by atomic structure, it is important to have an access to precise structural information for nanomaterials, which is challenging task [1].

Scientists have been studying structure of nanomaterials for more than 40 years. It was noticed that in metallic nanoparticles the interatomic distances decrease with decreasing the size of the particle [2, 3, 4, 5]. Such behavior is consistent with the predictions of the classical physics [6], stating that surface tension should increase with decreasing of the particle diameter. Thus, increasing surface tension creates more pressure to the particle volume that leads to the decreasing of the interatomic distances.

At the same time metal oxides and other metal nanomaterials possess opposite behavior, their interatomic distances increase with decreasing size of nanoparticles [7, 8, 9, 10]. Different mechanisms have been proposed to explain this phenomena [11, 12, 13], but still the question, why metals and metal compounds show different behavior, is open.

In this context, the accurate determination of the changes in atomic structure in nanomaterials is very important. Information about atomic structure allows to validate theoretical models for existing nanomaterials and predict new nanomaterials with

desired properties.

Different experimental techniques have developed to study nanomaterials [1, 14, 15], but only two methods, namely total scattering [16, 17] and x-ray absorption spectroscopy [18, 19], provide with direct access to the structural information.

The advantage of x-ray absorption spectroscopy is its chemical element selectivity, sensitivity to low element concentration and scalability down to nanoparticles and even molecules [20, 21, 22]. It allows to extract information on the local atomic structure around the absorbing atom including distances and mean-square relative displacements (MSRD).

1.2 Aim and objectives of the work

The aim of this work was to study changes in atomic structure (structure relaxation) that happen upon decreasing the size of the materials to nanoscale.

In particular, we have studied structure relaxation in nanocrystalline nickel oxide (NiO), tungstates ($MeWO_4$, Me = Co, Cu) and lead sulfide (PbS) using extended X-ray absorption fine structure (EXAFS) experimental data.

In this work we have adopted a recently developed complex modeling approach [23, 24], combining *ab initio* EXAFS calculations [22, 25] with classical molecular dynamics (MD), further referenced as MD-EXAFS, to the nanomaterials [26, 27]. The advantage of the MD-EXAFS method is a significant reduction of a number of free model parameters, which are required to describe the structure and dynamics of nanoobjects [23, 26]. The only parameters we need are related to the geometry of the nanoobject and to the force-field model used in the molecular dynamics simulations. All interatomic distances, bond angles, thermal and static disorder effects are obtained from MD simulations by calculating configuration averages from snapshots of instant atomic positions.

We have tested MD-EXAFS on nanocrystalline NiO and have reconstructed structural and dynamic information from experimental Ni K-edge EXAFS spectra up to the eighth coordination shell of nickel in nanocrystalline NiO taking into account the presence of defects, thermal disorder and structure relaxation in nanoparticles [26, 27].

1.3 Scientific novelty of the work

Conventional EXAFS data analysis is restricted by the photoelectron single-scattering approximation [28], which limits the obtained structural information with only the first or, in some cases, also the second coordination shell of the absorbing atom. At the same time, standard fitting procedure, including photoelectron multiple-scattering processes [29, 30], employs three model parameters (path degeneracy, length and MSRD) for each scattering path, that results in a huge number of correlated parameters rapidly exceeding the maximum number of the allowed independent parameters.

Recently developed MD-EXAFS method [23, 24] overcomes these limitations and allows one to use all information hidden in the EXAFS spectra, including all contributions from the photoelectron multiple-scattering events. Also the method requires only few force-field parameters to describe the interatomic interactions in a compound.

We have extended MD-EXAFS method to the case of nanomaterials. It allows us to account for atomic structure relaxation, thermal disorder, nanoobject size and the presence of defects. This method enables us direct comparison of experimental EXAFS spectrum with the model one taking into account all coordination shells of the absorbing atom and the multiple-scattering effects. The agreement between experimental and theoretical EXAFS spectra is used as a criterion for the force-field model reliability.

The study of the local atomic structure around nickel atoms in nickel oxide (NiO) nanocrystalline powder and thin films has been performed using Ni K-edge EXAFS and interpreted using MD-EXAFS method [26, 31, 32]. It was found that in nanocrystalline NiO there is noticeable structure relaxation, which results in an expansion of the Ni–Ni bonds and a contraction of the nearest neighbor Ni–O bonds as well as an increase of the static disorder probed by the mean-square relative displacement (MSRD). At the same time, the lattice dynamics, also probed by the MSRD, is close in both micro- and nanocrystaline NiO in the temperature range from 10 to 300 K. It was shown using the MD-EXAFS method that the structure relaxation inside NiO nanoparticles is due to the presence of Ni vacancies [26, 27].

The study of the local atomic structure around tungsten and metal atoms in $MeWO_4$ (Me = Co, Cu) nanoparticles has been performed using the W L_3-edge and Me K-edge EXAFS and Raman spectroscopy. It was found that atomic structure of nanosized $MeWO_4$ relaxes compared with microcrystalline phase, leading to large and particular

distortion of the WO_6 octahedra. In nanoparticles tungsten atoms have stronger and shorter bonds with the nearest four oxygen atoms, whereas other two oxygens become weakly bound. It is also shown that the relaxation is affected by the Me^{2+} ion type.

Pb L_3-edge EXAFS results indicate strong structure relaxation in led sulfide (PbS) nanoparticles compared to microcrystalline PbS. The analysis of radial distribution functions (RDF) for Pb–S and Pb–Pb atom pairs revealed that they have non-Gaussian shape, indicating strong anharmonic Pb–S interaction, average Pb–S distance in the first coordination shell decreases, but the average Pb–Pb distance in the second coordination shell increases. This effect is similar to that found in NiO.

1.4 Author's contribution

The majority of the work has been done at the Institute of Solid State Physics, University of Latvia. X-ray absorption spectroscopy measurements were performed at HASYLAB/DESY (Hamburg, Germany) using synchrotron radiation produced by the DORIS III storage ring.

The author has been participated in the nanopowder preparation and their characterization by Raman spectroscopy and x-ray diffraction.

The MD-EXAFS implementation for nano-compounds and corresponding computer code has been developed by the author.

The molecular dynamics simulations, the analysis of the experimental EXAFS data and the advanced modeling of EXAFS spectra (including MD-EXAFS) have been performed by the author at the Latvian SuperCluster facility LASC [33].

The results of this work have been presented at 8 international conferences and 4 international schools during 2009-2013 and discussed at the scientific seminar at the Institute of Solid State Physics, University of Latvia on April 20, 2013. Main results have been published in 6 SCI papers and 3 SCI papers are accepted, but not published yet.

1.5 Contents of the thesis

The thesis consists of seven chapters.

In order to provide context, Chapter 2 is an overview of current situation on the atomic structure relaxation research in the nanomaterials, giving an insight into the problem history and existing models for this phenomenon.

Chapter 3 gives a review of the theory of X-ray absorption, which is the main tool for our structure analysis. Here the description of the EXAFS theory is provided, including three major implementations for the data analysis: Gaussian approximation, cumulant approximation and radial distribution function reconstruction.

In Chapter 4 we describe EXAFS data analysis and simulations used to analyze experimental spectra. In the first part of the chapter we present traditional methods, including EXAFS data extraction from the X-ray absorption spectra and data analysis using the single-scattering approximation. Next we describe more advanced data analysis methods, which allow us to go beyond the single-scattering approach. Here we give details of the MD-EXAFS method implementation for nano-compounds.

In Chapter 5 we describe used samples and their preparation, as well as employed experimental techniques, including X-ray diffraction, scanning electron microscopy, micro-Raman spectroscopy and X-ray absorption spectroscopy.

Chapter 6 presents our experimental and modeling results for NiO, PbS and $MeWO_4$ nanomaterials. Here we provide the results of the conventional EXAFS analysis for all our samples and detailed MD-EXAFS based analysis for NiO samples.

The main conclusions are summarized in Chapter 7.

2

Atomic structure of nanomaterials: an overview

Physical properties of nanomaterials are often different from corresponding bulk materials [34, 35] due to changes in atomic structure (structure relaxation) originated by a reduction of the nanoparticle size [14]. In this chapter we will give an insight into available information about character of the structure relaxation in nanoobjects and existing models of this phenomenon.

The most common feature of all nanosized objects is large surface-to-volume ratio [34]. One could expect that with a decrease of the size, the surface tension increases and creates a positive pressure to the nanoparticle that results in a reduction of the inter-atomic distances [6].

2.1 Metals, metal oxides and other compounds

Inline with these predictions [6], a decrease of interatomic distances is observed in fine metallic particles, such as silver [2], copper, platinum [3] and gold [4, 5], upon a reduction of their size (see Fig. 2.1).

For some time palladium was considered as a metal with anomalous behavior, since its lattice parameter expands upon decreasing the nanoparticle size [36, 37]. This fact has created many questions and cannot be explained in the frame of the common approach for all metals. However, more careful studies by R. Lamber *et al.* [38] revealed that pure Pd obeys normal rule for metals: its lattice parameter decreases

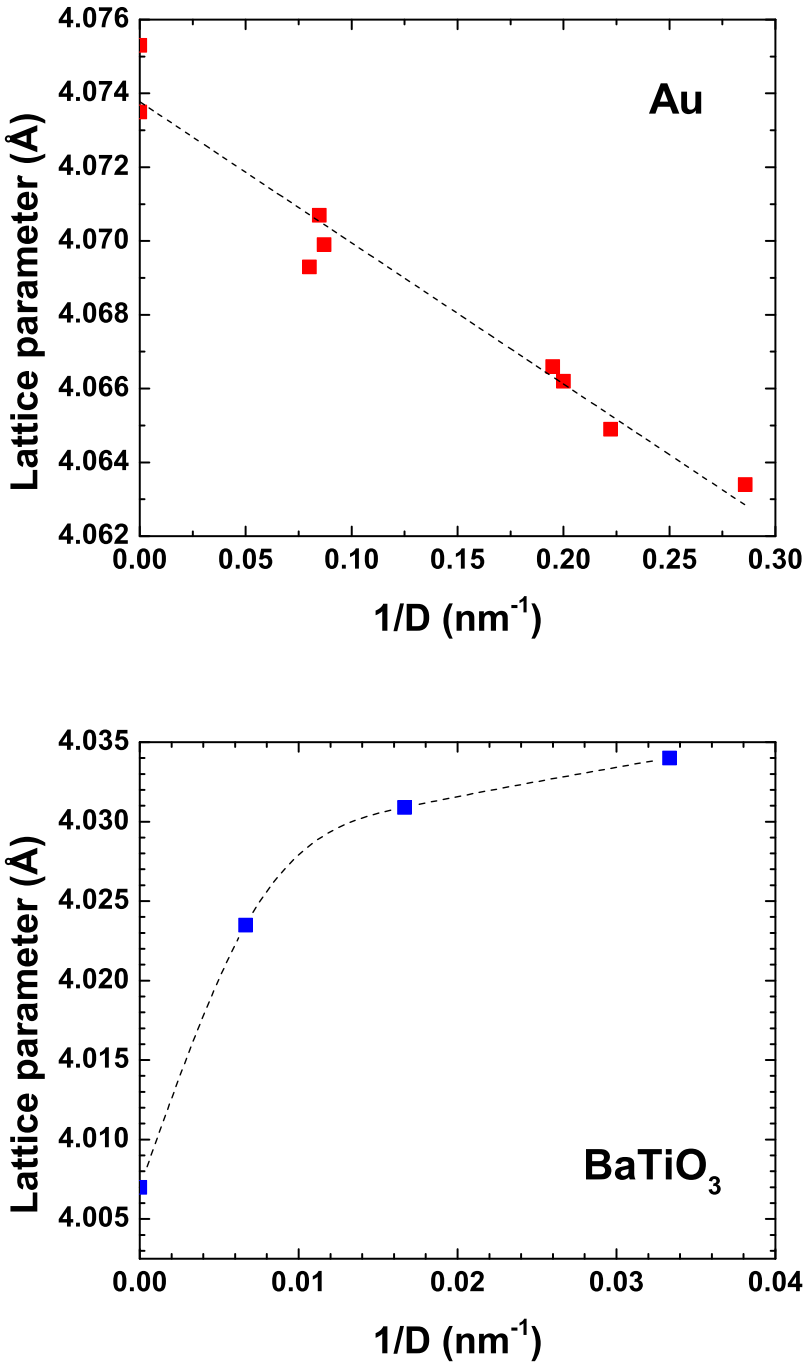

Figure 2.1: Lattice parameter dependence on nanoparticle diameter D for gold nanoclusters [4] (upper panel) and $BaTiO_3$ [39] (lower panel). As one can see, oxides have different behaviour compared with metals.

upon decreasing size of palladium clusters. Authors in [38] explain the dilation of the Pd lattice, observed in other studies [36, 37], in terms of incorporation of impurities, e.g. oxygen, hydrogen, carbon, or pseudomorphism in case of crystalline substrates. Thus, currently available information suggests that in all pure metals lattice parameter decreases upon decreasing nanoparticle size.

A size-dependent lattice dilatation was also found in silver nanoparticles (3.9 and 5.1 nm mean size) embedded in a silicate glass matrix by high-resolution electron microscopy and EXAFS spectroscopy by M. Dubiel *et al.* [40]. The effect was found to be related to a size-dependent increase of the thermal expansion coefficient, evidenced from the temperature dependence of the Ag-Ag distances [40]. Therefore, the unusual dilation behaviour was interpretation by a combination of both the particle size effects and the influence of the surrounding glass matrix [40].

In contrast to metals, some materials show opposite behavior, their lattice constant expands upon a decrease of the nanoparticle size. Such materials include most of metal oxides including complex oxides, for example: MgO [7], $BaTiO_3$ [9] (see Fig. 2.1). The same applies to other metal compounds, like TiC [8].

P. Ayyub *et al.* [10] studied a wide range of materials, such as Fe_2O_3, Al_2O_3, ZrO_2 and $BaTiO_3$, $La_{1.85}Sr_{0.15}CuO_4$, $YBa_2Cu_3O_{7-\delta}$, $Bi_2Sr_2CaCu_2O_{8+\gamma}$, and proposed a general rule: in a majority of partially covalent oxides, the unit-cell volume increases with a decrease of particle size, and the lattice gets distorted in such a way that the crystal symmetry tends to increase. In some cases the lattice distortion is large enough to induce a phase transition to a more symmetric lattice, but in most cases, there is simple size-induced reduction in an asymmetry parameter. Note that such behaviour affects many physical properties, especially phase transition temperature and other cooperative effects, such as magnetism, ferroelectricity and superconductivity.

This general rule was confirmed by x-ray diffraction (XRD) studies of copper oxide by V. R. Palkar *et al.* [41].

S. Tsunekawa *et al.* [42] observed similar behavior in XRD and transmission electron microscope (TEM) studies of $BaTiO_3$ nanoparticles, where the lattice constant increases for particles with the diameter less than 110 nm, reaching 2.5% for particles with the diameter about 15 nm. The critical size of these nanoparticles, below which the particle structure changes from the tetragonal to the cubic phase and the ferroelectric polarization is canceled, was determined to be 80 nm [11].

Other studies, done by T. C. Huang *et al.* [39], confirm that upon decreasing particle size from 140 nm to 30 nm, the tetragonality of $BaTiO_3$ nanoparticles is reduced and the unit-cell volume expands. Note that this phenomemon is responsible for reducing giant LO–TO splitting of phonon modes in $BaTiO_3$, because the Born effective charges are not influenced by a change of structure or size.

Lattice expansion upon size reduction was also observed by TEM in CeO_{2-x} nanoparticles, having a size of 2−8 nm [11].

Studies of $CaWO_4$ nanocrystals revealed similar common trend: a lattice expansion and increased symmetry of structural units with a reduction of physical dimension [43]. Lattice volume increases monotonically with particle size reduction, while the axial ratio of c/a decreases from 2.169 to 2.154, tending to c/a=2 for an ideal structure of scheelite phase with equal cation coordination. As a surprise, the same trend of increasing symmetry (decreasing c/a axis ratio) was observed in bulk $CaWO_4$ under high pressure when the unit cell volume contracts [44].

Using x-ray diffraction G. Li *et al.* [13] have found similar behavior in rutile TiO_2 nanocrystals. With a reduction in the physical dimensions, rutile TiO_2 nanocrystals show a linear lattice expansion.

Only metal compound, which does not obey common rule, is TiN, where the lattice constant decreases upon decreasing nanoparticle size [45].

At the same time, there is no unique explanation of possible mechanisms responsible for the unit cell volume expansion in metal oxides upon decreasing the size of the nanoparticles. Basically three mechanisms have been proposed.

The first mechanism was introduced by Tsunekawa *et al.* [11, 42] based on the X-ray photoelectron spectroscopy (XPS) studies of $BaTiO_3$ and CeO_{2-x} nanoparticles. Authors proposed that the lattice constant change in oxide (ionic) nanoparticles originates from a variation in nominal ionic valences. The reduction of the valence induces an increase in the lattice constant due to a decrease in electrostatic forces, but an increase in the valence does not always lead to lattice shrinkage. Nanoparticles with the increase in ionicity or nominal valence may show either expansion or shrinkage, depending on the structure of the large clusters [11].

The second mechanism was proposed by G. Li *et al.* [13]: they have studied rutile TiO_2 nanocrystals using XRD and XPS techniques. Upon reduction of the physical dimensions, rutile TiO_2 nanocrystals show a linear lattice expansion and an anomalous

covalency enhancement in apparent contradiction to the ionicity increase in $BaTiO_3$ and CuO nanocrystals as reported by S. Tsunekawa et al. [11] and V. R. Palkar et al. [41]. A surface defect dipole model is proposed to explain these physical phenomena in terms of the strong interactions among the surface dipoles that produce an increased negative pressure. The covalency enhancement is interpreted according to the critical properties of the elongated Ti–O bond lengths in the expanded lattice [13].

The third mechanism proposed by M. Fukuhara [12] suggests that an expansion of the lattice upon decreasing of the size of MgO, α-Fe_2O_3 and TiC nanoparticles is due to the screening effect of electrons coming from the the outer s and p shells. These electrons originate on the nanoparticle surface, because of the large number of the broken bonds present there, and they screen the Coulomb potential [12]. The proportion of atoms on the surface increases upon a decrease of the nanoparticle size, leading to stronger Coulomb potential screening and, thus, weakening of interatomic bonds that results in an expansion of the lattice constant. This scenario has been proposed to all nanoscale particles, including MnF_2, CeO_{2-x} and $BaTiO_3$ [12].

Thus, a careful studies of nanoparticles and other nanosized objects are required. Most probably there is no single rule, but there are some trends, and each individual case should be studied carefully avoiding experimental errors as much as possible.

2.2 State of the art in the atomic structure analysis of nanoobjects

As we have seen, a key requirement for understanding and control of nanomaterial properties is the knowledge of its atomic structure, whose determination is a challenging task, called "nanostructure problem" [1].

Atomic structure can be resolved relatively easy for the crystals, where robust and quantitative methods exist including x-ray diffraction (XRD) [46]. The challenge is to reconstruct the phase information from the intensity data, because in XRD measurements one collects amplitude and do not know the phase of the signal. This problem is resolved by solving a large set of nonlinear equations with unknown phases and atomic coordinates, known Bragg peak positions and intensities. Since in crystals one usually has much more Bragg peaks than a number of unknown parameters, the structure problem can be solved [46].

Table 2.1: Experimental probes of nanoscale structure from [1].

Probe	Direct (D) or indirect (I) method	Probes whole sample (B) or a small part of it (L)
Total scattering / PDF	D	B
EXAFS	D	B
XANES	I	B
Raman spectroscopy	I	B
NMR/Mössbauer/μSR	I	B
TEM/electron diffraction	D	L
Atom probe tomography	D	L
STM/AFM	I	L

Unfortunately this is not a case for nanoobjects where instead of the sharp Bragg peaks one observes broad and continuous intensity distribution that is not suitable for conventional (Rietvield method based) crystallographic structure determination. One has too few data to solve the structure of nanoobject from the X-ray scattering data [1].

Different experimental techniques have been developed to study nanomaterials [1, 14, 15] (see Table 2.1), but only two methods, namely total scattering [16] and x-ray absorption spectroscopy [18, 19], provide with direct access to the structural information for the whole sample. Other methods (like Raman spectroscopy) either provide indirect information about the structure, or give very local information about the single particle or small part of the sample (like TEM).

In this study we have used x-ray absorption spectroscopy as the main method to determine atomic structure of nanoobjects from the extended x-ray absorption fine structure (EXAFS). We believe that this technique is well adapted to the nanostructure problem and contains very rich structural information. Brief insight on the EXAFS theory and data analysis will be given in the next chapters (3 and 4).

3

X-ray absorption spectroscopy

3.1 Basics of X-ray absorption

X-ray interaction with matter (Fig. 3.1) can be separated into two processes: elastic or coherent (Thomson) scattering, which conserve the kinetic energy of the incident photons, and inelastic or incoherent scattering, when the kinetic energy of the incident photons is not conserved (Compton scattering, electron-positron pair production and photoexcitation of electrons) [47].

We will be interested in the latter process, namely photoexcitation of electrons, which causes the absorption of x-rays. In this process x-ray photon excites electron of the core shell (for example, 1s (K-edge) or 2s, 2p (L-edges)) and creates an excited state with a hole in the inner shell, excited electron and all other electrons being relaxed in the presence of the core hole. The life time of the excited state is very short (10^{-15}-10^{-18} s), and it decays to the ground state through the emitting x-ray photon or Auger photoelectron [22].

The x-ray absorption coefficient $\mu(E)$ is defined by the Beer-Lambert law as:

$$\mu(E) = \frac{1}{d} \ln(\frac{I_0}{I}), \tag{3.1}$$

where E is the x-ray photon energy, d is the thickness of a sample, I_0 and I are incident and transmitted x-ray beam intensities, respectively.

X-ray absorption spectrum is measured as a function of x-ray energy and has three main features seen in Fig. 3.2. The absorption coefficient decreases with increasing of the x-ray energy before the absorption edge, next, it increases sharply at the edge, and, finally, it is modulated by the oscillating fine structure above the edge.

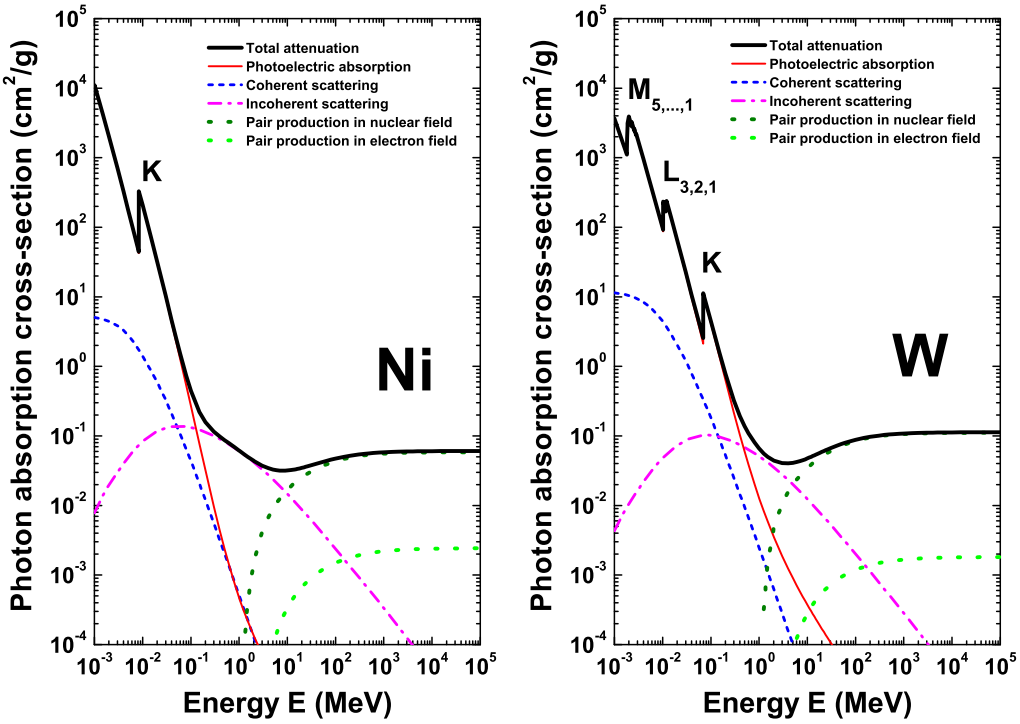

Figure 3.1: Photon absorption cross-section components and total attenuation for Ni atom (on the left) and W atom (on the right). K is the absorption edge due to the electron transitions from the core 1s level, L is the absorption edge for 2s and 2p levels, and M is that for 3s, 3p, 3d levels [48].

The energy of the absorption edge is specific to each element and each electronic shell of this element [22]. This allows one to use x-ray absorption spectroscopy to identify particular chemical element and its electronic properties. The oscillating part is unique fingerprint of the local environment (electronic and structural) around the absorbing atom, sensitive to the positions of the surrounding atoms and valence state of the absorbing atom and its electronic environment. For this reason x-ray absorption spectroscopy is local probe of various materials, including, crystals, glasses, liquids and even gasses.

The extended x-ray absorption fine structure (EXAFS) signal $\chi(E)$ is defined as the normalized, oscillatory part of the x-ray absorption coefficient (μ) above absorption edge [22, 28]

$$\chi(E) = \frac{\mu(E) - \mu_0(E) - \mu_b(E)}{\mu_0(E)} \tag{3.2}$$

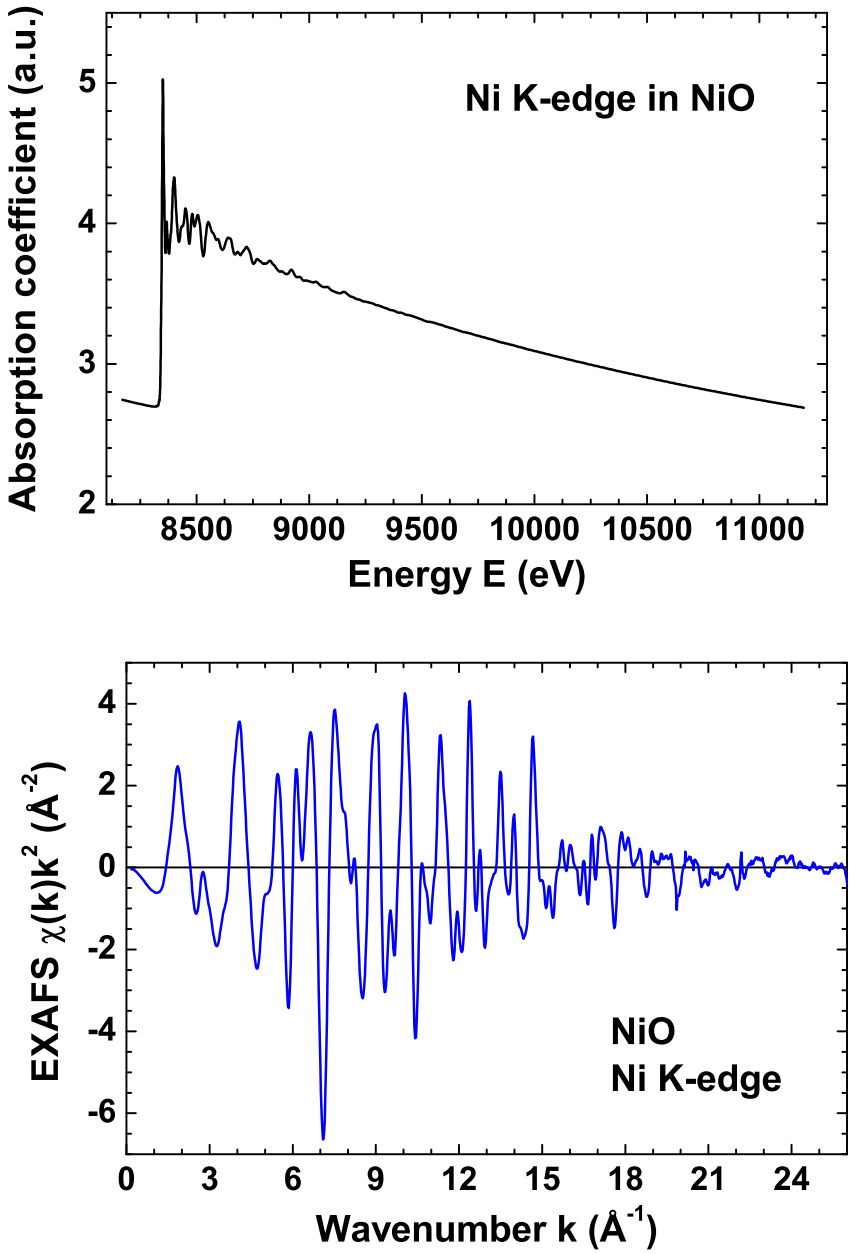

Figure 3.2: (Upper panel) The experimental x-ray absorption spectrum (μ) at the Ni K-edge in microcrystalline NiO. (Lower panel) Ni K-edge EXAFS spectrum $\chi(k)k^2$ extracted from the experimental absorption coefficient shown in the upper panel.

where $\mu_b(E)$ is the background absorption coming from electrons of the outer shells, and $\mu_0(E)$ is the atomic-like contribution, i.e., an absorption by the atom in the absence of surrounding atoms.

From quantum mechanics we know that the absorption coefficient is proportional to the photoexcitation transition rate which is given by the Fermi's Golden Rule. In the one-electron and dipole approximations it is given as [49]

$$\mu \propto \sum_f |\langle\psi_f|\vec{p}\cdot\vec{A}(r)|\psi_i\rangle|^2\delta(E_f - E_i - \hbar\omega) \tag{3.3}$$

where ψ_i is the wave function of initial state, ψ_f is the wave function of final state, $E_f = E_i + \hbar\omega$ is the energy conservation condition, $\vec{p}\cdot\vec{A}(r)$ is the x-ray absorption transition operator, $\vec{p}$ is the momentum operator, and $\vec{A}(r)$ is the vector potential of the incident electromagnetic field.

Within the multiple-scattering (MS) theory [22, 50] Eq. 3.3 can be rewritten using the Green function formalism as

$$\mu \propto \frac{1}{\pi} Im\langle\psi_i|\vec{p}\cdot\vec{A}(r')G(r,r',E)\vec{p}\cdot\vec{A}(r)|\psi_i\rangle\theta(E - E_F) \tag{3.4}$$

where $G(r,r',E)$ is the full one electron propagator, describing the propagation of the excited photoelectron from point r to point r', and $\theta(E - E_F)$ is a broadened step function at the Fermi energy E_F. The Green function can be determined from the solution of the Dyson equation, which is one-particle Schrödinger equation [22, 51]:

$$(\nabla^2 + E - U_c(\vec{r}) - \Sigma_{XC}(E;\rho(\vec{r})))G(\vec{r},\vec{r}',E) = \delta(\vec{r} - \vec{r}') \tag{3.5}$$

where $U_c(\vec{r})$ is the final state Coulomb potential felt by the photoelectron, and $\Sigma_{XC}(E;\rho(\vec{r}))$ is "self energy", which is equivalent of the exchange-correlation potential.

The Green function G of an excited photoelectron with the energy E can be expressed as a contribution from the absorbing atom (atomic-like absorption) G^C and perturbation created by the neighboring atoms treated as a scatterers of the photoelectron G^{SC} [22, 50]

$$G = G^C + G^{SC}, \tag{3.6}$$

$$G^C = G^0 + G^0 t_c G^0, \tag{3.7}$$

$$G^{SC} = G^0 t G^0 + G^0 t G^0 t G^0 + G^0 t G^0 t G^0 t G^0 + ..., \tag{3.8}$$

where G^0 is the free particle Green function describing propagation of the photoelectron between two points in space, t is the scattering matrix describing scattering of the photoelectron from a single atom. G^0 can be expressed in form of the spherical wave

$$G^0(\vec{r},\vec{r}',E) = -\frac{1}{4\pi}\frac{e^{ik|\vec{r}-\vec{r}'|}}{|\vec{r}-\vec{r}'|}, \tag{3.9}$$

$$k = \sqrt{(2m_e/\hbar^2)(E-E_F)}, \tag{3.10}$$

where k is the photoelectron wave number, m_e is the electron mass, and $\hbar$ is the Plank's constant).

Eq. 3.8 is called the multiple-scattering series and describes the contribution of the neighboring atoms to the total absorption. The first term corresponds to the single-scattering processes, where only atom pairs consisting of the absorbing atom and one neighboring atom are involved. The second term corresponds to the double-scattering processes, in which two neighboring atoms are involved. Further terms correspond to the triple and higher order scattering processes. Each term in Eq. 3.8 can be written as a sum over every path of the corresponding order [22, 50]

$$G^{SC} = \sum_{i\neq 0} G_c t_i G_c + \sum_{i,j\neq 0; i\neq j} G_c t_i G^0_{i,j} t_j G_c + ..., \tag{3.11}$$

where G_c is the propagator between the absorbing and neighboring atom i, and $G^0_{i,j}$ is the propagator between atoms i and j.

3.2 Gaussian approximation

The presence of thermal (dynamic) or structural (static) disorder in real materials modifies the scattering path geometry and, thus, should be included into the formalism. Since the life time of the x-ray absorption process (10^{-15}-10^{-18} s) is much smaller than the characteristic life time of thermal vibrations (10^{-13}-10^{-14} s), one needs to average over all atomic configurations, contributing into the measured experimentally absorption coefficient.

In the case of weak disorder, one can assume Gaussian distribution of the atomic coordinates, and applying small atom approximation, i.e., assuming atoms as point scatterers, one gets [22, 52]

$$\langle e^{i2k}\sum_i (\vec{u}_i - \vec{u}_{i+1})\cdot\vec{R}_{i,i+1}\rangle = e^{-2k^2\sigma^2}, \tag{3.12}$$

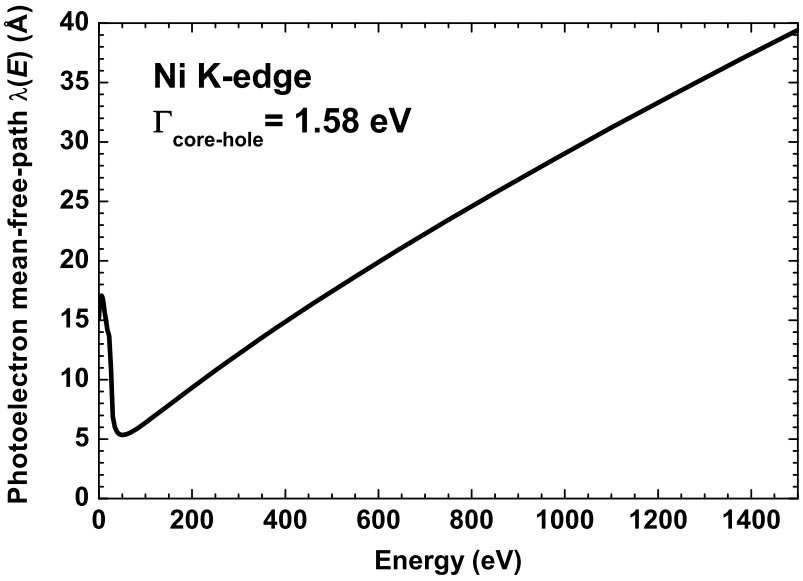

Figure 3.3: The mean free path $\lambda(E)$ of photoelectron depending on the energy for the Ni K-edge including the core-hole effect. $\Gamma_{\mathrm{core-hole}}$ is the core-hole broadening parameter [22].

where $\vec{u}_i$ is a displacement from the equilibrium position of the atom at site i, and σ^2 is the mean-square fluctuation of the corresponding path length, i.e., the mean-square relative displacement (MSRD).

In this case the EXAFS signal can be written as [22]

$$\chi(k) = S_o^2 \sum_j \frac{N_j F_j^{eff}(k)}{kR_j^2} \sin[2kR_j + \phi_j^{eff}(k)] e^{-2k^2\sigma_j^2} e^{-2R_j/\lambda(k)}, \qquad (3.13)$$

where S_o^2 includes multielectron effects leading to the amplitude damping, N_j is the degeneracy of the path j, back scattering amplitude $F_j^{eff}(k)$ includes the effects of the scattering amplitudes of each atom in a path j as well as the scattering angles, $\phi_j^{eff}(k)$ is the phase shift for path j including its angular dependencies, R_j is the half length of the scattering path, σ_j^2 is the mean-square fluctuation of the corresponding path length, and $\lambda(k)$ is the mean free path (MFP) of the photoelectron. The MFP is shown in Fig. 3.3 for the Ni K-edge, including the core-hole effect.

In the so-called single-scattering approximation, only scattering paths involving two atoms (the absorber and the scatterer) are considered and the meaning of the parameters in Eq. 3.13 becomes more simple. The degeneracy of the single-scattering path

corresponds to the coordination number, i.e., the number of atoms in the corresponding shell. The half path length is equal to the interatomic distance between the absorber and the scatterer. Finally, σ^2 is a variation of the corresponding interatomic distance or the mean-square relative displacement (MSRD) [22]

$$\sigma_R^2 = \langle[(\vec{u}_R - \vec{u}_0)\cdot\vec{R}]^2\rangle = \langle(\vec{u}_R\cdot\vec{R})^2\rangle + \langle(\vec{u}_0\cdot\vec{R})^2\rangle - 2\langle(\vec{u}_R\cdot\vec{R})(\vec{u}_0\cdot\vec{R})\rangle, \qquad (3.14)$$

where $\langle(\vec{u}_R\cdot\vec{R})(\vec{u}_0\cdot\vec{R})\rangle$ is the displacement-displacement correlation function for the absorbing atom at site $\vec{0}$ and the scattering atom at site $\vec{R}$, and $\langle(\vec{u}_R\cdot\vec{R})^2\rangle$ is the mean-square displacement of the atom at site $\vec{R}$ from its equilibrium position.

Thus, Eq. 3.13 connects the EXAFS signal $\chi(k)$ with the local structure parameters around the absorbing atom (N_j, R_j, σ_j^2). However, to extract this structural information, one should know the values of the back scattering amplitudes $F_j^{eff}(k)$ and phase shifts $\phi_j^{eff}(k)$. These values can be calculated by *ab initio* programs, like FEFF [25] (which got its name from F_j^{eff}) or, as we will see later, in some cases extracted from the experimental data of the reference compound.

The EXAFS spectroscopy is element sensitive method, because it gives information on the local structure only around particular type of the atom, absorbing x-rays. This gives unique information, for example, in case of the complex oxides like $CuWO_4$, where we can study the local environments of Cu and W atoms separately and independently, or for doped materials like ZnO:Al, where we can study the local structure of Zn and Al. This is unique feature of the EXAFS, compared with other structure determination methods, like x-ray or neutron diffraction.

It is important to understand that EXAFS gives relative to the absorbing atom values of interatomic distances and MSRD. As it has been already stated above, the EXAFS process takes very short time (10^{-15} to 10^{-18} s) compared with the characteristic lattice vibration time scale (about 10^{-13}-10^{-14} s). Therefore we can treat all atoms as "frozen" during single photoabsorption event, and EXAFS measures a distribution of instantaneous interatomic distances. This fact is very important to understand when comparing data obtained by EXAFS with that from X-ray, neutron or electron diffraction. In EXAFS we measure the averaged length of scattering paths (or interatomic distances in the single-scattering approximation) and the MSRD values, not the distances between the equilibrium positions of atoms and the means squared displacements (MSD) of atoms from their equilibrium positions as in diffraction experiments.

Another important point is that EXAFS is not limited to bulk crystals, the signal depends only on the amount of the absorbing atoms and senses their local neighborhood. This means, it is suitable for crystals, glasses, nanosized objects like nanoparticles, nanowires, thin films, liquids and gasses.

3.3 Cumulant approximation

Equation 3.13 does not take into account any anharmonic effects, since it is based on the assumption that atoms have Gaussian distribution of their coordinates, which is true in the harmonic approximation. When the anharmonic contributions are significant, one can use the cumulant approximation [52, 53, 54]

$$\langle e^{i2k}(r-R)\rangle = \exp\sum_{n=0}^{\infty}\frac{(2ik)^n}{n!}C_n, \tag{3.15}$$

where C_n is the nth cumulant.

In this casse one can rewrite the conventional EXAFS formula in the form where additionally to σ^2 ($\equiv C_2$) we have even moments, but odd moments contribute to the EXAFS phase [52]

$$\begin{aligned}\chi(k) &= \sum_{j}^{shells}\frac{N_j F_j(k) e^{-2k^2\sigma_j^2+\frac{2}{3}C_{4j}k^4-\frac{4}{45}C_{6j}k^6}}{kR_j^2}e^{-2R_i/\lambda(k)} \\ &\times \sin[2kR_j-\frac{4}{3}C_{3j}k^3-\frac{4}{15}C_{5j}k^5+\phi_j(k,R_j)].\end{aligned} \tag{3.16}$$

For weak disorder only first cumulants (C_0, C_1 and C_2) are significant and Gaussian approximation works fine. When the Debye temperature is approached, then anharmonic effects cannot be neglected. When temperature increases further, higher order cumulants become important.

3.4 Radial distribution function reconstruction

In the general case EXAFS signal can be written in terms of the distribution functions [55]

$$\chi(k) = \int 4\pi R^2\rho_0 g_2(R)(\chi_2^{oio}(k)+\chi_4^{oioio}(k)+...)dR$$

$$+\int\int\int 8\pi^2 R_1^2 R_2^2 sin(\theta)\rho_0^2 g_3(R_1,R_2,\theta)(2\chi_3^{oijo}(k)+2\chi_4^{oiojo}(k)$$
$$+\chi_4^{oijio}(k)+\chi_4^{ojijo}(k)+...)dR_1 dR_2 d\theta+..., \quad (3.17)$$

where ρ_0 is the average density of a system, $\chi_m(k)$ are the multiple-scattering EXAFS signals of the $(m-1)$ order generated from the group of atoms (o, i, j, k, ...) described by g_n.

If we consider only single-scattering contribution from the single coordination shell containing only one type of atoms and which is well separated from other shells, then we can simplify this expression (Eq. 3.17) by taking into account only the first integral. One can also define the radial distribution function (RDF) $G(R)$

$$G(R) = 4\pi R^2 \rho_0 g_2(R), \quad (3.18)$$

which corresponds to the number of atoms in the region between R and $R+dR$ around the absorbing atom. Note also that RDF $G(R)$ must be smooth and positive function, but can have an arbitrary shape. The average number of atoms N in the region between R_{min} to R_{max} is determined as

$$N = \int_{R_{min}}^{R_{max}} G(R)dR. \quad (3.19)$$

As a result, one obtains for the EXAFS signal from a single shell [55]

$$\chi(k,G(R)) = \int_{R_{\min}}^{R_{\max}} \frac{G(R)}{kR^2} f(k,R)\sin[2kR+\phi(k,R)]dR. \quad (3.20)$$

An invertion of Eq. 3.20 allows one to find RDF $G(R)$, which will give the best fit to the experimental EXAFS signal. Mathematical methods, how to solve this ill-posed problem are described in [56].

The limitations of this method are the single-scattering approximation and its applicability to coordination shells containing only one type of atoms.

This approach is especially suitable in cases where the cumulant expansion of the EXAFS signal, described before, does not converge, typical example is highly disordered materials like glasses, low-symmetry systems, materials where even the first coordination shell has very large distortion.

4

EXAFS data analysis and simulations

4.1 Extraction of EXAFS data

EXAFS spectra extraction is well described in the review article [28]. In this work it was performed by the EDA software package [56], freely available on the web site http://www.dragon.lv/eda/. Here we give short description of this procedure.

To obtain structural information from X-ray absorption spectrum (Fig. 4.1), one needs first to extract the oscillatory part - the EXAFS. We will use the standard procedure for extracting EXAFS signal $\chi(k)$ from the absorption coefficient $\mu_{exp}(E)$, which is described in [28] and implemented in EXAFS Data Analysis software package EDA [56].

The first step is to subtract the background contribution $\mu_b(E)$, obtained by approximation of the pre-edge signal with the modified Victoreen polynomial

$$\mu_b(E) = A + B/E^3. \tag{4.1}$$

The $\mu_b(E)$ is extrapolated to the whole range of the spectrum and subtracted from the experimental signal $\mu_{exp}(E)$

$$\mu_1(E) = \mu_{\exp}(E) - \mu_b(E). \tag{4.2}$$

The next step is to find and subtract atomic-like contribution $\mu_0(E)$. This is an important step, because inaccuracies in $\mu_0(E)$ lead to a distortion of the $\chi(k)$ signal. In order to increase the accuracy in EDA software this step is done in three iterations.

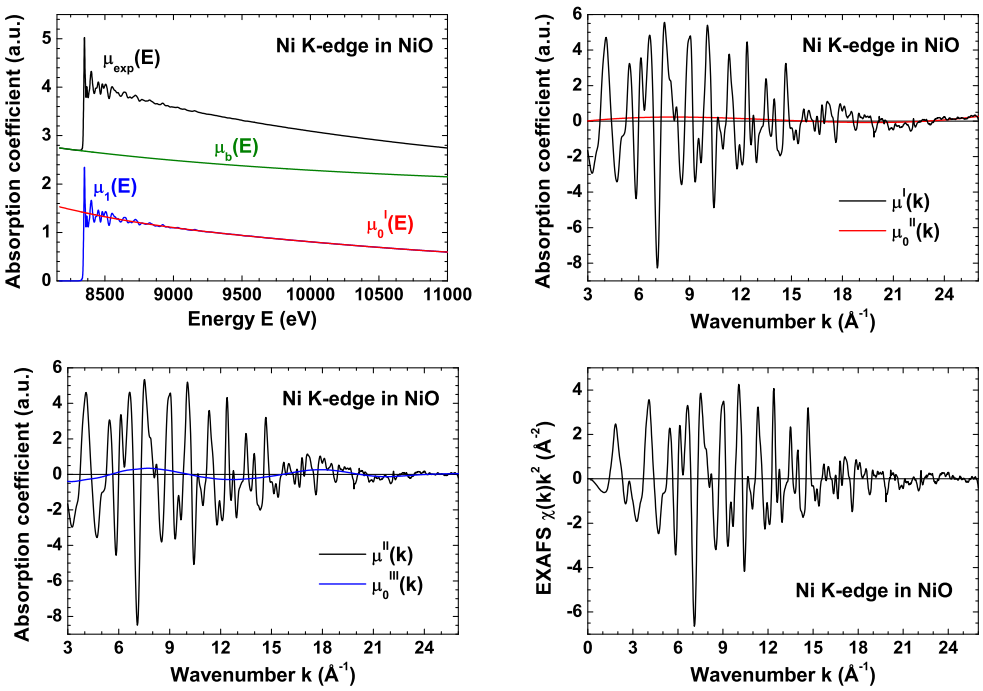

Figure 4.1: Example of the EXAFS extraction procedure for the Ni K-edge in NiO. See text for details.

At the first iteration, $\mu_0(E)$ is approximated by a polynomial $\mu_0^I(E)$ of power m_1 and subtracted from the signal

$$\mu^I(E) = \mu_1(E) - \mu_0^I(E). \tag{4.3}$$

At this stage the $\mu^I(E)$ is converted into k-space and multiplied by a factor k^n, where $n = 1, 2, 3$ and k is the photoelectron wave vector (Eg. 3.10).

At the second iteration zero line function $\mu_0^{II}(k)$ is approximated by another polynomial of power m_2 and $\mu^{II}(k)$ is obtained

$$\mu^{II}(k) = \mu^I(k) - \mu_0^{II}(k). \tag{4.4}$$

The goal of this step is to eliminate distortion of $\chi(k)$ especially those in high k values region, which are enlarged after multiplication by the factor k^n. The goal is to find $\mu^{II}(k)$ which is oscillating around zero within all range of k.

At the third iteration, $\mu_0(k)$ is fine tuned using the cubic-smoothing-spline

$$\mu_0^{III}(k) = \sum_i (a_i k^3 + b_i k^2 + c_i k + d_i), \tag{4.5}$$

and $\mu^{III}(k)$ is obtained as

$$\mu^{III}(k) = \mu^{II}(k) - \mu_0^{III}(k), \tag{4.6}$$

where i corresponds to i-th experimental point. Coefficients (a_i, b_i, c_i, d_i) are selected to guarantee continuous first and second derivatives of $\mu_0^{III}(k)$, and the sum over the all data points of $[\mu^{II}(k) - \mu_0^{III}(k)]^2$ should be equal to the smoothing parameter s entered by the user. The smoothing parameter value is varied in order to eliminate from the signal low frequency components but not distorting EXAFS oscillations.

At the end of this procedure the experimental EXAFS signal $\chi(k)$ is calculated as

$$\chi(k) = \frac{\mu(k) - \mu_0(k) - \mu_b(k)}{\mu_0(k)} \tag{4.7}$$

where $\mu_0(k) = \mu_0^I + \mu_0^{II} + \mu_0^{III}$. Thus extracted EXAFS signal is used in further analysis.

4.2 Conventional EXAFS analysis in the single-scattering approximation

Conventional approach to the analysis of EXAFS within the single-scattering approximation is well described in the review article [28]. In this work it was performed using the EDA software package [56].

The single-scattering approximation is always valid for the analysis of the first coordination shell around the absorbing atom because the first shell radius is smaller than the half of any other scattering path length. However, the approximation can be sometimes reliably employed also for the outer shells, if the multiple-scattering effects there give negligible contribution. Therefore before starting any analysis one needs to find those coordination shells, where the single-scattering approximation can be used. We did theoretical calculations of the EXAFS spectra for all model compounds using FEFF8 code [25]. In the case of the Ni K-edge in NiO, having cubic rock-salt type structure [57], the single-scattering approach can be used for the first two coordination shells of the absorbing Ni atom as it can be seen in Fig. 4.2. Here the multiple-scattering effects become important above ~ 3 Å.

The next step is to filter the experimental EXAFS signal leaving those coordination shells which contain only single-scattering contributions. This is done by applying Fourier filtering procedure, i.e., by calculating direct ($FT(R)$) and inverse ($BFT(R)$)

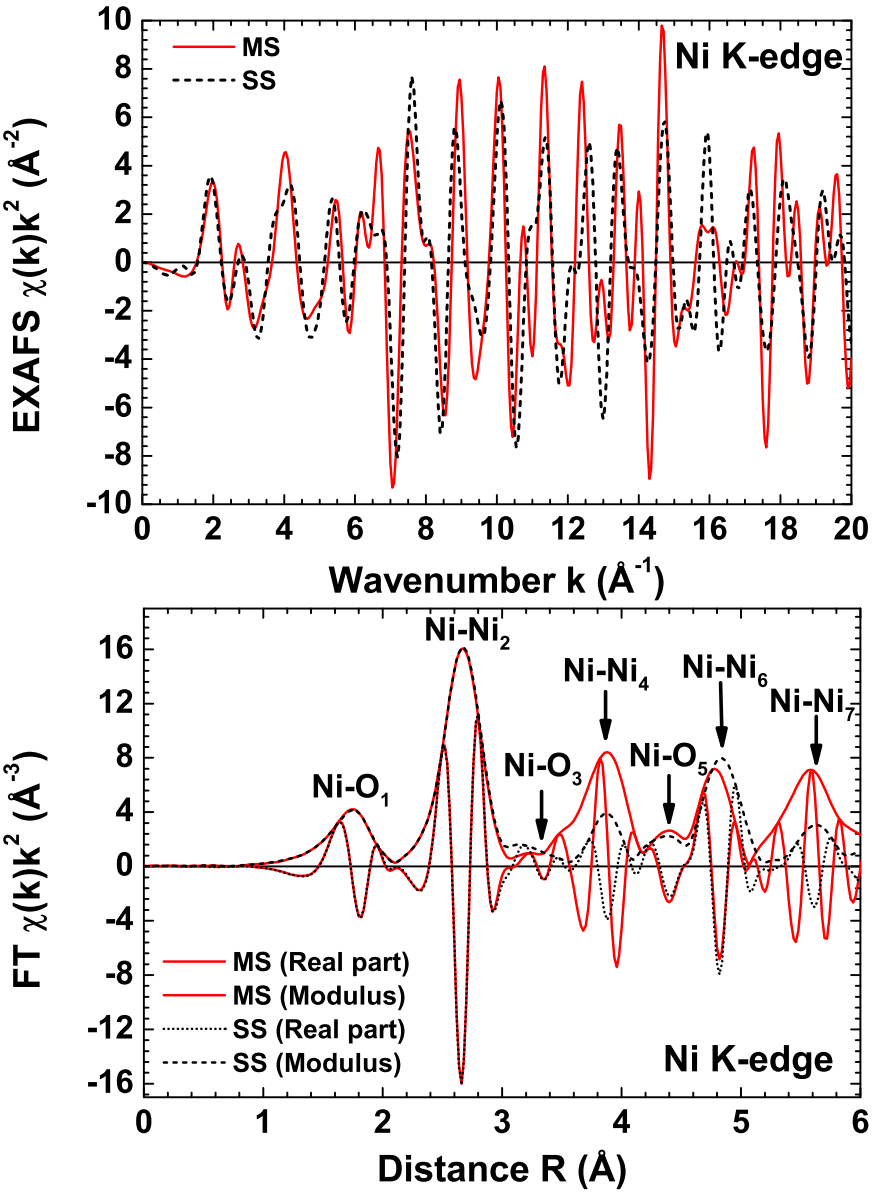

Figure 4.2: Theoretical Ni K-edge EXAFS spectra for NiO calculated with all multiple-scattering (MS) and only single-scattering (SS) contributions. Contirubtions from the first seven coordination shells are indicated by arrows in lower panel. As one can see from the Fourier transform (FT) of the EXAFS spectra, the multiple-scattering contributions do not contribute into the first and second coordination shell of Ni atoms. The calculations were performed without accounting for thermal damping (all MSRD parameters σ^2=0) and setting S_o^2=1.

Fourier transforms (FT) of the EXAFS signal within required intervals in k- and R space

$$FT(R) = \sqrt{\frac{2}{\pi}} \int_{k_{\min}}^{k_{\max}} \chi(k) k^n W(k) \exp(-2ikR) dk \tag{4.8}$$

$$BFT(k) = \frac{1}{k^n W(k)} \sqrt{\frac{2}{\pi}} \int_{R_{\min}}^{R_{\max}} FT(R) \exp(2ikR) dR \tag{4.9}$$

where $k_{\min}$, $k_{\max}$ and $R_{\min}$, $R_{\max}$ denote, respectively, the ranges of the direct and inverse FT; $W(k)$ is a window function [56]. For example, in the case of NiO the first two coordination shells contribute in the R-space interval from 1 to 3 Å, as follows from the results of our FEFF simulations (Fig. 4.2).

When EXAFS signal from a single shell is isolated, one can apply Gaussian, cumulant or RDF reconstruction methods (described in previous chapter) to find the local atomic structure around the absorbing atom.

Let us first concentrate on the Gaussian and cumulant models, which are the most popular. The cumulant model is more general, because if one neglects all cumulants of the order 3 and higher, then Eq. 3.16 tranforms into the Gaussian model (Eq. 3.13). In order to find structural parameters N_i, R_i, σ_i^2, C_{3i}, C_{4i}, C_{5i} and C_{6i} in Eq. 3.16, one must know the values of the amplitude $F_i(k, R_i)$ and phase $\phi_i(k, R_i)$ functions, which can be obtained using one of two methods.

The first method allows one to extract these functions from the experimental EXAFS signal of the reference compound which has local environment around absorbing atom close to that of the studied material. The extraction procedure is similar to previously described Fourier filtering procedure, except that performing back-Fourier transformation one calculates separately amplitude and phase of the EXAFS signal

$$AMPLITUDE(k) = \sqrt{\Im(BFT(k))^2 + \Re(BFT(k))^2}, \tag{4.10}$$

$$PHASE(k) = \arctan\left(\Im(BFT(k))/\Re(BFT(k))\right), \tag{4.11}$$

which are next normalized to the known values of N_{ref} and R_{ref} for the reference compound. Note that here $\Im$ and $\Re$ denote the imaginary and real parts of a function, respectively.

Thus extracted amplitude and phase functions can be used in the EXAFS analysis to find structural parameter values for other compounds having the same absorbing and scattering atoms as in the reference. Note that in this case one obtains the values

of MSRD $\Delta\sigma_i^2$, which are relative to the value of the reference compound. Also the precision of interatomic distance R_i depends on how precise is known R_{ref} for the reference, which means, that strictly speaking we should consider $\Delta R_i = R_i - R_{ref}$. The same applies to the coordination number N_i.

It is good to use low temperature EXAFS spectrum as a reference, because the EXAFS oscillations are the strongest at low temperatures due to reduced damping caused by the thermal motion of atoms. Also the use of the reference allows one to exclude the term $S_o^2 \exp(-2R_i/\lambda(k))$ from consideration since it is assumed to be the same as in the reference compound and is included into the amplitude function.

For example, we used microcrystalline NiO at low temperature ($T = 6$ K) as a reference sample, to study properties of NiO thin films and nanoparticles. The same reference amplitude and phase were also used to study properties of microcrystalline NiO at higher temperatures up to 300 K.

The second method is based on the use of the amplitude $F_i(k, R_i)$ and phase $\phi_i(k, R_i)$ functions obtained theoretically. Here we employed FEFF8 code [25] which uses complex exchange correlation Hedin-Lundqvist potential, and, thus, allows one to take into account the contribution of the inelastic scattering processes determining the mean free path of the photoelectron $\lambda(k)$. Therefore in our calculations using Eq. 3.13 we assume that the term $\exp(-2R_i/\lambda(k)) = 1$. Also the obtained value of N_i is actually $N_i^{eff} = N_i S_o^2$, because it is impossible to separate these two quantities (N_i and S_o^2).

When the amplitude $F_i(k, R_i)$ and phase $\phi_i(k, R_i)$ functions are available for desired shells, the conventional fitting procedure can be applied to obtain the values of structural parameters N_i, R_i, σ_i^2 as well as C_{3i}, C_{4i}, C_{5i}, C_{6i}, if needed. Note that according to the Nyquist-Shannon sampling theorem [58, 59] the maximum number of free parameters N_{exp} in a model

$$N_{exp} = \frac{2\Delta k \Delta R}{\pi} + 2 \tag{4.12}$$

is determined by Δk and ΔR intervals in k and R space used in the simulations.

In the radial distribution function (RDF) reconstruction procedure [56, 60], instead of using a set of structural parameters, one vary the shape of the RDF $G(R)$, which should be a positive and smooth function. The theoretical amplitude $F_i(k, R_i)$ and phase $\phi_i(k, R_i)$ functions were used in this case. Such method is very useful when Gaussian or cumulant methods do not converge due to strong anharmonicity or disorder

of corresponding coordination shell, for example in glasses, amorphous materials or liquids [60, 61].

4.3 Advanced methods for EXAFS data analysis

Conventional methods of EXAFS data analysis are valid for coordination shells, which do not contain multiple-scattering contributions. Unfortunately in the most cases this is applicable only for the first coordination shell. This means that we are analyzing only small fraction of the information available in the EXAFS spectra.

Therefore the analysis of the full EXAFS spectrum, including contributions from outer coordination shells, requires more advanced and elaborated approach, because multiple-scattering (MS) effects become important there [32]. The MS signal contains valuable contribution from the multi-atom distribution functions, containing information not only about their distances, but also information about the bond angles (Eq. 3.17). Note that the multiple-scattering signals have non-linear angular dependence and are sensitive even to the small variations of the angles [62].

One way to solve this problem is to include in the fitting also multiple-scattering paths, as it is implemented in FEFF [25] and FEFFIT [29, 30]. But the problem is that the number of required parameters increases rapidly, since each scattering path, including MS paths, contains own N_i, R_i, σ_i^2 values. Even when some parameters can be correlated due to the structure symmetry and physical considerations, their number grows up rapidly upon increasing cluster size contributing into the total EXAFS and at some cluster radius will become larger than the number of independent data points (N_{exp}) in the experimental EXAFS signal according to the Nyquist-Shannon sampling theorem [58, 59].

In Fig. 4.3 one can see the case of NiO. In ideal cubic NiO crystal the account of symmetry allows one to reduce significantly the number of unique photoelectron scattering paths (red squares). As a result, one can extract information up to the sixth coordination shell around Ni atom. However, in the case of NiO nanoparticles with defects, the symmetry is broken and one should consider all scattering paths (black circles), then we are able to perform multiple-scattering analysis only up to the second coordination shell, which is not very useful, since it can be done also within the Gaussian single-scattering approximation.

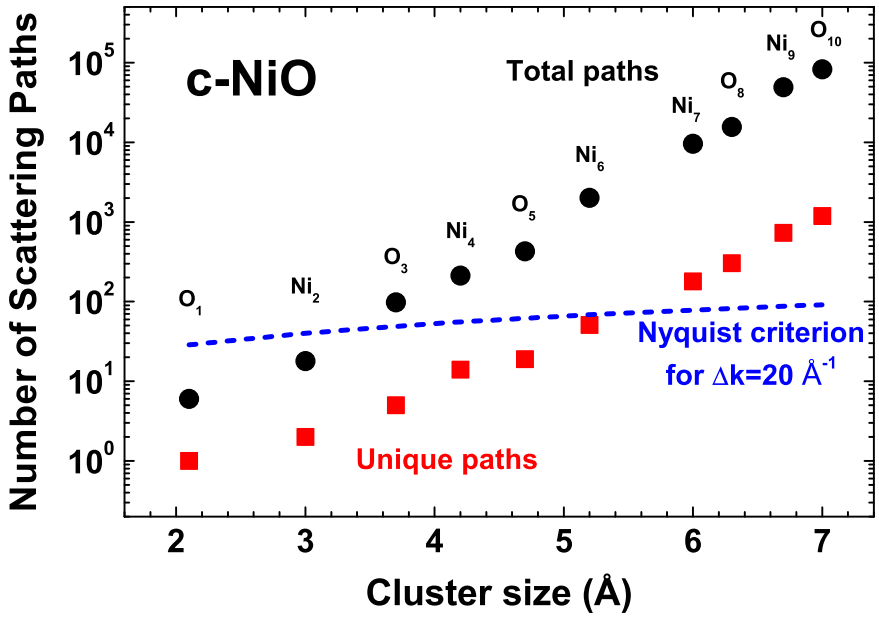

Figure 4.3: The dependence of the number of scattering paths on the cluster size for NiO. Note the logarithmic scale on the number of scattering paths axis.

To overcome these problems, there are several advanced methods available for EXAFS data analysis, including molecular dynamics, Monte-Carlo, or reverse Monte-Carlo simulations in combination with EXAFS spectra modeling.

These methods were successfully applied in the past to disordered materials like glasses [63, 64, 65, 66, 67, 68], solutions [69, 70, 71, 72] and liquids [73, 74].

As a result of these simulations, a set of instant atomic configurations is obtained for which the configuration-averaged EXAFS spectrum is calculated. This allows including the dynamic and static disorder effects into *ab initio* multiple-scattering theory without applying any rough approximation. Thus obtained configuration-averaged EXAFS spectrum can be directly compared with the experimental one. An advantage of the reverse Monte-Carlo simulations is that there is, in principle, no need for any starting model of a compound [75, 76].

In recent years a combination of classical molecular dynamics and *ab initio* EXAFS calculations has been successfully applied to solids, including crystals [23, 24, 74, 77, 78, 79, 80, 81, 82, 83]. In the present work (see below) we have extended this method to nanosized objects.

4.4 MD-EXAFS approach for bulk crystals and nanoparticles

To use the full power of the multiple-scattering EXAFS theory, we employed a recently developed simulation method [23, 24], combining *ab initio* multiple-scattering EXAFS calculations with classical molecular dynamics (MD), further referenced as MD-EXAFS. This approach allows us to reconstruct the local environment of the absorbing atom, which contains not only single-scattering, but also multiple-scattering contributions, at the same time taking into account thermal disorder, structure relaxation and presence of defects.

Below we will explain an implementation of the MD-EXAFS scheme for nanoparticles in more details (Fig. 4.4).

The advantage of the MD-EXAFS method is a significant reduction of a number of free model parameters, which are required to describe the structure and dynamics of nano-objects. Only actual parameters are related to geometry (size and shape) and force-field model used in molecular dynamics simulations. All interatomic distances, bond angles, thermal and static disorder effects, and an influence of defects are obtained from MD simulations by calculating configuration averages from snapshots of instant atomic positions.

4.4.1 Development of the nanoparticle model

Before starting MD-EXAFS calculations one needs to define a structural model of the material: specify shape and size, defect (if any) concentration and distribution as well as the force-field (FF) parameters for the MD simulation.

Starting force-field parameters can be taken from the simulations of the bulk. It is important that they give realistic structure and properties of the material.

Bulk crystals were simulated in the isothermal–isobaric ensemble (NPT) with constant pressure and temperature using the supercell and 3D periodic boundary conditions. The half of the size of the supercell determines the longest distance from the absorbing atom which can be analyzed. For example, if we want to analyze coordination shells up to 6.5 Å, then the supercell dimensions should be larger than 13 Å. The NPT ensemble was chosen to allow the relaxation of the unit cell volume, not presuming any predefined value.

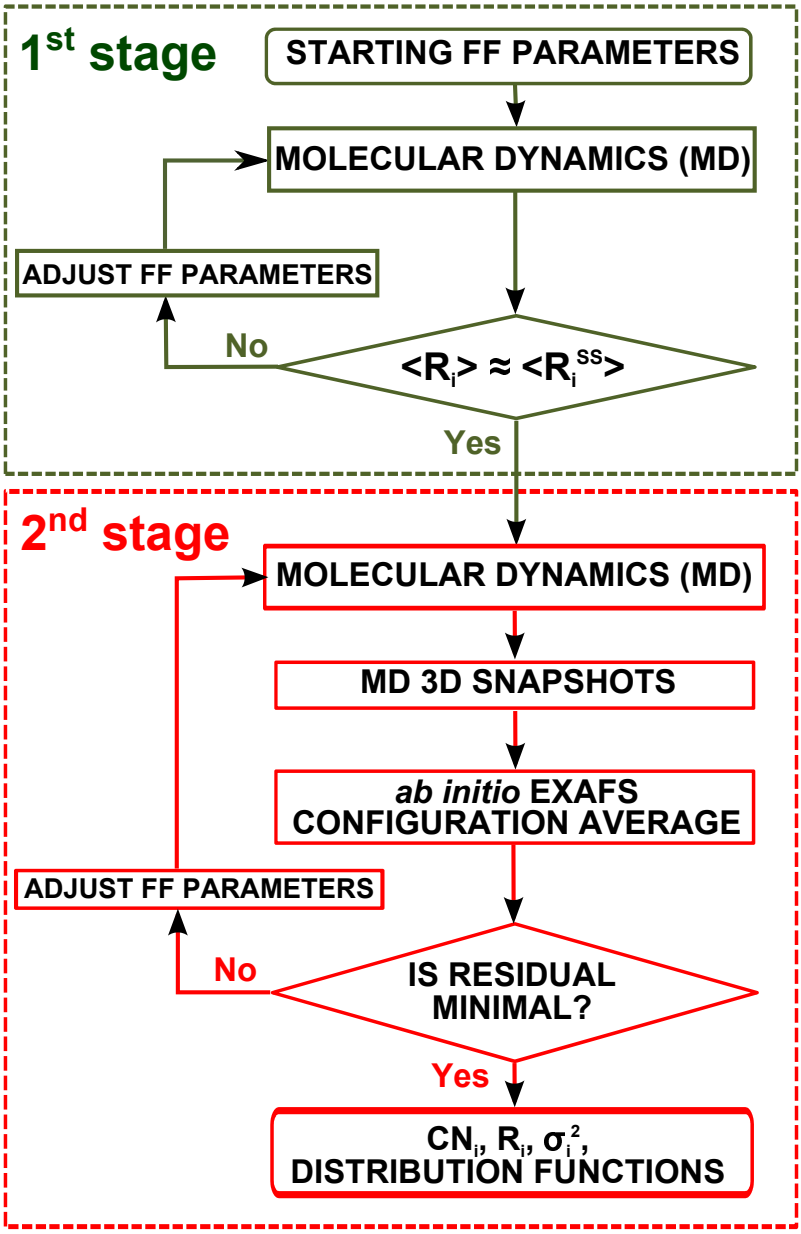

Figure 4.4: The scheme of MD-EXAFS calculations. The goal of the first stage is to find force-field (FF) parameters which give the mean values of interatomic distances for the first coordination shells being in agreement with those obtained from the conventional analysis of the experimental EXAFS spectrum or other structural analysis. Only those model nanoparticles which give this agreement within the desired precision are passed to the second step. The goal of the second step is to fine-tune FF parameters in order to minimize the residual between configuration-averaged multiple-scattering EXAFS spectrum of the model nanoparticle and experiment. One should find the model nanoparticle which gives the minimal residual value. After second phase one can use MD data to find all necessary properties of the selected model nanoparticle.

As we have shown in [31, 32], unfortunately the force-field parameters from the bulk cannot be directly transferred to nanoobjects. Therefore, in our MD-EXAFS method we have straightforward mechanism, how to adjust FF parameters using EXAFS spectra.

Nano-objects were simulated in the canonical ensemble (NVT) using appropriate shape clusters placed in a large enough empty box, which corresponds to the free nano-object in the vacuum. The size of this box should be big enough, to avoid self-interaction of the nano-object. In this case NVT ensemble was natural choice, because we do not want to change the volume of the box.

4.4.2 Details of the MD-EXAFS modeling

As the first step (Fig. 4.4), one needs to perform the MD simulations with the goal to find the values of the force-field parameters that result in the mean values of interatomic distances for the nearest coordination shells being in agreement (in our case, within ± 0.005 Å) with those obtained from the conventional analysis of the experimental EXAFS spectrum in the single-scattering approximation or other structural analysis (e.g. X-ray or neutron diffraction).

To understand a behavior of the model and to increase efficiency of the optimization procedure, it is important to study how the calculated mean distances in the nearest coordination shells depend on the force-field parameters.

For example, in the case of NiO, we found that both interatomic distances (R(Ni–O_1) and R(Ni–Ni_2)) show linear dependence on the Ni ion charge Z_{Ni} (Fig. 4.5). This result allowed us to save a lot of computing effort, by calculating the value of Z_{Ni}, which provides the desired value of the mean interatomic distance for the first or second coordination shell, using the linear dependence $R(Z_{Ni})$.

Summing up, the first step of the calculations (Fig. 4.4) is relatively fast screening procedure to tune the force-field parameters for different model nanoparticles and to select only those model particles, which have the desired structural parameters (e.g. distances of the first two coordination shells).

As the second step (Fig. 4.4), the agreement between the configuration-averaged and experimental EXAFS spectra was used as a goodness of model criterion.

At this step each model particle, selected at the first step, is processed. For every nanoparticle the configuration-averaged EXAFS spectrum was calculated using a set

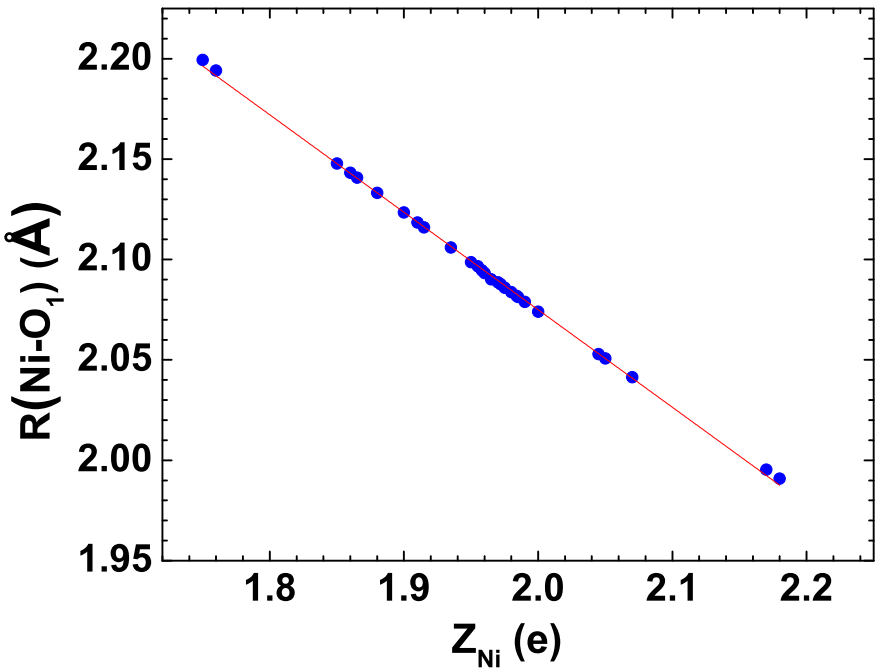

Figure 4.5: The calculated distance R(Ni–O_1) between the atoms in the first coordination shell of NiO model nanoparticle as a function of the Ni ion charge Z_{Ni}. Force-field parameters used in MD calculations come from [32]. Line represents linear fit of the modeled data.

of snapshots of instant atomic positions generated by MD simulation. For each MD snapshot the averaging of EXAFS spectra over all absorbing atoms in the particle is performed, because in nanoobjects every absorbing atom has different environment (depending on the distance from the surface and/or defects). In EXAFS calculations we use full potential of the multiple-scattering theory up to the 8th order and considered contributions from as many as possible coordination shells around the absorbing atom (usually this is about 6.5 Å).

Then configuration-averaged EXAFS spectra is calculated by averaging EXAFS spectra of all snapshots. Such approach allowed us to take into account disorder effects caused by atomic thermal vibrations and by structure relaxation due to the finite size of the particle and the presence of defects. A convergence of the configuration-averaged EXAFS spectrum was controlled by evaluating its variation upon an addition of the successive MD snapshot. The convergence was achieved when a change of the mean square difference between two configuration-averaged EXAFS spectra was below 10^{-4}.

This criterion is usually satisfied when one averages over the EXAFS signals from 4000 absorbing atoms. For large enough particles this means that even a single MD snapshot of the particle is enough to create configuration-average EXAFS spectrum. However, for smaller particles one needs many MD snapshots in order to collect 4000 signals and to achieve convergence.

Note that while the force-field parameters were optimized for each model particle at the first modeling step, FF parameters were additionally tuned around previously determined values by allowing small value variation in order to achieve the minimal value of the residual between model and experimental spectra.

At the end of the second step, one obtains optimal values of the force-field parameters for each selected model particle, which lead to the minimal residual between the configuration-averaged and experimental EXAFS spectra. By comparing residual values for different model particles, one can select the model particle, which provides the lowest possible residual for the given experimental EXAFS spectrum.

Our modeling procedure allows one to obtain not only the basic structural information like average interatomic distances, bond angles, MSRD values, coordination numbers, pair and many-atom distribution functions, which can be calculated from the atomic coordinates, but also to determine other properties of the model particle like phonon frequencies, elastic properties, etc., using the optimized force-field potential model [84].

4.4.3 Details of the MD and EXAFS calculations

For classical MD simulations we used GULP 3.1 [85] and DLPOLY 4.02 [86] codes, which are suitable for both bulk and nanosized materials. The integration of Newton's equations was performed by the leapfrog Verlet method. In each simulation, the structure was first equilibrated during 75 ps at 300 K and zero pressure, corresponding to conditions of the EXAFS experiments, and a set of instantaneous atomic configurations was accumulated during next 20 ps production run with a time step of 0.5-2.0 fs. Such time step is equivalent to the largest allowed change of the distance equal to 0.1 Å. The calculated sets of instantaneous atomic configurations were also used to evaluate the total and pair distribution functions (PDFs). These PDFs were further decomposed into a set of Gaussian functions to evaluate the values of coordination numbers CN, interatomic distances R and corresponding MSRDs σ^2.

4. EXAFS DATA ANALYSIS AND SIMULATIONS

The EXAFS spectra were calculated for each instantaneous atomic configuration and for all absorber atoms in each of these configurations using the *ab initio* real-space multiple-scattering FEFF8 code [50]. The scattering potentials and partial phase shifts were evaluated only once for the average configuration, thus neglecting a variation of the scattering potentials due to a disorder [23]. Since we are interested to account for the contributions from the outer coordination shells, it is important to take into account the multiple-scattering effects [32]. In our calculations for NiO, we considered the multiple-scattering contributions up to the eighth order with the half path length up to 6.5 Å. To reduce the number of scattering paths, they were filtered using the cut-off criteria (CRITERIA 0.0 1.7) as is implemented in the FEFF8 code [50]. This means that all paths with the mean amplitude of 1.7% and above of the largest path, estimated within the plane wave approximation, were kept. The inelastic losses were taken into account using the complex exchange-correlation Hedin-Lundqvist potential [22]. The cluster potential was of the muffin-tin (MT) type, and the values of the MT-radii for NiO were R_{MT}(Ni)=1.319 Å and R_{MT}(O)=1.021 Å.

5

Experimental

5.1 Sample preparation

Non-stoichiometric $Ni_{1-x}O$ nanoparticle powder (nano-NiO) was produced by the precipitation method [87], based on a reaction of aqueous solutions of $Ni(NO_3)_2 \cdot 6H_2O$ and NaOH, followed by subsequent annealing of the precipitate in air at 250°C.

Non-stoichiometric nanocrystalline $Ni_{1-x}O$ thin films were produced using reactive dc-magnetron sputtering of metallic nickel target and were deposited on three substrates (silicon, glass and polyimide tape). The film deposition was performed at three Ar/O_2 ratios equal to 0/100 (TF1), 50/50 (TF2) and 90/10 (TF3). Thus obtained thin films have dark brown color, suggesting the presence of nickel vacancies [88, 89, 90, 91].

Commercial microcrystalline NiO powder (c-NiO, Aldrich, 99%), having green color, was used for comparison.

Lead sulfide (nano-PbS) nanoparticles was synthesized using the method described in [92] and kindly provided to us by Dr. Boriss Polyakov. Microcrystalline PbS was commercial powder from Aldrich (99.9% trace metals basis).

$MeWO_4$ nanoparticles were synthesized using co-precipitation technique by the reaction of $Co(NO_3)_2 \cdot 6H_2O$ or $CuSO_4 \cdot 5H_2O$ and $Na_2WO_4 \cdot 2H_2O$ at room temperature (20°C), pH=8 [93, 94]. We used "as prepared" nanopowders, which were x-ray amorphous. Microcrystalline powders were produced by annealing of "as-prepared" powders at 800°C for 4-8 h in air.

5.2 X-ray powder diffraction

The crystallinity of samples was characterized by x-ray diffraction (XRD) using PANalytical diffractometer, Model X-Pert Pro MPD. It has high resolution vertical goniometer equipped with long fine focus ceramic tube, type PW3373/00, Cu anode, wavelength $\lambda = 0.154$ nm, max. $P = 2.2$ kW, $U = 60$ kV and PIXcel wide dynamic range solid-state detector.

5.3 Scanning electron microscopy

Morphology of the films were characterized by scanning electron microscopy (SEM) using Carl Zeiss EVO 50 XVP electron microscope. Tungsten cathode was used as a source of electrons. The accelerating voltage was 25 kV.

5.4 Micro-Raman spectroscopy

Micro-Raman scattering spectra were collected in back-scattering geometry at 20°C using a confocal microscope with spectrometer "Nanofinder-S" (SOLAR TII, Ltd.). The measurements were performed through Nikon Plan Apo 20× (NA=0.75) optical objective. DPSS laser (532 nm, 150 mW cw power) was used as the excitation source, and the Raman scattering spectra were dispersed by 1800 grooves/mm diffraction grating, having a resolution of about 2.5 cm^{-1} and mounted in the 520 mm focal length monochromator. The elastic laser light component was eliminated by the edge filter (Semrock LP03-532RE). Peltier-cooled back-thinned CCD camera (ProScan HS-101H, 1024x58 pixels) was used as a detector.

5.5 X-ray absorption spectroscopy

X-ray absorption spectra were measured in transmission mode at the HASYLAB/DESY C bending-magnet beamline [95]. The storage ring DORIS III operated at $E = 4.44$ GeV and I_{max}=140 mA. The x-ray radiation was monochromatized by a 40% detuned Si(111) double-crystal monochromator, and the beam intensity was measured using two ionization chambers filled with argon and krypton gases.

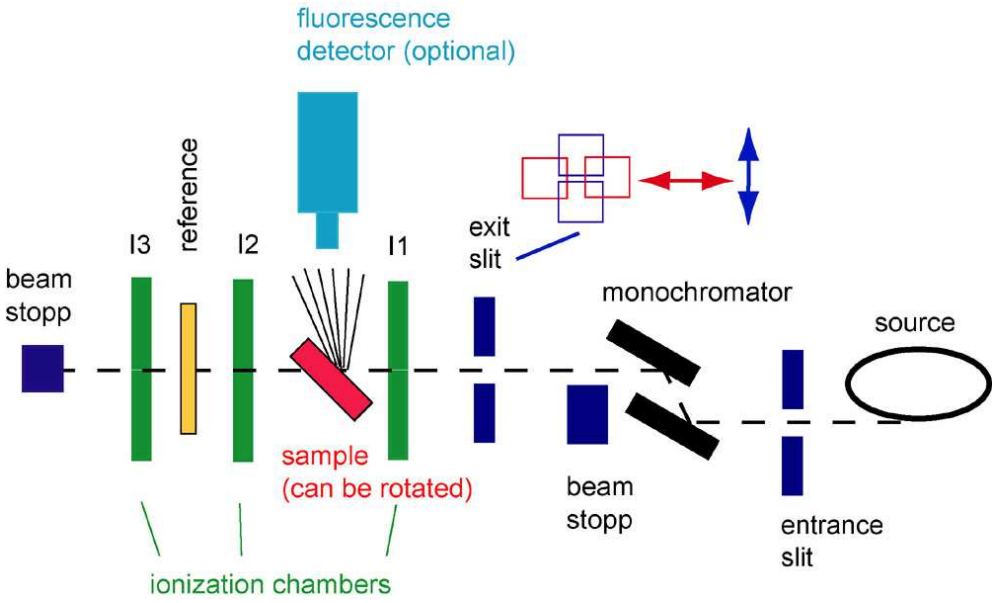

Figure 5.1: Schematic view of the EXAFS experiment at C beamline DORIS III storage ring. The setup consists of the x-ray source (the storage ring), variable entrance and exit slits, double-crystal monochromator, three ionization chambers (I1, I2 and I3), beam stopper. The position of the unknown and reference samples and the optional fluorescence detector (not used in the present work) are also shown (http://www.hasylab.de).

To achieve the absorption edge jump value $\Delta\mu \approx 1$, the proper amount of the sample powder was deposited on Millipore nitrocellulose membrane filter and fixed by Scotch tape, whereas a stack of simultaneously sputtered thin films was used. The relevant metal foil was used as the reference sample to control monochromator stability.

The Oxford Instruments liquid helium flow cryostat was used to maintain the required sample temperature, usually 6-300 K. The temperature was stabilized to within ± 0.5 degrees during each experiment.

6

Results and Discussion

6.1 Local structure of microcrystalline and nanosized NiO

Nickel oxide (NiO) is antiferromagnetic material [96, 97] with the Néel temperature $T_N = 523$ K. It has cubic rock-salt structure ($Fm\bar{3}m$) above T_N, undergoing weak cubic-to-rhombohedral distortion ($R\bar{3}m$) below T_N due to the magnetostriction effect [98].

Nickel oxide as a nanomaterial finds a broad range of practical applications including but not limited to catalysis [99], electrochromic devices [100], gas sensors [101], pressure sensors [102], resistive and magnetoresistive memory [103, 104], giant magnetoresistive spin valve structures [105, 106], rechargeable batteries [107], transparent conductors for solar cells [108], transparent electronics [109], light emitting diodes [110] and fuel cells [111]. NiO is known to be *p*-type semiconductor, having an oxygen excess due to the presence of nickel vacancies [88, 89, 90, 91]. Nickel vacancies are indicated by Rutherford back scattering measurements [89], by microthermogravimetric techniques [90, 112], by Hall mobility measurements [88], and by *ab initio* calculations [91].

Upon size reduction down to nanoscale, the influence of particle surface increases leading to atomic structure relaxation. An expansion of lattice volume has been found in nanosized NiO by x-ray diffraction [113, 114, 115, 116] (Fig. 6.1). This phenomenon is in line with the general behaviour of nanosized metal oxides [7, 11, 12], described in section 2.1, and in the case of nickel oxide was tentatively explained in [113, 116] by a negative pressure due to the repulsive interaction of the parallel surface defect dipoles at small particle sizes. The unit cell volume in NiO nanoparticles becomes equal to that

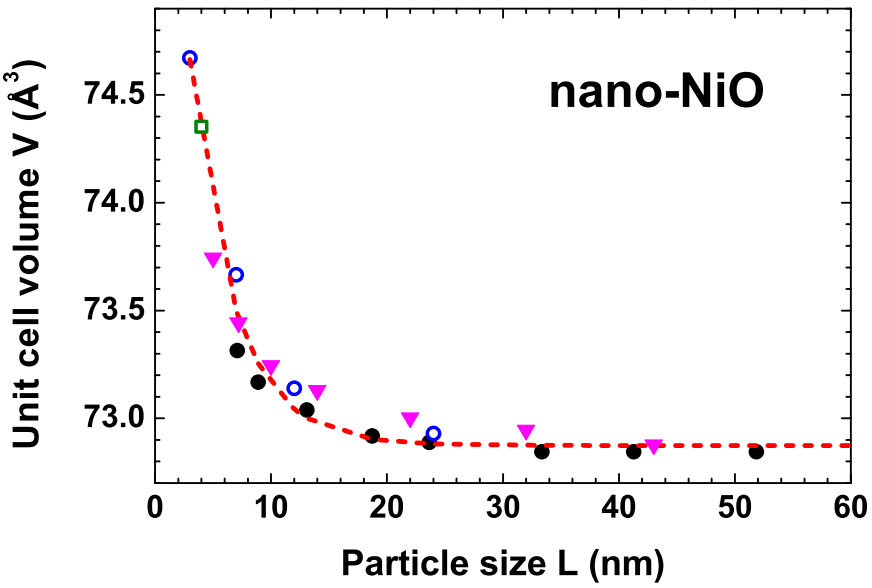

Figure 6.1: Dependence of the unit cell volume on the nanoparticle size (data taken from XRD studies, solid circles from [113], empty circles from [114], empty box from [115], solid triangles from [116]). Dashed line corresponds to the fitted formula $V = V_0 + A\exp(-L/B)$, where V is the unit cell volume (in Å^3), L is the particle size (in nm), $V_0 = 72.874$ Å^3, $A = 3.9419$ Å^3, B =3.8009 nm.

in the bulk nickel oxide for particle size above about 20 to 30 nm, taking into account the accuracy of the lattice constant determination in [113, 114, 115, 116].

EXAFS spectroscopy has been used to study nickel oxide for a long time since very beginning of the EXAFS till now [117, 118, 119, 120]. This continuous interest is caused by the practical importance of nickel oxide and by a fact that NiO is very convenient as model material due to its simple crystalline structure and, especially, as a material with strongly correlated electronic structure.

In many modern devices, like electrochromic cells [100] or giant magnetoresistive spin valve structures [106], NiO is used in a form of thin film. So it is not surprising that most of the works covering nanosized NiO have been dedicated to investigation of NiO thin films.

The in-plane and out-of-plane strains have been evaluated in the epitaxial ultrathin NiO layers on Ag(001) in [121, 122, 123], where authors showed that nickel oxide films have the rock-salt structure which is tetragonally strained to match the interatomic distances of silver substrate.

A decrease of the first shell average distance R(Ni–O_1) by ∼0.02 Å and an increases of the mean second shell distance R(Ni–Ni_2) by ∼0.01-0.02 Å have been observed in $Ni_{1-x}O$ thin films sputtered on polyimide tape by A. Kuzmin *et al.* in [124]. Estimated lattice parameter for thin films (4.20 and 4.21 Å) was in good agreement with data from X-ray diffraction (4.22 Å), which shows lattice expansion for nanosized nickel oxide clusters [124]. The average grain sizes of nickel oxide were estimated from the ratio of coordination numbers to be 2.1±0.3 nm and 3.4±0.3 nm for the thin films sputtered in mixed argon-oxygen atmosphere with 30% and 100% oxygen content, respectively [124].

Transparent hydrated $Ni_{1-x}V_xO_y$ thin films sputtered onto quartz and polyimide (kapton) have been studied by EXAFS in [125]. Results showed a decrease of the mean Ni–O distance by ∼0.02 to 0.04 Å, the second shell Ni–Ni distance increase by ∼0.01 to 0.02 Å, and the nanocrystal size estimated from the ratio of coordination numbers was about 1 nm [125].

Recently, the presence and the role of nickel vacancies have been studied using EXAFS and XRD in sputtered NiO films by W.L. Jang *et al.* [126, 127]. By analyzing a change of coordination number as a function of the annealing temperature, it was concluded that nickel vacancies, being the dominant point defects, are responsible for the electrical conductivity of the films [126]. Other finding is that Ni–O distance in a film annealed at 100°C is 2.045 Å (being smaller by 0.04 Å than the bulk value), and it approaches 2.084 Å (nearly equal to that in the bulk material) upon annealing at higher temperatures, whereas the Ni–Ni distances remain nearly unchanged [126]. A shortening of Ni–O distance was explained by the presence of Ni^{3+} ions, having smaller radius (0.56 Å) than Ni^{2+} (0.69 Å), in a neighbourhood of the nickel vacancies and by stronger attractive force between Ni^{3+} and O^{2-} [126]. At the same time, oxygen atoms surrounding nickel vacancy are displaced outward from it that may lead to the lattice expansion [126]. Besides, W.L. Jang *et al.* proposed that nickel vacancies are responsible for the thin film decomposition under annealing in vacuum above 400°C [127].

At the same time, very few works exist to our knowledge on the EXAFS studies of NiO nanoparticles.

An elongation of the first shell R(Ni–O_1) and second shell R(Ni–Ni_2) distances has been found in ultra fine NiO particles dispersed on activated carbon fibers [128].

In-situ EXAFS study of the initial crystallization stage of NiO nanoparticles from the amorphous precursor has been performed in [129].

Finally, the influence of point defects in NiO nanoparticles (having size 9.8, 12.5, and 17.3 nm) has been studied recently by S. Mandal *et al.* in relation to their magnetic properties [130]. Using two EXAFS data collection techniques, namely bulk sensitive transmission mode and near-surface sensitive conversion electron yield mode, they analyzed coordination numbers in the second coordination shell of nickel corresponding to the nearest neighboring Ni atoms. Coordination numbers become smaller as the particle size decreases. Authors proposed that the smallest nanoparticles (9.8 nm) have the largest nickel vacancy concentration (10.3% detected by near-surface sensitive technique and 5.2% detected by bulk sesitive technique), claiming that most of the vacancies are concentrated on the nanoparticle surface [130]. They argue that there are no signs of the Ni^{3+} in nickel oxide nanoparticles [130].

As one can see, there is plenty of room in studies of nanosized nickel oxide in order to clarify the controversial data on the structure and role of nickel vacancies.

6.1.1 XRD studies of NiO nanoparticles and surface morphology of thin films

The crystallinity of the samples was characterized by x-ray diffraction (XRD) and morphology of thin films was studied by scanning electron microscopy (SEM) (methods described in section 5).

According to the XRD data (Fig. 6.2), the structure of all samples correspond to the NiO having cubic rock-salt crystal structure ($Fm\bar{3}m$).

Using the Scherrer's method, and assuming the cubic particles shape, we have found that the average size of nanoparticles was 6.2±1.8 nm in the nanopowder and 6±1 nm (TF3), 12±1 nm (TF2) and 17±1 nm (TF1) in the thin films. So the XRD data suggest that the crystallinity of the films is influenced by the sputtering atmosphere, i.e. Ar/O_2 ratio, and the nanocrystallites in the thin film TF3 are smaller than in the nanopowder.

Note that our thin films with larger crystallite size have preferable crystallite orientation (100), but it changes to (110) and (111) upon decreasing the size of the crystallites.

SEM images of $Ni_{1-x}O$ thin films (Fig. 6.3), simultaneously deposited on silicon, glass and polyimide substrates by dc magnetron sputtering at the gas ratio Ar/O_2 =

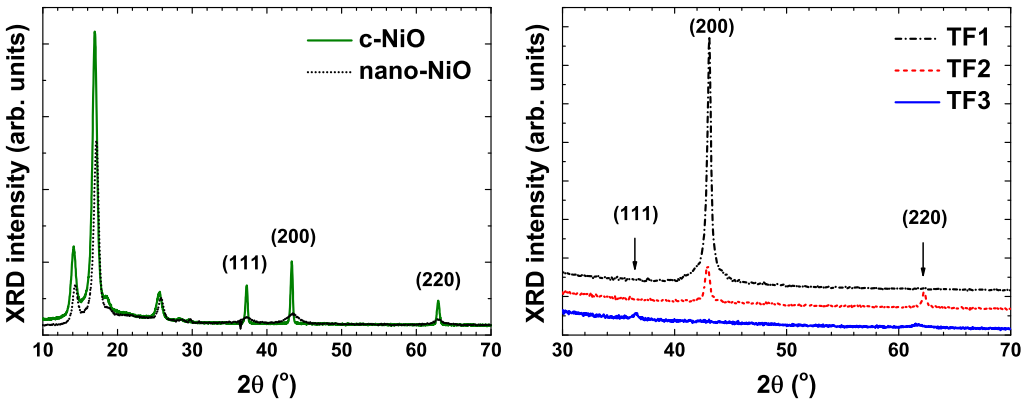

Figure 6.2: Left panel: XRD patterns of NiO nanopowder (nano-NiO) and microcrystalline NiO (c-NiO). Right panel: XRD patterns of $Ni_{1-x}O$ thin films prepared at three Ar/O_2 gas ratios equal to 0/100 (TF1), 50/50 (TF2) and 90/10 (TF3).

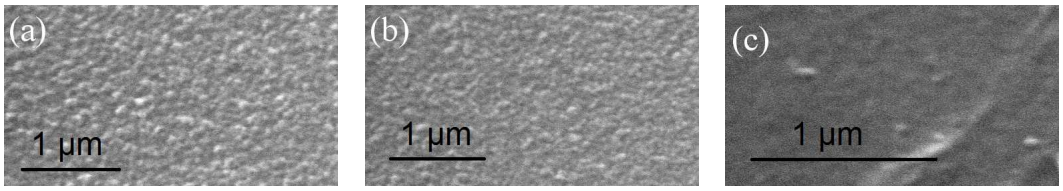

Figure 6.3: SEM images of $Ni_{1-x}O$ thin films with Ar/O_2=90/10 simultaneously sputtered on (a) silicon, (b) glass and (c) polyimide film.

90/10, reveal that their morphology strongly depends on substrate material. Films deposited on polyimide tape have the smoothest surface, but those deposited on silicon have the coarsest surface.

6.1.2 X-ray absorption spectroscopy

The Ni K-edge x-ray absorption spectra were measured in transmission mode at the HASYLAB/DESY C1 bending-magnet beamline in the temperature range from 6 K to 300 K. The XANES and EXAFS oscillations $\chi(k)$ were extracted and analyzed following the conventional procedure [28] using the EDA software package [56] (for details see Sec. 4.2).

6.1.2.1 XANES

The normalized to the absorption edge jump Ni K-edge XANES signals for microcrystalline and nanocrystalline nickel oxide are compared in Fig. 6.4. They are composed

of the low energy pre-edge peak A at ∼8335 eV, followed by the wide feature B at ∼8340 eV, the main maximum at ∼8347 eV, and the fine structure above it. The two XANES signals are very close, except that the main maximum and the broad peak at ∼8400 eV have slightly higher intensity in c-NiO. The pre-edge region of the XANES provides with the information on the local electronic structure at the absorbing Ni atoms in the presence of the core-hole. In particular, the Ni K-edge absorption is caused by the transition of a 1s electron of nickel from its core atomic state to a final unoccupied state following to dipole ($\Delta l = \pm 1$) or quadrupole ($\Delta l = 0, \pm 2$) selection rules. Note that the final state is a relaxed excited state due to the presence of a 1s core hole screened by the other electrons of nickel.

The interpretation of the Ni K-edge XANES in NiO has been a topic of extensive studies in the past [119, 124, 131, 132, 133, 134, 135, 136]. The use of the multiple-scattering approach allowed understanding the origin of main peaks to be due to the scattering by atoms of the first ten coordination shells surrounding the absorber [131, 133]. The pre-edge peak A (Fig. 6.4) was assigned to the quadrupole 1s→3d transition from the analysis of resonant x-ray magnetic scattering in [132]. Its quadrupole origin was also supported by several theoretical calculations [119, 134, 135].

In the recent work [136], the DFT+U calculation scheme, i.e., the density-functional theory (DFT) with the Hubbard-U correction obtained by linear response, within the spin-polarized generalized gradient approximation (GGA) was applied to the analysis of Ni K-edge in NiO. It was found that the pre-edge peak A consists of two contributions: (i) a quadrupole part caused by the intrasite 1s(Ni)→3d(Ni) excitations lowered by core-hole attraction, and (ii) a very small dipolar component due to the 3d(Ni)-2p(O) hybridization between nearest Ni and O atoms [136]. At the same time, the next feature B of dipolar origin (Fig. 6.4) has nonlocal nature, caused by hybridization of on-site Ni empty 4p states with empty 3d states of the Ni atoms located in the fourth coordination shell [136] and participating in the 180° Ni–O–Ni antiferromagnetic interactions. Due to the nonlocal origin of the feature B, its position is insensitive to the core-hole attraction and, thus, the A-to-B peak separation can be used to estimate the value of the charge transfer gap in NiO [136]. The similarity of the XANES signals in bulk c-NiO, nano-NiO, and TF3 (Fig. 6.4) suggests the closeness of their electronic structures: in particular, one can conclude that no significant changes in the spin ordering should occur in NiO upon a decrease of the particles size down to ∼6 nm.

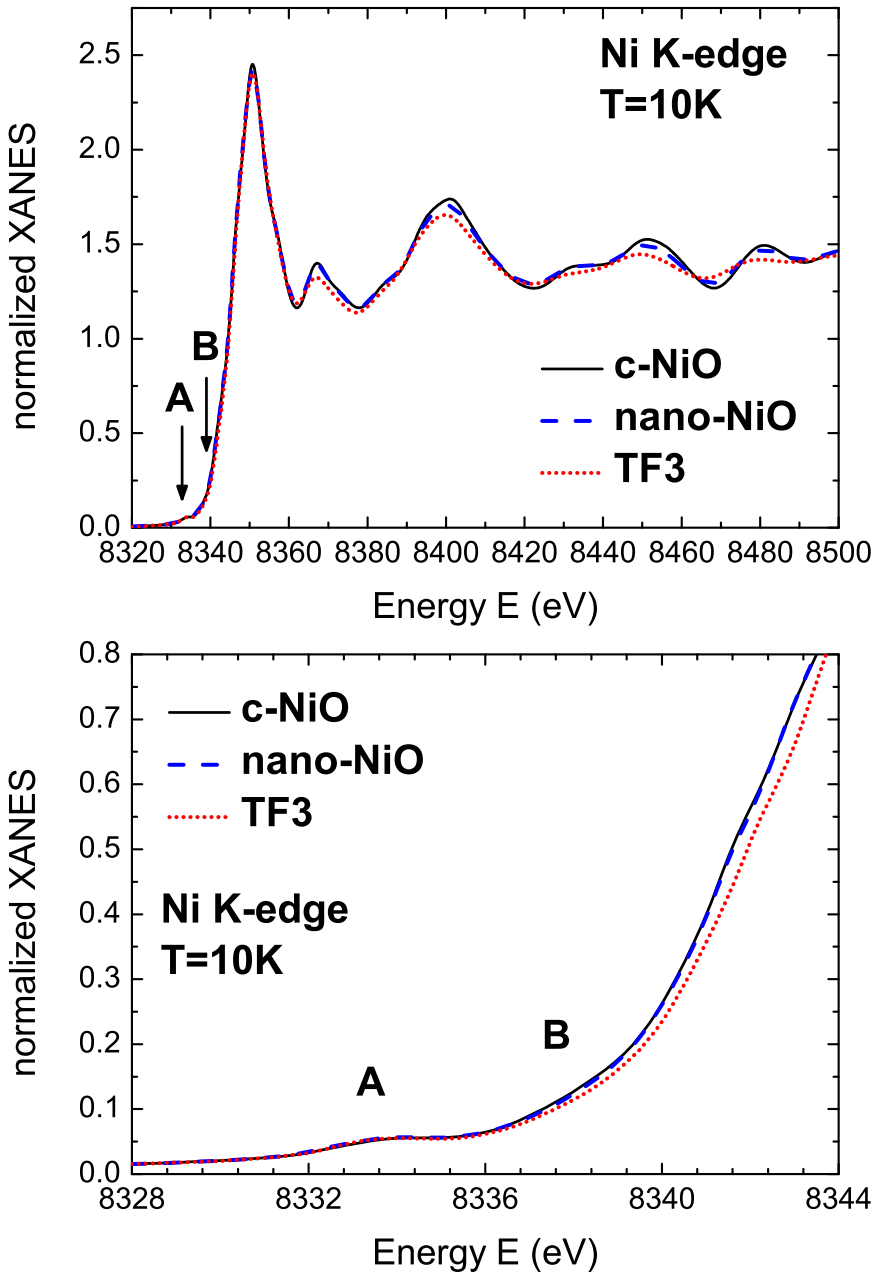

Figure 6.4: Upper panel: Experimental Ni K-edge XANES in c-NiO (solid lines), nano-NiO (blue dashed lines) and TF3 (red dotted line) at 300 K. The position of the pre-edge peak A (quadrupole transition to 3d(Ni)) and next feature B (dipole transition to hybrid 4p(Ni) and 3d($Ni_{4th\ shell}$)) are indicated by arrows. Lower panel: enlarged region of the pre-edge peak A.

6.1.2.2 Conventional analysis of the EXAFS data

The low temperature ($T = 10$ K) experimental Ni K-edge EXAFS spectra $\chi(k)k^2$ and their Fourier transforms (FT) for selected NiO samples are shown in Fig. 6.5. As one can see, the obtained EXAFS data for all samples have good quality in a wide k-space range up to 18 Å^{-1}.

There is a noticeable difference between the EXAFS spectra of nano- and micro-crystalline samples (Fig. 6.5). When comparing these spectra with the particle size estimations from XRD data, one can see that the damping of the signal increases upon decreasing of the particle size. Also one can notice the shift of the FT peak positions starting from the second peak to the larger distances upon a decrease of the particle size. This indicates clearly the lattice volume expansion in nanocrystalline NiO which will be analyzed in details further.

At the same time, one can see that the shape of EXAFS spectra for all samples is rather close. This means that there are no significant changes in the structure of NiO nanoparticles compared with the bulk NiO reference sample.

The EXAFS spectra for all samples show significant temperature dependence (see, for example, the case of nano-NiO in Fig. 6.6), suggesting that the thermal disorder effects are important and are not masked by structural disorder.

A comparison of simulated Ni K-edge EXAFS spectra for c-NiO taking into account only single-scattering or all multiple-scattering (up to 8th order) contributions is shown in Fig. 6.7. The two Fourier transforms of the EXAFS spectra differ at the distances longer than ∼3.2 Å, i.e. above the second peak, thus confirming that the single-scattering approximation is valid for the first two coordination shells of nickel atoms [31, 32].

Based on this knowledge we have performed conventional analysis for the first two coordination shells of nickel atoms [26, 27, 31, 32], by isolating them using the Fourier filtering procedure in the R-space range of 0.7-3.2 Å and best fitted in the k-space range of 2-17 Å^{-1} using the two-component Gaussian model [28] (see Sec. 3.2). The scattering amplitude and phase shift functions for the Ni–O_1 and Ni–Ni_2 atom pairs, used in the fits, were extracted from the low temperature ($T = 6$ K) experimental data of c-NiO sample, assuming the crystallographic value of the lattice parameter $a_0 = 4.1769$ Å [137] and six nearest neighbors in the first coordination shell and twelve

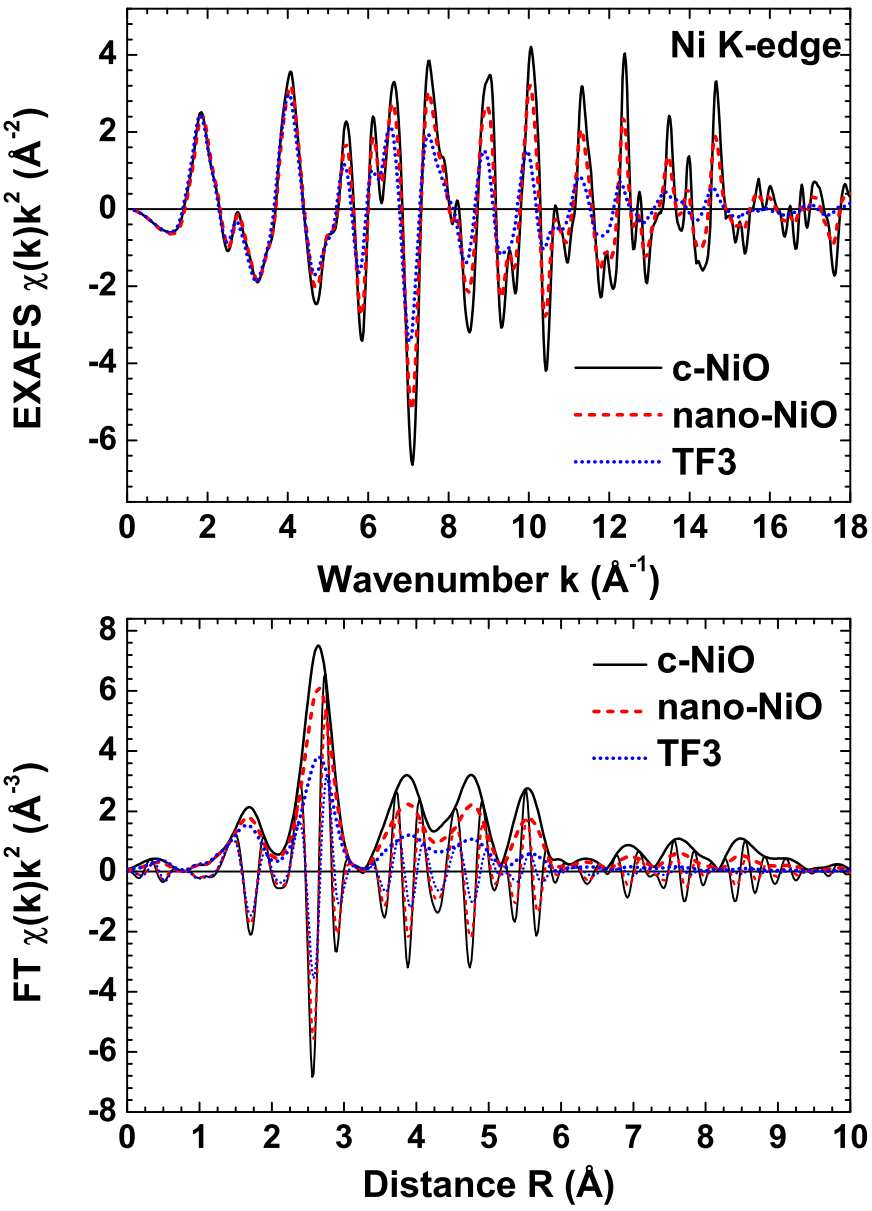

Figure 6.5: Low temperature ($T = 10$ K) Ni K-edge EXAFS spectra $\chi(k)k^2$ and their Fourier transforms (FTs) for c-NiO, nano-NiO and TF3. There is noticeable signal damping upon a decrease of the size of particles (going from c-NiO to nano-NiO and, next, to TF3). Note also a small shift of the peak positions in FTs to larger distances upon a decrease of the particle size.

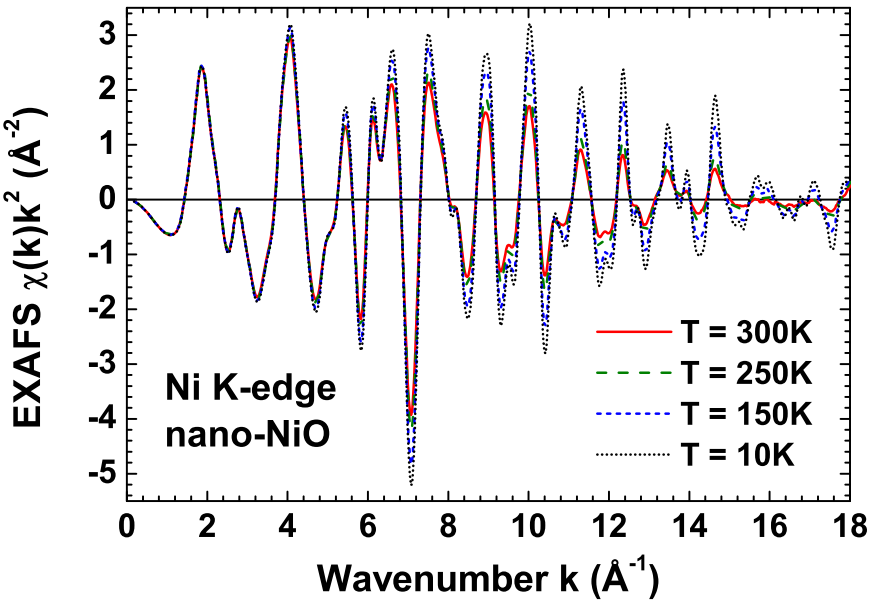

Figure 6.6: The Ni K-edge EXAFS spectra $\chi(k)k^2$ for nano-NiO at selected temperatures. Thermal disorder is responsible for the oscillation damping at high-k values.

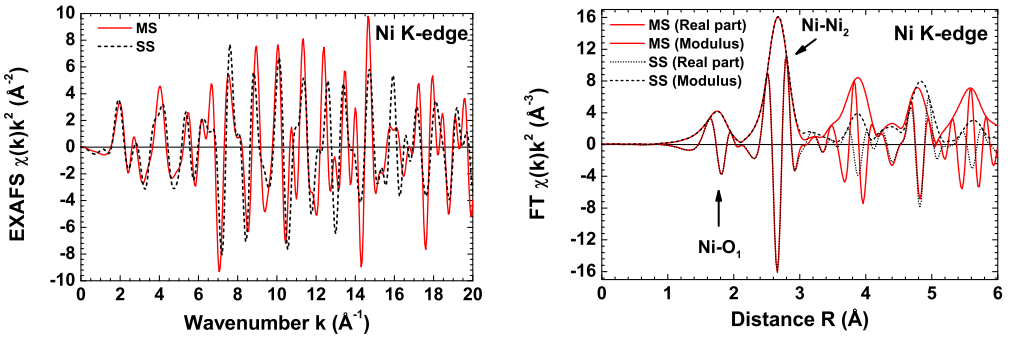

Figure 6.7: Theoretical Ni K-edge EXAFS spectra for c-NiO calculated using all multiple-scattering (MS) contributions and only single-scattering (SS) contributions. These calculations were performed without accounting for thermal damping (all MSRD parameters $\sigma^2 = 0$) and setting $S_o^2 = 1$. As one can see from the comparison of Fourier transforms, the MS contributions are not present in the first and second coordination shells of Ni atoms.

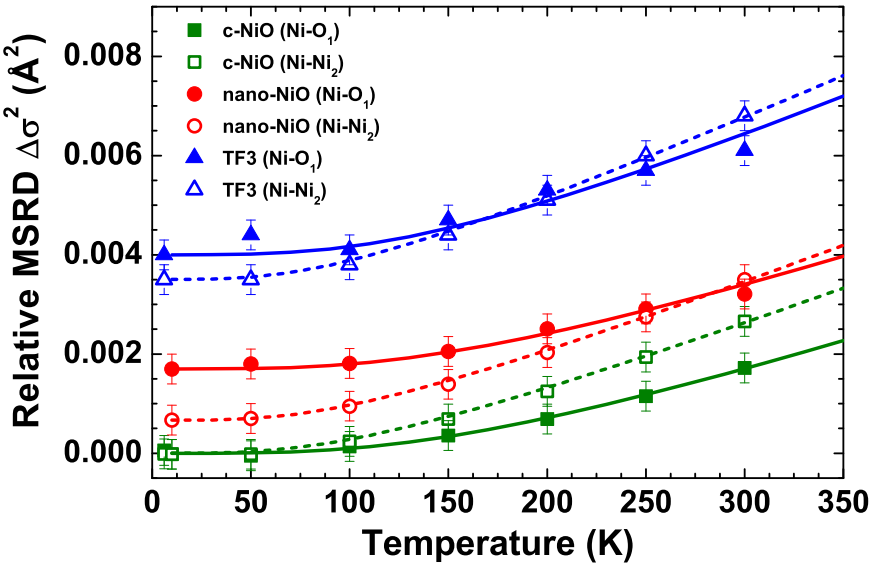

Figure 6.8: Temperature dependence of the mean-square relative displacements (MSRD) $\Delta\sigma^2 = \sigma^2(T) - \sigma^2(\text{c-NiO}, T = 6\text{ K})$ for the first (Ni–O_1) and second (Ni–Ni_2) coordination shells in c-NiO, nano-NiO and TF3 relative to the MSRD value in c-NiO at $T = 6$ K. The Debye models are shown by lines. See text for the values of the characteristic Debye temperatures.

in the second coordination shell of nickel. The obtained temperature dependencies of the mean-square relative displacements (MSRDs) σ^2 and interatomic distances R are shown in Figs. 6.8 and 6.9, respectively. Note that thus determined MSRD values are relative to the low temperature c-NiO data, i.e. $\Delta\sigma^2(T) = \sigma^2(T) - \sigma^2(\text{c-NiO}, T = 6\text{ K})$.

The difference between temperature dependencies of the MSRDs (Fig. 6.8) for nano- and microcrystalline NiO samples remains nearly constant in the whole range of temperatures in both the first and second coordination shells. The constant difference gives clear evidence of the static disorder in nanocrystalline NiO, which is induced by a relaxation of its atomic structure. At the same time, the thermal disorder contribution $\sigma^2(T)$ into the MSRD is close in all samples but differs for the first and second coordination shells, as expected. It can be well approximated by the Debye model [138, 139]

$$\sigma^2_{\text{D}}(T) = \frac{3\hbar}{M}\int_0^{\omega_{\text{D}}} (\omega/\omega^3_{\text{D}})\coth(\hbar\omega/(2k_{\text{B}}T))\left[1 - \frac{\sin(\omega R_0/\nu_s)}{(\omega R_0/\nu_s)}\right] d\omega \qquad (6.1)$$

where $\hbar$ is the Plank constant, M is the atomic mass, $\omega_{\text{D}} = k_{\text{B}}\theta_{\text{D}}/\hbar$ is the characteristic Debye (cutoff) frequency, k_B is the Boltzmann constant, θ_{D} is the characteristic Debye

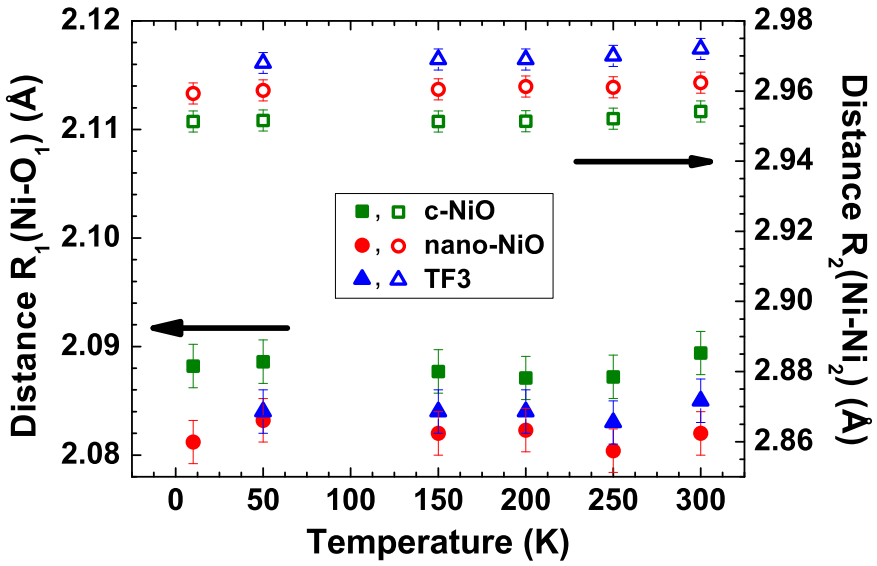

Figure 6.9: Temperature dependence of the average interatomic distances in the first (Ni–O_1, labeled with full markers) and second (Ni–Ni_2 labeled with open markers) coordination shells of nickel in c-NiO (squares), nano-NiO (circles) and TF3 (triangles).

temperature, R_0 is the equilibrium distance between the two atoms, and ν_s is the sound velocity in the crystal. Note that the second term in square brackets describes the correlation effects.

The obtained values of the characteristic Debye temperatures [26] are θ_D(Ni–O_1)=680 K and θ_D(Ni–Ni_2)=425 K for c-NiO; θ_D(Ni–O_1)=680 K and θ_D(Ni–Ni_2)=415 K for nano-NiO; and θ_D(Ni–O_1)=600 K and θ_D(Ni–Ni_2)=390 K for tf-NiO. These values are consistent with those, θ_D(O)=719 K and θ_D(Ni)=366 K, derived in [140] from the bulk thermal vibration amplitudes of nickel and oxygen atoms, obtained within the Debye model by high-resolution 120 keV He^+ ion scattering at room temperature, and also with the results of heat capacity measurements, θ_D(O)=900 K and θ_D(Ni)=425 K ([141]), θ_D(O)=762.5 K and θ_D(Ni)=515.9 K ([142]).

The average second shell distance R_2(Ni–Ni_2) in nanocrystalline samples is longer by ∼0.008 Å in nano-NiO and by ∼0.015–0.018 Å in NiO thin films than that in microcrystalline c-NiO at all temperatures (see Table 6.1 and Fig. 6.9). Such temperature dependence of the R_2(Ni–Ni_2) distance agrees well with a weak positive thermal expansion in NiO nanocrystals, which is nearly equivalent to that observed in bulk NiO [115]. From R_2(Ni–Ni_2) distance we can calculate effective lattice constant for cubic

Table 6.1: Values of the structural parameters for the first two coordination shells in microcrystalline NiO (c-NiO), NiO nanoparticles (nano-NiO) and NiO thin films (TF1, TF2, TF3), obtained from the best-fit of the EXAFS signals within the Gaussian approximation. N_i is the coordination number, ΔR_i (± 0.002 Å) is the interatomic distance relative to c-NiO, $\Delta\sigma_i^2$ (± 0.0003 Å^2) is the MSRD relative to c-NiO, a_0 is the lattice parameter ($a_0 = \sqrt{2}R_2$), V is the unit cell volume calculated from a_0 ($V = a_0^3$), which allows to estimate the particle size $L(V)$ according to Eq. 6.2. For reference c-NiO a_0 is equal to 4.17693 Å and $V_0 = 72.874$ Å^3.

	c-NiO	nano-NiO	TF1	TF2	TF3
			Ni–O_1		
N_{O1}	6.0	6.0	6.0	6.0	6.0
ΔR_1 (Å)	0.000	-0.007	-0.004	-0.009	-0.004
$\Delta\sigma_1^2$ (Å^2)	0.0000	0.0012	0.0028	0.0038	0.0045
			Ni–Ni_2		
N_{Ni2}	12.0	11.1	9.9	9.6	9.2
ΔR_2 (Å)	0.000	0.008	0.015	0.016	0.018
$\Delta\sigma_2^2$ (Å^2)	0.0000	0.0008	0.0019	0.0032	0.0037
a_0 (Å)	4.177	4.188	4.197	4.199	4.202
V (Å^3)	72.87	73.48	73.95	74.06	74.21
$L(V)$ (nm)	n/a	7.1	4.9	4.6	4.1

lattice $a_0 = \sqrt{2}R_2$ and corresponding unit cell volume $V = a_0^3$. The obtained data are in agreement with the overall unit cell volume expansion upon a decrease of NiO nanocrystal size observed by diffraction [113, 114, 115, 116].

The dependence of the unit cell volume V on the size L of the nanoparticles can be described by the empiric formula (see Fig. 6.1)

$$V = V_0 + Ae^{-\frac{L}{B}}, \tag{6.2}$$

where V_0 corresponds to the unit cell volume of the bulk NiO ($V_0 = 72.874$ Å^3), and A and B are two empirically determined constants ($A = 3.9419$ Å^3 and $B = 3.8009$ nm). It was used to estimate the size of the nanoparticles L (Table 6.1) from the R_2(Ni–Ni_2) distances determined by EXAFS (Fig. 6.9). Thus obtained L values can be compared with those determined using Scherrer's method (see Table 6.3 below): they are close to those found for nano-NiO, but are smaller than those for NiO thin films.

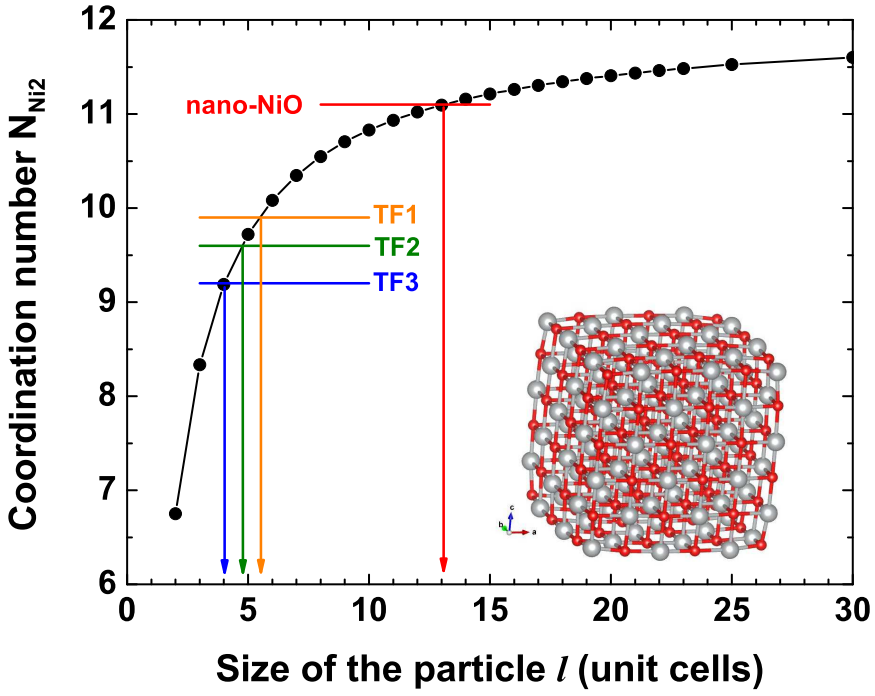

Figure 6.10: Dependence of the average coordination number N_{Ni_2} in the second shell of nickel on the cubic nanoparticle size ($L = la_0$). The parameters for nanocrystalline samples are indicated. The inset shows the relaxed nanoparticle model with $l = 3$ ($3 \times 3 \times 3$ unit cells).

We can calculate the average coordination number for the second shell of Ni atoms for ideal cubic particles. This value approaches 12 (the value for the ideal infinite crystal) for large particles and reduces upon a decrease of the nanoparticle size (Fig. 6.10). The reason of this is the under-coordination of the nickel atoms at the surface. This effect gives us another method to estimate the size of the nanoparticles from the coordination numbers, so that the average size of the particles in our samples is: 5.4 nm for nano-NiO, 2.5 nm for TF1, 2.1 nm for TF2, and 1.7 nm for TF3. Note that one should be very careful when using coordination numbers for any conclusions, because they are subject to systematic errors and other factors, including the presence of vacancies and particle shape. However, in our case, they give good estimate and feeling about the observed trend, which is in line with the results from XRD.

On the contrary to the second shell behavior, the average first shell R_1(Ni–O_1) distance in all nanocrystalline samples is shorter compared with microcrystalline NiO (Fig. 6.9, Table 6.1). This interesting result has been found by us [31, 32] in nanosized NiO powder at room temperature and is confirmed in a wide temperature range for differently prepared NiO nanocrystalline samples [26, 27]. This can be a result of the non-uniform relaxation of the atomic structure (distances) in nanoparticles. One obvious example is the interatomic distances on the surface. This phenomenon should be studied in more details, by using advanced methods of EXAFS analysis.

6.1.2.3 Modeling of NiO crystal and ideal nanoparticles with MD-EXAFS

To reveal the fine details of the structure relaxation in NiO nanoparticles, we used a more rigorous approach [26, 27, 31, 32], based on the MD-EXAFS method [23], which is described in details in Section 4.4.

Crystalline NiO was modeled in the isothermal–isobaric ensemble (NPT) with constant pressure and temperature using the supercell size 6×6×6 and 3D periodic boundary conditions [26].

Nanosized nickel oxide particles were simulated in the canonical ensemble (NVT) using cubic shape clusters $L \times L \times L$ placed in a large empty box, which corresponds to the free NiO particle in a vacuum [26]. They were generated from cubic rocksalt-type unit cell having the symmetry $Fm\bar{3}m$ (space group 225) and containing 4 nickel and 4 oxygen atoms (Fig. 6.11). The cluster size was up to $L = 40a_0$, where a_0=4.1773 Å is lattice parameter of c-NiO [57].

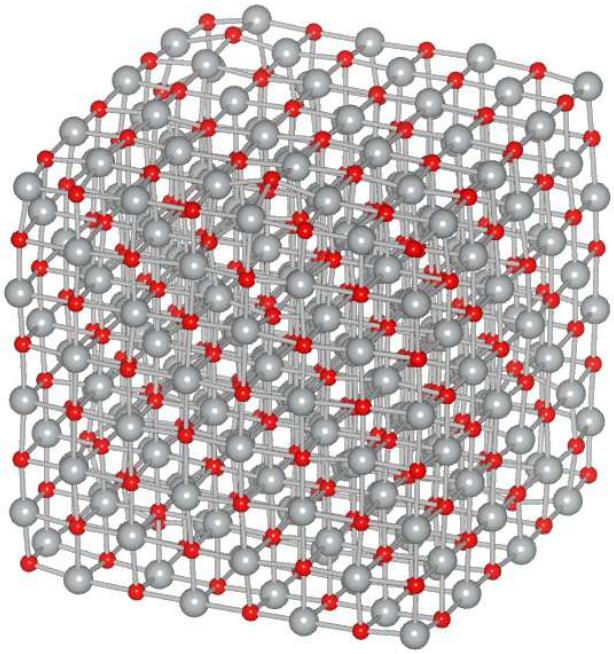

Figure 6.11: Example of the single MD snapshot of a nanoparticle with the size $l = 9$ unit cells. Small red balls represent oxygen atoms, large gray balls represent nickel atoms.

Table 6.2: Force-field model parameters of the Buckingham potentials for the Ni–O and O–O atom pairs used in the molecular dynamics simulations.

Pair of atoms	A (eV)	ρ (Å)	C (eVÅ^6)
Ni–O	754.92	0.3277	0.0
O–O	22764.3	0.1490	27.89

Our force-field (FF) potential model included two-body central force interactions between atoms i and j described by a sum of the Buckingham and Coulomb potentials

$$U_{ij} = A_{ij} \exp(-r_{ij}/\rho_{ij}) - \frac{C_{ij}}{r_{ij}^6} + \frac{Z_i Z_j e^2}{r_{ij}}. \tag{6.3}$$

The Buckingham potential parameters A, ρ, and C are reported in Table 6.2. They were taken from simulations of c-NiO [32, 143] using the formal charges of ions (Z_{Ni}=+2.0 for nickel atoms and Z_{O}=–2.0 for oxygen atoms) and reproduce well such properties of bulk crystal as lattice constant, elastic constants, bulk modulus and static dielectric constant [143].

The FF model developed for bulk NiO should be adopted to the case of nanoparti-

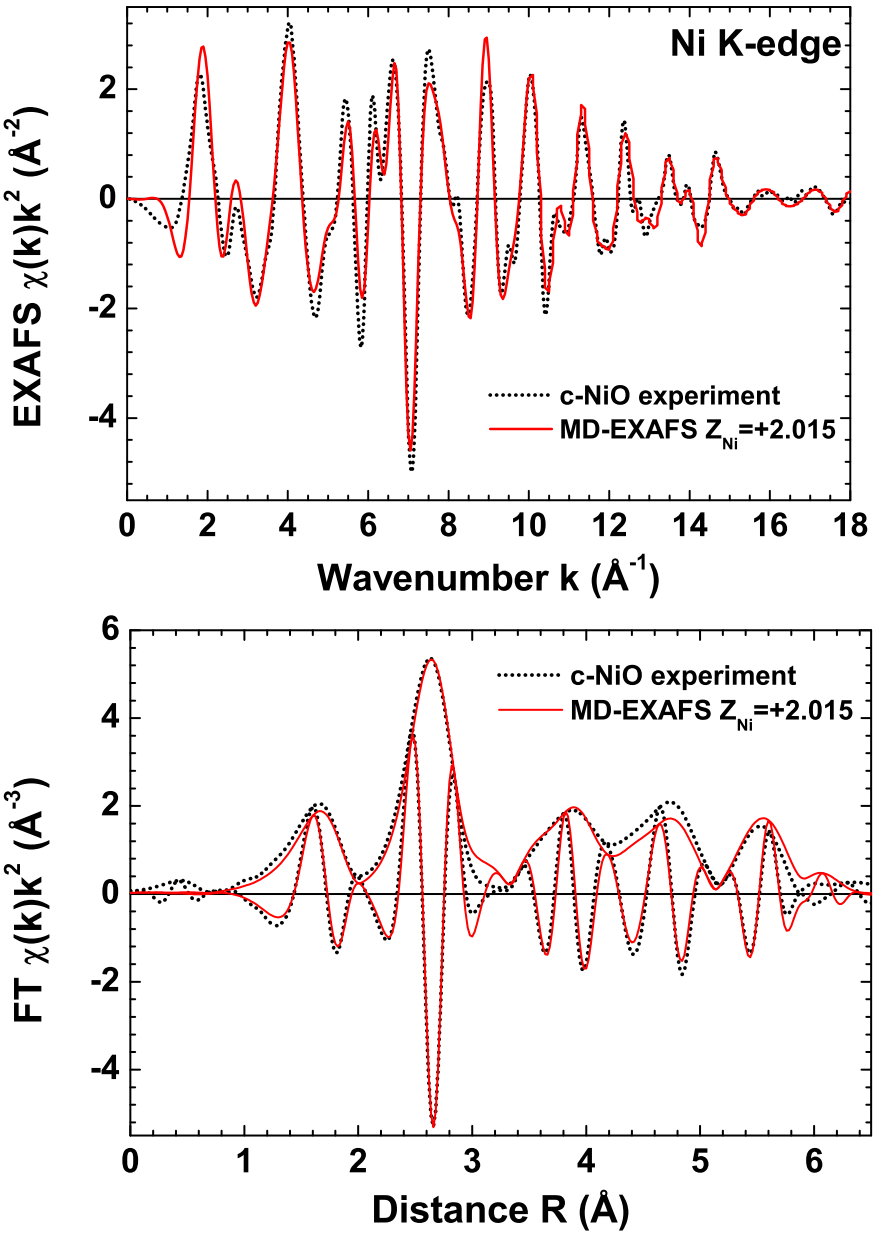

Figure 6.12: Experimental Ni K-edge EXAFS spectra for microcrystalline NiO (c-NiO) compared with the model spectra, obtained using MD-EXAFS procedure described in Sec. 4.4 and the optimized value of the nickel ion charge Z_{Ni}=+2.015.

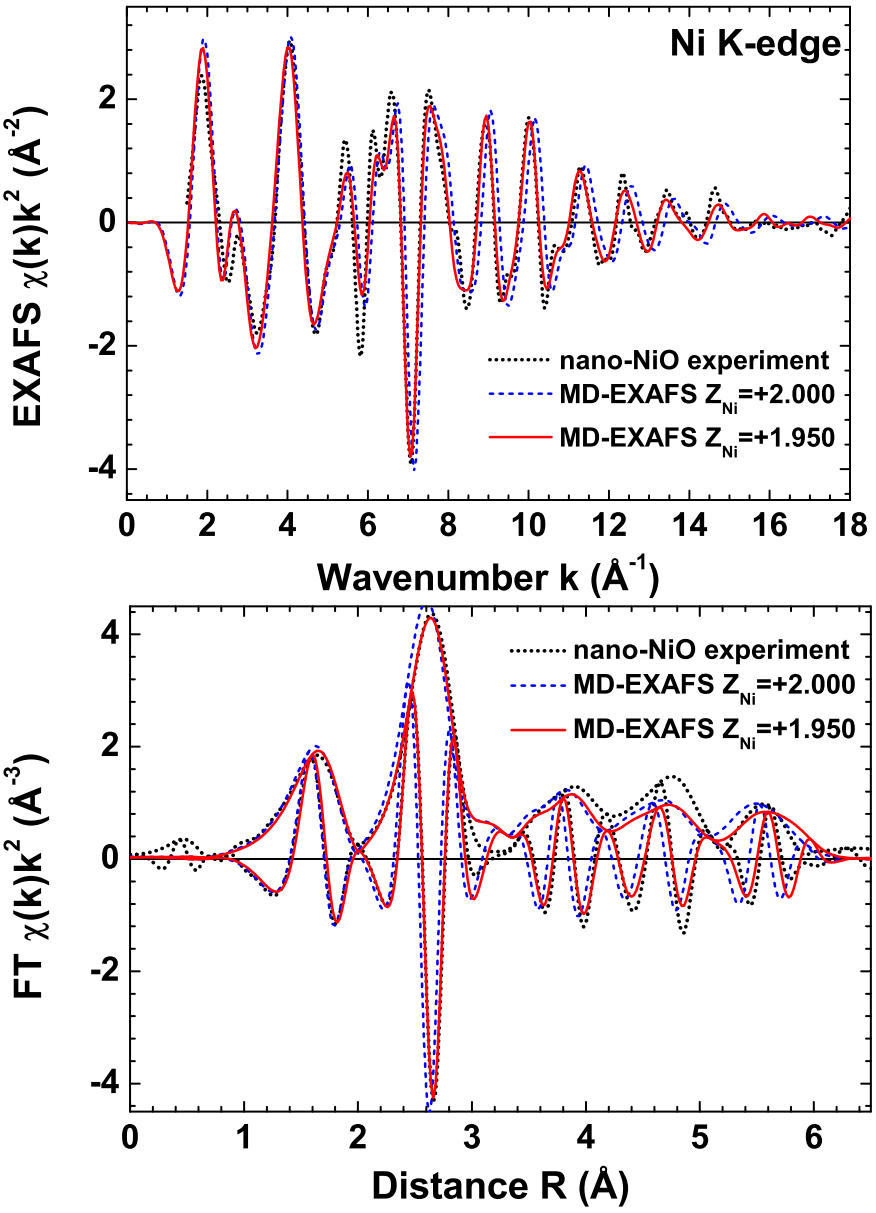

Figure 6.13: Experimental Ni K-edge EXAFS spectra for nano-NiO compared with the model spectra of the ideal nanoparticle (no vacancies) with ion charges used from the bulk NiO model (Z_{Ni}=+2.0 and Z_{O}=-2.0) and optimized ones (Z_{Ni}=+1.95 and Z_{O}=-1.95, obtained using MD-EXAFS procedure described in Sec. 4.4. The size of the model nanoparticle is 6×6×6 unit cells.

cles [31, 32]. In this study we selected the charge of nickel atoms Z_{Ni} as the optimization parameter to minimize the residual between experimental and calculated EXAFS signals. All other Buckingham potential parameters were left unchanged. Such choice is justified by the fact that the lattice dynamics of c-NiO and of nanocrystalline samples is close at all studied temperatures (Fig. 6.8), and the difference in the static part of the MSRDs is attributed to atomic structure relaxation. The charge of the oxygen atoms Z_{O} for the bulk and nanoparticles without defects is equal to -Z_{Ni} to maintain electroneutrality of the system.

As the first application of the previously described MD-EXAFS procedure (Sec. 4.4) we optimized FF parameters (in our case the ion charge of nickel) for experimental EXAFS spectrum of microcrystalline NiO (c-NiO). The minimal value of the residual for EXAFS spectrum was achieved with Z_{Ni}=+2.015 and corresponding Z_{O}=-2.015 [26]. This is a small change compared to the initial values ±2.0, that gives us confidence in selected procedure and our FF model (Fig. 6.12).

At the next step we have considered the model of defect-free cubic NiO nanoparticles [31, 32].

As we have noted in [31], the force-field potential parameters cannot be directly transferred from a crystal to nanoparticles, since they lead to the incorrect values of the interatomic distances and to the incorrect relaxation, which can be clearly observed in EXAFS signal as seen in Fig. 6.13. This is an interesting issue indicating that simple force-field model is not fully transferable from bulk to nanoobjects. In the case of NiO, if one uses the force-field parameters developed for the bulk NiO (c-NiO), the interatomic distances in nanoparticle become smaller than in the bulk material, which is controversial to the experimental results suggesting that the unit cell volume in the nanoparticles expands upon decreasing of the size of nanoparticles [113, 114, 115, 116]. Therefore, one should be very careful, when using molecular dynamics and force-field parameters from the bulk to predict the properties of the nano-sized objects.

Thus, additional optimization of the force-field parameters is required for nanoparticles. To solve this issue, in our earlier works [31, 32] we have varied the ρ(Ni–O) and ρ(O–O) parameters of the Buckingham potential (Eq. 6.3), which determine the position of the potential minimum. However, the same result can be achieved by changing the charge of ions. One should remember that in the force-field potential model the ion charge is just another parameter to simulate the real interaction between atoms.

Therefore, we have selected the charge of nickel atoms Z_{Ni} as the optimization parameter to minimize the residual between the experimental and calculated EXAFS signals [26, 27]. Note that such choice is more appropriate in the presence of defects (nickel vacancies).

We have tested MD-EXAFS procedure for nanocrystalline NiO powder using as a model ideal NiO nanoparticles (without vacancies) with sizes starting from 3×3×3 and up to 25×25×25 unit cells. As one can see, the results presented in Fig. 6.14 suggest that the residual between the experimental and calculated EXAFS signals has a minimum for NiO nanocrystalline powder when the model nanoparticle has the size of 8×8×8 unit cells, and another minimum for NiO thin film (TF1, sputtered in pure oxygen atmosphere) when the model nanoparticle has the size of 5×5×5 unit cells. This result gives us additional confidence in our MD-EXAFS procedure, allowing us to select from a large set of possible nanoparticles a single solution which gives the best agreement with the experimental EXAFS data.

This is nontrivial result, because if we use data only from the first two coordination shells and limit our EXAFS calculations to the single-scattering approximation, then it is impossible to determine a single solution giving the required R_1 and R_2 values. Only including outer shells (up to 8th shell) and multiple-scattering paths (up to 8th order), we were able to identify the single solution giving the best overall agreement with the experimental EXAFS data and reproducing the expansion of the unit cell. However, this solution failed to accurately reproduce the contraction of the first coordination shell distance $R_1(\mathrm{Ni–O_1})$. Therefore, an improved model of the nanoparticle has been developed and will be described in the next section.

In the defect-free nanoparticles, the only source of the nearest bond Ni–O_1 shortening is a relaxation at the nanoparticle surface. The influence of such relaxation on the average Ni–O_1 distance increases upon a decrease of the nanoparticle size, because of an increase in the ratio between the number of atoms located at the surface relative to their total number. At the same time, the most significant signal from the outer shells comes from Ni–Ni pairs and chains, so including outer shells and multiple scattering effects prevents from finding as a solution unrealistically small particle (like 3×3×3 unit cells) in order to satisfy the required R_1 and R_2 values. So our MD-EXAFS method even in the case of ideal nanoparticles finds a realistic solution which very well repre-

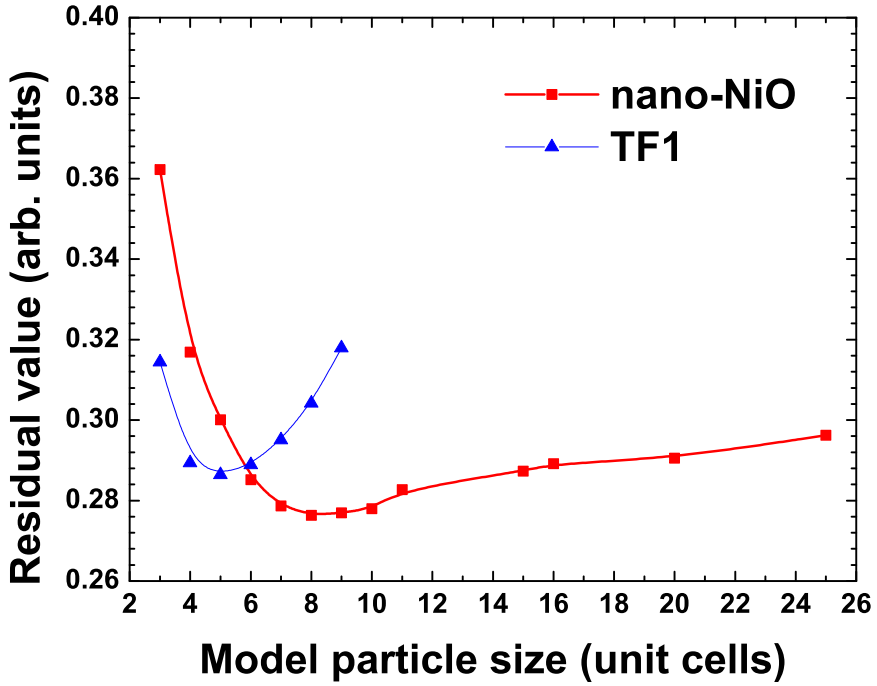

Figure 6.14: The dependence of the residual between the experimental and MD-EXAFS signals (see Sec. 4.4 for detailes of calculations) on the nanoparticle size equal to the $l \times l \times l$ unit cells. The results for the two series of simulations are shown: red squares are for NiO nanocrystalline powder (nano-NiO) and blue triangles are for NiO thin film (TF1) sputtered in pure oxygen atmosphere. In both cases, there is a clear minimum at l=8 for nano-NiO and at l=5 for TF1.

sents the structure of the real life average nanoparticle, except for the distance in the first coordination shell of nickel R_1(Ni–O_1).

6.1.2.4 Modeling of NiO nanoparticles with nickel vacancies

Stoichiometric NiO has green color, and the black color is good indicator of defects in the material. As it was shown by different experimental [88, 89, 91, 112, 113, 126, 144, 145] and *ab initio* [146, 147] studies, the most dominant defects in this material responsible for p-type conductivity are nickel vacancies. It is energetically preferable point defect in NiO compared with oxygen vacancies and oxygen interstitial [146, 147].

All our nanocrystalline NiO samples have black color, that gives strong evidence for the presence of the nickel vacancies. Therefore, they should be included into the nanoparticle model to make it more realistic [26, 27].

Nickel vacancies were generated by randomly removing Ni atoms from the ideal model particle, ensuring their homogeneous distribution [26]. Thus, each model particle now is characterized by its size L and the number of nickel vacancies N_{vac}. Taking into account that

$$N_{\mathrm{Ni}} + N_{\mathrm{vac}} = N_{\mathrm{O}}, \tag{6.4}$$

the vacancy concentration C_{vac} can be calculated as

$$C_{\mathrm{vac}} = \frac{N_{\mathrm{vac}}}{N_{\mathrm{O}}}, \tag{6.5}$$

where N_{Ni} and N_{O} are the number of nickel and oxygen atoms, respectively.

The charge of oxygen atoms Z_{O} was calculated to maintain electroneutrality of the system, taking into account the Ni vacancies when present

$$Z_{\mathrm{O}} = -Z_{\mathrm{Ni}}\frac{N_{\mathrm{Ni}}}{N_{\mathrm{O}}}. \tag{6.6}$$

Note that in our simple model all Ni ions regardless of their location have the same charge (Z_{Ni}) and so do all oxygen ions (Z_{O}).

To understand the influence of nickel vacancies on the structure of nanoparticles, we first calculated the relaxation of the local atomic structure around the single vacancy in the bulk of c-NiO (Fig. 6.15) [26]. This was done by calculating the average atomic distances for a large set of atomic configurations, generated by the MD simulation. The obtained results show that the six nearest oxygen atoms move away from the center of

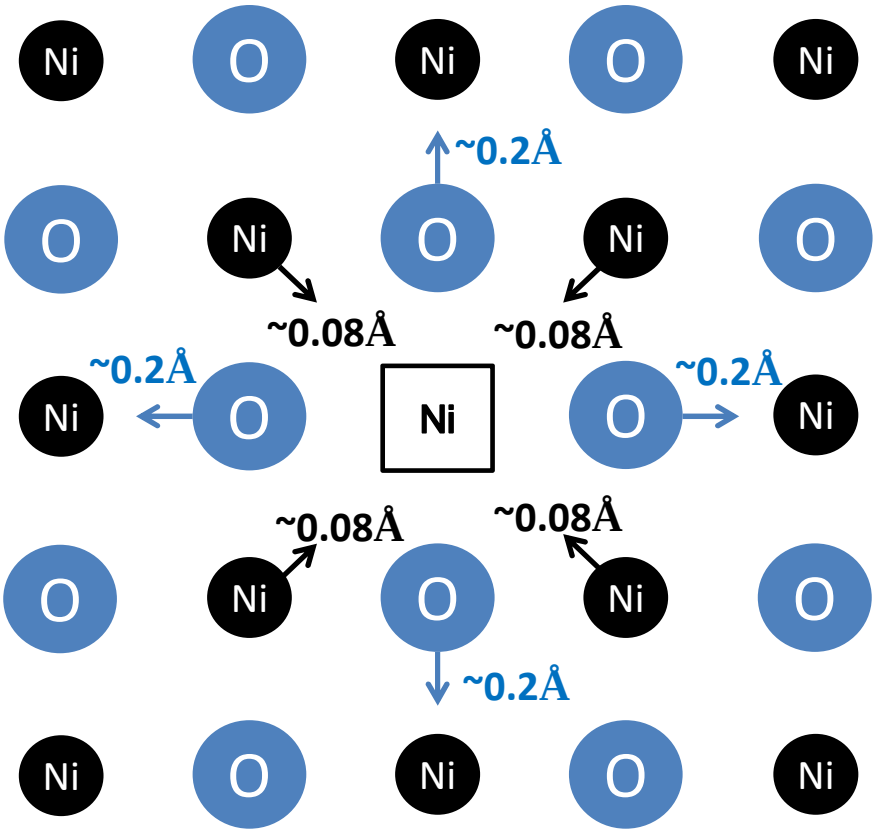

Figure 6.15: Schematic view of the nearest-neighbor relaxation around nickel vacancy in the bulk of nickel oxide according to our molecular dynamics simulations. Note that oxygen atoms move outwards, but nickel atoms move inwards to the nickel vacancy.

the vacancy by ≈0.2 Å, thus significantly decreasing the distance with the neighboring Ni atoms. At the same time, twelve nearest Ni atoms move slightly towards the center of the vacancy by ≈0.08 Å, thus increasing the distance between the nearest Ni atoms.

This relaxation is caused by short-range two-body central force interactions given by Buckingham potential and by long-range Coulomb interactions. By removing Ni atom one changes the balance of the electrostatic interactions, so it is expected that oppositely charged nickel and oxygen ions move closer, whereas ions having the same charge move apart from each other. This effect is strong in the first shell (Ni–O) and becomes much weaker in the second shell, and practically vanishes in the next shells. Such relaxation of atomic structure, induced by the presence of nickel vacancy, plays significant role in the average structure relaxation, especially for the first coordination

shell of nickel, as was found recently in [126]. The results of our simulations are in excellent agreement with those from the recent *ab initio* calculations of the structure relaxation around Ni vacancy [146, 147], which predict the relaxation of oxygen atoms by about 0.17 Å outwards from the vacancy. This fact confirms the ability of our simple force-field potential model to reproduce well structure relaxation around nickel vacancies.

The structure relaxation within the whole nanoparticle shows a very complex picture. The influence of surface extends deep inside the nanoparticle volume, and, only in the large enough nanoparticles having a size L >10 nm, one can find some inner part, which is uniform and can be treated as the "core". This result provides a support for recently proposed core-shell model of large NiO nanoparticles having a size of about 10-18 nm [130]. The structure relaxation influences several atomic layers up to few nanometers below the surface, and also the shape of the initially cubic particle becomes slightly rounded. Note that the relaxation depends also on the nickel atom position at the surface, i.e., in the corner, at the edge or at the face. Adding more vacancies makes this landscape even more complex. Therefore, we decided to model nanoparticles as a whole, because it is hard to define any equivalent regions inside the nanoparticle, especially for small nanoparticles with nickel vacancies.

We started simulations from a generation of desired NiO model nanoparticles, having a cubic shape, a given size L and a number of randomly distributed Ni vacancies with a given concentration C_{vac}. For each model nanoparticle we applied previously described MD-EXAFS procedure to obtain configuration-averaged EXAFS signal.

The results of the first step obtained for a large set of nanoparticles are presented in Fig. 6.16, which shows a value of the residual modulus $|\Delta R(\mathrm{Ni–O_1})|$ as a function of the particle size L and of the Ni vacancies concentration C_{vac}. One can see that for any size of model nanoparticle starting from $L = 3$ there exists a vacancy concentration that gives for a single Z_{Ni} value both interatomic distances $R(\mathrm{Ni–O_1})$ and $R(\mathrm{Ni–Ni_2})$ equal to those found by the conventional modeling procedure (Fig. 6.9). This result gives a proof that information from the first two coordination shells is not enough to unambiguously determine both size of and vacancy concentration in a nanoparticle. Nevertheless, this first step allows us to restrict significantly the domain of possible solutions. Therefore, it is crucial for the practical implementation, since the calculation

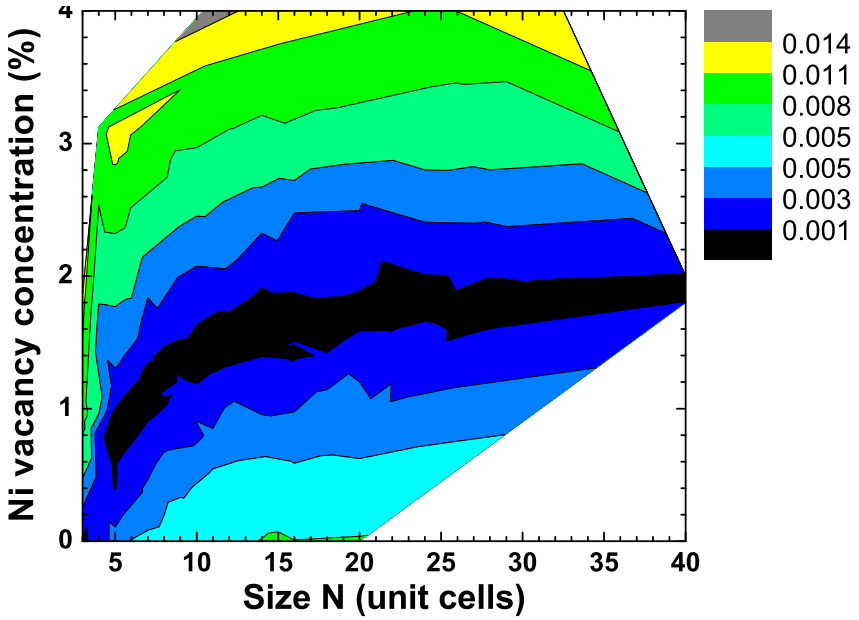

Figure 6.16: The dependence of the residual modulus value $|\Delta R(\text{Ni–O}_1)|$ between the first shell interatomic distances, obtained for cubic NiO nanoparticles by conventional analysis method (Fig. 6.9) and from the MD simulation, on the nickel vacancy concentration C_{vac} and on the nanoparticle size $L{=}Na_0$ under imposed requirement that the second shell interatomic distance $R(\text{Ni–Ni}_2)$ should coincide with the value, obtained by the conventional modeling procedure (Fig. 6.9) within ± 0.001 Å.

of the configuration-averaged EXAFS signal is very time consuming, especially in the case of nanoparticles having many non-equivalent atom sites.

At the second step we considered only those model nanoparticles, which have the average distance in the first $R(\text{Ni–O}_1)$ and second $R(\text{Ni–Ni}_2)$ coordination shells within the desired accuracy (± 0.005 Å or better in the present work) compared with the results of the conventional EXAFS analysis (Sec. 6.1.2.2). The configuration-averaged EXAFS spectrum for each nanoparticle was calculated, taking into account the multiple-scattering effects, and the sum of squares of the residuals between the experimental and model EXAFS spectra was evaluated. A small variation of the Ni ions charge Z_{Ni} by ± 0.05 was also allowed to further minimize the residual value for each model nanoparticle.

As a result, we found that there is a clear minimum in the dependence of the residual on the particle size and vacancy concentration, which determines the sought model nanoparticle. Thus, only comparison between the experimental and configuration-

Table 6.3: The size L of the NiO nanoparticles, estimated from EXAFS and XRD data. $L = la_0$ where l is the number of unit cells and a_0 is the lattice parameter. C_{vac} is the concentration of nickel vacancies. $L(N_{\mathrm{Ni2}})$ is the particle size estimated from conventional EXAFS analysis using the Ni second shell coordination numbers and assuming cubic shape of the nanoparticles (Fig. 6.10). $L(V)$ is the particle size estimated using Eq. 6.2 and the second shell radius $R_2(\mathrm{Ni-Ni_2})$. L(Scherrer) is the particle size estimated from XRD data using Scherrer method.

	nano-NiO	TF1	TF2	TF3
C_{vac} (%)	0.4	1.0	1.4	1.6
l (unit cells)	9	6	5	4
L (nm)	3.6	2.3	1.9	1.5
$L(N_{\mathrm{Ni2}})$ (nm)	5.4	2.5	2.1	1.7
$L(V)$ (nm)	7.1	4.9	4.6	4.1
L(Scherrer) (nm)	4.6-8.0	5-7	11-13	16-18

averaged EXAFS spectra, using the full potential of the multiple-scattering theory, allowed us to select the best nanoparticle model, which also fulfills conditions of the first step. The experimental and final theoretical EXAFS spectra are compared in Fig. 6.17, showing good agreement in both k and R space for NiO nanocrystalline powder and thin film samples.

The nanoparticle model, having the size $L \approx 3.6$ nm and the vacancy concentration $C_{\mathrm{vac}} = 0.4\%$, gives the best fit to the experimental EXAFS spectrum for the NiO nanocrystalline powder sample (nano-NiO). The same procedure was applied to the experimental data of NiO thin film samples.

The size of the model nanoparticles and the concentration of nickel vacancies for all thin film samples are reported in Table 6.3. As one can see, these results correlate well with those of the analysis for the first two shells by conventional EXAFS method (see Fig. 6.10), suggesting that the average size of the nanoparticles decreases in the series of our samples: nano-NiO (nanocrystalline powder), TF1 ($\mathrm{Ar/O_2} = 0/100$), TF2 ($\mathrm{Ar/O_2} = 50/50$), TF3 ($\mathrm{Ar/O_2} = 90/10$). Note that the Ni vacancy concentration increases with a decrease of the nanoparticle size.

It is also interesting to compare the difference between average size of nanoparticles obtained by XRD (using Scherrer method) and EXAFS (from coordination number N_{Ni2} and MD-EXAFS methods). The two experimental techniques show qualitatively

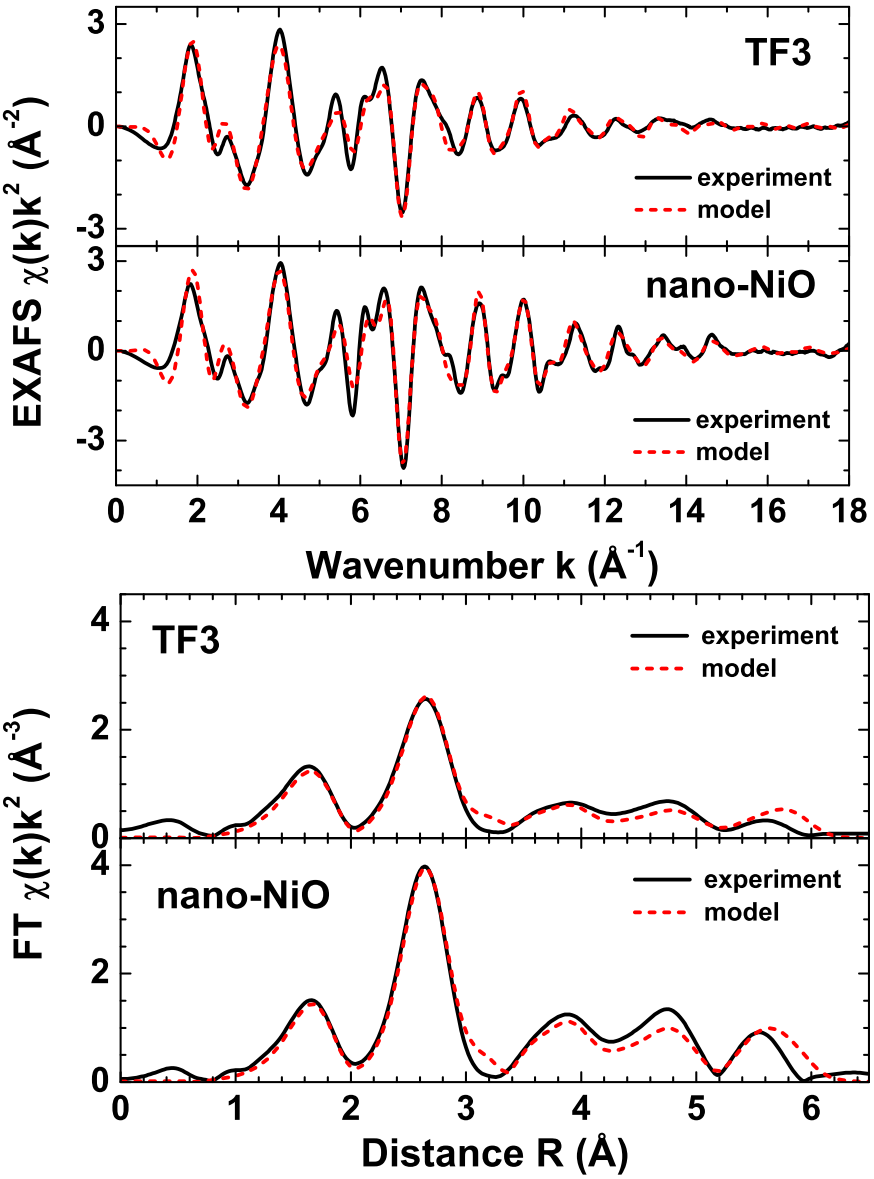

Figure 6.17: Comparison of the experimental (solid lines) and configuration-averaged (dashed lines) Ni K-edge EXAFS spectra $\chi(k)k^2$ and their Fourier transforms (FTs) for nano-NiO and TF3. The theoretical data correspond to the nanoparticle models which give the best fit to the experimental spectra (nano-NiO: N=9 corresponding to L ≈3.6 nm, C_{vac}=0.4% corresponding to 12 vacancies, Z_{Ni}=+1.976, Z_{O}=–1.968; tf-NiO: N=4 corresponding to L ≈1.5 nm, C_{vac}=1.6% corresponding to 4 vacancies, Z_{Ni}=+1.925, Z_{O}=–1.895).

similar trends, however Scherrer method gives systematically larger values for nanoparticle size: from 6 nm in the film TF3 to 17 nm in the film TF1. This fact can be explained by the presence of crystallite size distribution in the samples. The Bragg peaks in the XRD patterns are significantly broadened upon decreasing crystallite size and, thus, become masked by the noise for crystallites with a size smaller than 2 nm. Therefore, the XRD signal is dominated by the contribution coming from the largest crystallites present in the sample. On the contrary, EXAFS feels all absorbing nickel atoms, regardless the state and size of the matter, so it provides the average over the whole size distribution. For example, we can assume that in TF1 sample which is sputtered in oxygen rich atmosphere, there the large crystallites start to grow. This could create bimodal distribution of crystallites, most of them have small average size (around 2 nm), but some portion (say less than 10%) have larger average size (say about 17 nm). As they make less than 10% of overall mass of NiO, then in EXAFS spectra their influence is very limited and overall signal is dominated by the signal from the small crystallites, but the XRD pattern will be dominated only by large crystallites, leading to wrong conclusion on the average crystallite size.

Finally, we will comment on the structural parameters, obtained by a decomposition of the pair distribution functions from MD simulations into a set of Gaussian functions. Their values for the first six coordination shells of nickel, reported in Table 6.4, show clear evidence of the size reduction and structure relaxation effects. The reduction of the nanoparticle size increases the ratio of atoms at the surface relative to that in the bulk. As a result, a decrease of the average coordination numbers becomes more pronounced in outer coordination shells of all nano-sized samples, as is evidenced by the ratios CN_{na}/CN for the nanopowder and CN_{tf}/CN for the thin film. The atomic structure relaxation appears as a peculiar change of interatomic distances R and an increase of disorder, given by the MSRD σ^2. Note that contrary to the ideal nanoparticle models [31, 32], the presence of nickel vacancies in the nanoparticle models allowed us to reproduce simultaneously a decrease of the average nearest-neighbor Ni–O_1 distance and an increase of the outer shell distances. The nickel vacancies along with the nanoparticle surface relaxation contribute also into an increase of the MSRD σ^2 and small decrease of coordination numbers.

Comparing the results obtained from the MD-EXAFS modeling with those from the conventional single-scattering analysis (see Table 6.5), a good agreement is observed

Table 6.4: Structural parameters (CN is the coordination number, R is the interatomic distance, and σ^2 is the MSRD) for the first six coordination shells in c-NiO, nano-NiO and TF3, calculated by decomposition of the Ni–O and Ni–Ni pair distribution functions, obtained at 300 K, into Gaussian components.

	O_1	Ni_2	O_3	Ni_4	O_5	Ni_6
			c-NiO			
CN	6.0	12.0	8.0	6.0	24.0	24.0
R (Å)	2.093	2.961	3.627	4.188	4.682	5.129
σ^2 (Å^2)	0.0055	0.0044	0.0053	0.0058	0.0059	0.0059
			nano-NiO			
CN_{na}	5.5	10.5	6.6	5.1	19.8	18.7
R (Å)	2.091	2.968	3.638	4.190	4.685	5.142
σ^2 (Å^2)	0.0072	0.0056	0.0072	0.0093	0.0092	0.0082
			TF3			
CN_{tf}	5.1	8.6	5.1	4.1	15.4	12.9
R (Å)	2.091	2.981	3.666	4.193	4.699	5.170
σ^2 (Å^2)	0.0096	0.0083	0.0106	0.0128	0.0140	0.0121
CN_{na}/CN	0.92	0.88	0.83	0.85	0.83	0.78
CN_{tf}/CN	0.85	0.72	0.64	0.68	0.64	0.54

in the relative change of interatomic distances for the first two coordination shells of nano-NiO and TF3 compared to c-NiO. Note that their absolute values cannot be accurately compared directly, because in our conventional analysis we used experimental amplitude and phase shift functions, which were extracted from the low temperature Ni K-edge EXAFS spectrum of c-NiO assuming the crystallographic value of the lattice parameter a_0=4.176 Å. The same applies to the MSRDs, those absolute values extracted using the conventional data analysis are influenced by a correlation between the MSRD and coordination number parameters. In addition, the sample quality and the EXAFS amplitude reduction factor (S_0^2) will influence the absolute values as well [20, 22]. Nevertheless, the results of the MD-EXAFS and conventional analysis for both relative coordination numbers and relative MSRDs are in agreement and show similar trends (Table 6.5). The observed differences are attributed mainly to the sim-

Table 6.5: Relative to c-NiO values of the structural parameters (CN is the coordination number, R ($\pm$0.002 Å) is the interatomic distance, and σ^2 ($\pm$0.0003 Å^2) is the MSRD) for the first two coordination shells in nano-NiO and TF3, obtained from the best-fit of the EXAFS signals within the Gaussian approximation (Figs. 6.8 and 6.9) and from the MD-EXAFS analysis (Table 6.4).

	nano-NiO		TF3	
	Gaussian	MD-EXAFS	Gaussian	MD-EXAFS
		Ni-O_1		
CN/CN_c	1.0	0.92	1.0	0.85
ΔR (Å)	-0.006	-0.002	-0.004	-0.002
$\Delta\sigma^2$ (Å^2)	0.0032	0.0017	0.0061	0.0041
		Ni–Ni_2		
CN/CN_c	0.92	0.88	0.79	0.72
ΔR (Å)	0.009	0.007	0.017	0.020
$\Delta\sigma^2$ (Å^2)	0.0035	0.0012	0.0068	0.0039

plicity of our MD model and to inaccuracies of the theoretical amplitude and phase shift functions.

6.1.3 Conclusions

Based on the results of the EXAFS analysis for NiO samples we can withdraw several conclusions.

1. The atomic structure in nanocrystalline NiO experiences strong relaxation and lattice expansion upon a decrease of the nanoparticle size indicated by dependency of the distance of the second coordination shell of nickel atoms (R_2(Ni–Ni_2)) from the particle size.

2. At the same time, we observed controversial behavior of the distance in the first coordination shell of nickel atoms (R_1(Ni–O_2)), which becomes smaller upon a decrease of the particle size.

3. The contribution of thermal disorder to the mean-square relative displacements (MSRD) in the first and second coordination shells of nickel in the nanopowder

and thin films are close to that in the bulk nickel oxide, that suggests a similarity of their lattice dynamics.

4. Upon a decrease of the particle size the contribution of static disorder to the MSRD increases due to structure relaxation, caused by the lattice expansion and the presence of nickel vacancies.

5. Average coordination numbers in the second coordination shell of nickel atoms also decrease upon reduction of the size of the nanoparticles.

6. A method, combining classical molecular dynamics with *ab initio* multiple-scattering EXAFS calculations (MD-EXAFS method), has been extended to the case of nanoparticles. It allows us to account for the effect of the nanoparticle size, atomic structure relaxation, thermal disorder and the presence of defects using rather simple force-field model, based on the pair potentials and having a few parameters. This model allows us to take into account all coordination shells of the absorbing atom and multiple scattering effects in the EXAFS spectra.

7. The average Ni–O_1 bond length in the first coordination shell of nickel atoms contracts due to structure relaxation at the surface (especially, at corners and edges of the particles) and around the nickel vacancies. MD-EXAFS analysis showed that Ni vacancies play significant role in this structure relaxation. This phenomenon cannot be revealed by XRD, and shows the particular value of the X-ray absorption spectroscopy.

6.2 Microcrystalline and nanosized $MeWO_4$

Tungstates ($MeWO_4$, Me is a divalent metal as Mg, Ca, Sr, Ba, Co, Mn, Fe, Ni, Cu, Zn, Cd and Pb) are extremely interesting materials for many practical applications, such as scintillators [148, 149], catalysts [150, 151], gas sensors [152, 153], solid state Raman lasers [154, 155], self activating phosphors [156], electrochromic devices [100, 157], and phase change optical memories [158].

Majority of tungstates have either wolframite or scheelite structure [159]. Ions Me^{2+} having small radius (<0.77 Å) lead mainly to wolframite-type structure, but those having large radius (>0.99 Å) – to scheelite-type structure [159]. In this work we

will discuss four tungstates $CoWO_4$, $NiWO_4$, $CuWO_4$ and $ZnWO_4$, with a particular attention devoted to $CoWO_4$ and $CuWO_4$.

Crystalline $CoWO_4$, $NiWO_4$ and $ZnWO_4$ have monoclinic ($P2/c$) wolframite-type structure built from distorted WO_6 and MeO_6 octahedra joined by edges into infinite zigzag chains, consisting of octahedral units of the same type and running parallel to c-axis [159, 160] (see Fig. 6.18). The WO_6 octahedra distortion caused by second-order Jahn-Teller (SOJT) effect [161] results in the splitting of the W–O distances into three groups: two short (∼1.8 Å), two middle (∼1.9 Å) and two long (∼2.1 Å). As a result, the MeO_6 octahedra become also distorted.

Crystalline $CuWO_4$ has close structure but lower triclinic ($P\bar{1}$) symmetry due to the strong first-order Jahn-Teller (FOJT) distortion induced by Cu^{2+} $3d^9$ electronic configuration [162, 163, 164, 165]. In this structure copper atoms are bound to four oxygen atoms located in a square-like configuration at average distance 1.98 Å and to other two oxygen atoms located at about 2.4 Å above and below the CuO_4 square. Strong axial distortion of the CuO_6 octahedra results in more stronger distortion of the WO_6 octahedra [166].

So the two tungstates, $CoWO_4$ and $CuWO_4$, which we will consider in details, have two distinct structure types: in $CoWO_4$ the distortion of CoO_6 octahedra is imposed by SOJT effect in WO_6 octahedra, whereas in $CuWO_4$ much stronger distortion of CuO_6 octahedra due to FOJT effect dominates and imposes additional structural changes of WO_6 octahedra.

X-ray absorption spectroscopy has been used to study $MeWO_4$ for a while [163, 167, 168, 169, 170].

$NiWO_4$ microcrystalline samples, amorphous powders and thin films were studied in [169, 171] using W L_1- and L_3-edge and Ni K-edge X-ray absorption spectroscopy, X-ray diffraction, atomic force microscope and Raman spectroscopy. The coordination of tungsten atoms was described as WO_6 octahedra with four short and two long W–O bonds, and NiO_6 octahedra was described as built up of four strongly bonded forming square-like plane oxygen atoms and two weekly bonded oxygen atoms above and below the plane [171]. The main conclusion was that there is strong difference in the Ni–O and W–O interactions for thin film/amorphous powder and microcrystalline powder. The Ni–O bonds are stronger in the bulk material and become weaker upon decreasing the particle size, but a behaviour of the W–O bonds is opposite: upon decreasing the size

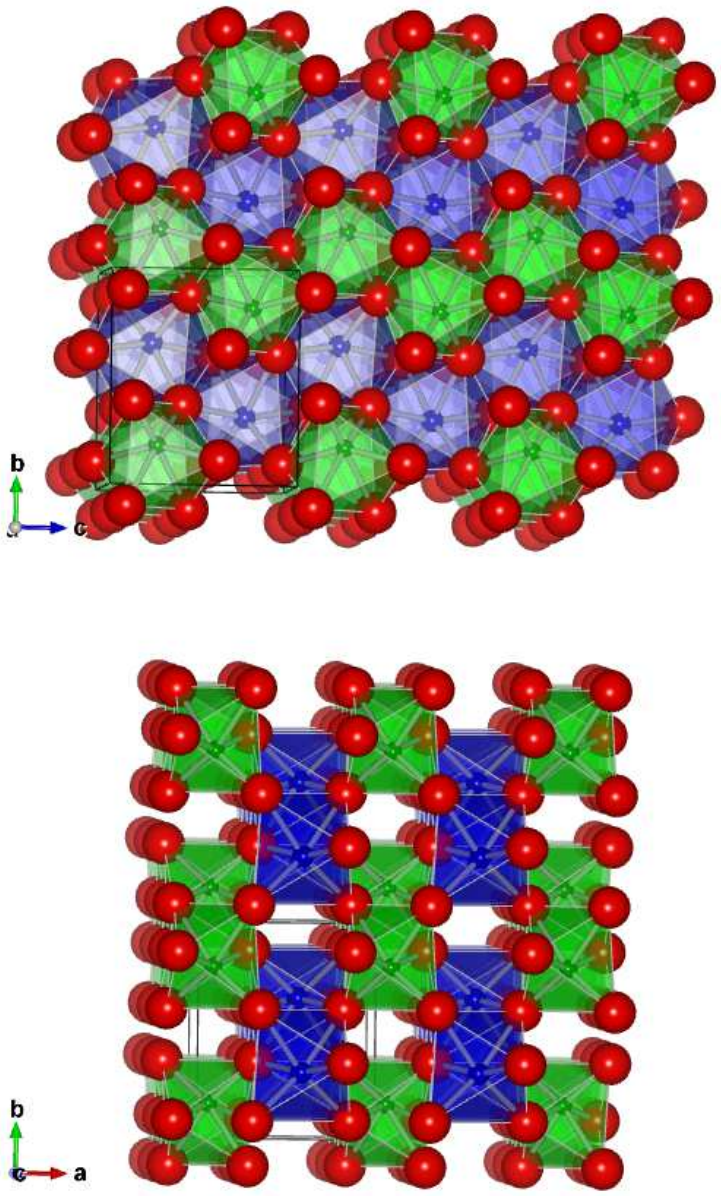

Figure 6.18: Crystal structure of $CoWO_4$. Red balls represent oxygen atoms, green balls - tungsten atoms, and blue balls - cobalt atoms. Co and W atoms are surrounded by six oxygen atoms, forming distorted octahedral coordination. Metal–oxygen octahedra of one type share edges and form zig-zag chains along the *c*-axis. Metal–oxygen octahedra of different type share single oxygen atom.

of the particles the W–O bonds become stronger and a distortion of WO_6 octahedra increases making tungsten coordination closer to the tetrahedral environment.

In [169] $ZnWO_4$, $NiWO_4$, and $CaWO_4$ were studied using W L_1- and L_3-edge EXAFS and XANES. The XANES data analysis revealed that WO_6 octahedra in $NiWO_4$ have stronger distortion than in pure WO_3. EXAFS data analysis was performed by RDF reconstruction method. The obtained shape of the RDF for the first coordination shell of tungsten atoms suggested strong distortion of WO_6 octahedra in these tungstates. The main conclusions coming from EXAFS data analysis are that in $ZnWO_4$ and $NiWO_4$, having wolframite-type structure, WO_6 octahedra are distorted with four short (1.84 Å) and two long (2.13 Å) W–O distances, but W atom in $CaWO_4$, which has scheelite-type structure, has regular tetrahedral coordination with W–O distances about 1.79 Å.

Recent studies of $ZnWO_4$ were performed using X-ray absorption spectroscopy, Raman and photoluminescence spectroscopy, and *ab initio* quantum chemistry calculations in [94, 172, 173, 174]. A strong variation of the Raman scattering band at 900-950 cm^{-1}, corresponding to the stretching W–O frequency, was observed in zinc tungstate powders upon particle size reduction [172]. It was found that the photoluminescence band at 2.5 eV, attributed to electronic transitions of the charge transfer type between oxygen and tungstate states in the WO_6 groups, shifts to longer wavelengths, comparing to single crystal, in powders upon annealing at temperatures below 450°C, whereas the band position for $ZnWO_4$ powders annealed at higher temperatures is identical to that in single crystal [172]. *Ab initio* calculations revealed that W–O chemical bonding is significantly covalent due to the electron density transfer to oxygen atoms, whereas zinc atoms show more ionic behavior, and the main contribution to the valence band is largely due to O 2p states, whereas the bottom of conduction band is dominated by W 5d states [173]. X-ray absorption spectroscopy studies of $ZnWO_4$ microcrystalline and nanocrystalline powders using Zn K-edge and W L_3-edge revealed that EXAFS signals for nanoparticles show weak temperature dependence and do not contain high-frequency contributions indicating the absence of long-range order [94]. RDF reconstruction unveiled three groups of W–O bonds (2×1.79 Å, 2×1.91 Å, and 2×2.13 Å) and three groups of Zn–O bonds (2×2.03 Å, 2×2.09 Å, and 2×2.23 Å) for microcrystalline $ZnWO_4$, whereas in nanoparticles RDF is broadened, only the first

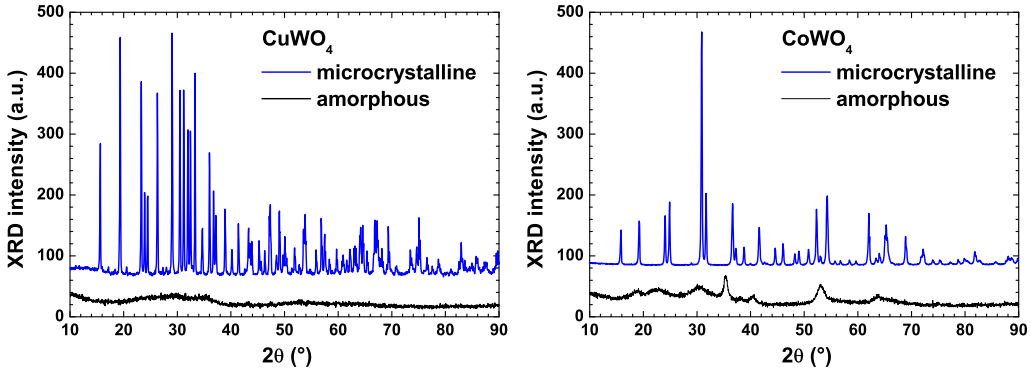

Figure 6.19: X-ray diffraction (XRD) patterns of microcrystaline and nanoscale $CuWO_4$ and $CoWO_4$.

coordination shell is well defined but slightly shifted to the shorter distances, indicating that both tungsten and zinc make stronger bonds with the nearest oxygen atoms while remaining oxygen atoms become weakly bound [94]. The RDFs for nanoparticles of $ZnWO_4$ show minor changes with temperature, which is a clear sign that the static disorder is masking the thermal one [94].

In this study we have explored a size-induced relaxation of the local structure in $CoWO_4$ and $CuWO_4$ by extended x-ray absorption fine structure (EXAFS) spectroscopy, x-ray powder diffraction and micro-Raman spectroscopy, extending recent results of our laboratory for nanosized $NiWO_4$ [171] and $ZnWO_4$ [94, 172, 174], thus, allowing us to elucidate in more details the effect of size, temperature and transition metal type.

6.2.1 X-ray diffraction

The X-ray diffraction (XRD) patterns of $CuWO_4$ and $CoWO_4$ are shown in Fig. 6.19. The XRD patterns for as-prepared tungstates have strongly broadened Bragg peaks, thus indicating their nanocrystalline structure. The powders become microcrystalline upon annealing in air at 800°C [172], transforming into respective wolframite-type phase with monoclinic ($CoWO_4$ [175], $NiWO_4$ [176], $ZnWO_4$ [177, 178]) or triclinic ($CuWO_4$ [179]) symmetry.

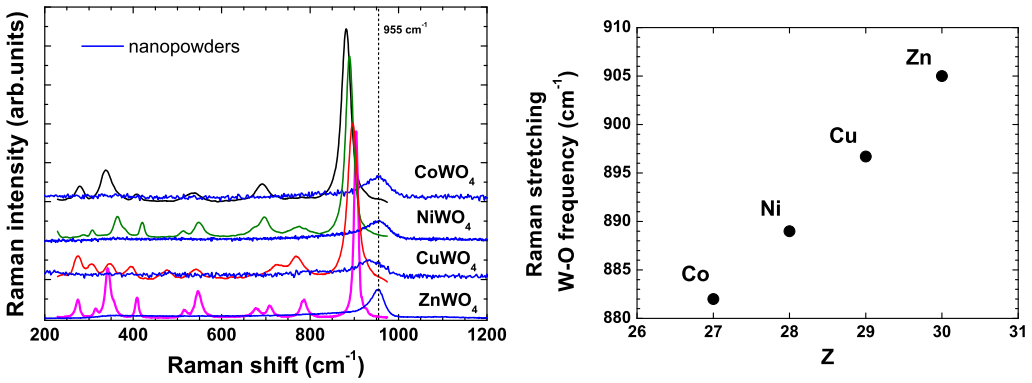

Figure 6.20: Left panel: Raman scattering spectra of microcrystaline and nanocrystaline $MeWO_4$ (Me = Co, Ni, Cu, Zn) powders. The position of the main band at 955 cm^{-1} in nanosized tungstates is indicated by dashed vertical line. Measurements were performed at 20°C. Right panel: the dependence of the main Raman band for microcrystaline $MeWO_4$ from the type of the Me atom.

6.2.2 Raman scattering spectroscopy

The Raman scattering spectra of microcrystaline tungstates are shown in Fig. 6.20. Since they have two formula units per primitive cell, the group theory analysis predicts 36 lattice modes, of which 18 even vibrations are Raman active [162, 180, 181, 182]. Only 12 of them can be observed in the frequency range reported in Fig. 6.20. The position of the most intense band, located at 882-905 cm^{-1} and corresponding to the symmetric A_g vibration of the short W–O bond, shifts systematically to higher frequencies upon transition from $CoWO_4$ to $ZnWO_4$ (see Fig. 6.20).

The Raman scattering spectra of nanoparticles differ significantly from that in microcrystalline powders. They are dominated by one broad band, located at ∼955 cm^{-1} (see Fig. 6.20). Higher Raman frequency of the A_g vibration of the short W–O bond is an indication of the stronger W–O bonding [183].

One should note that a care should be taken when measuring the Raman scattering from tungstate nanoparticles, since they can be easily crystallized under excessive laser irradiation.

6.2.3 X-ray absorption spectroscopy

Experimental W L_3-edge and Co(Cu) K-edge EXAFS spectra $\chi(k)k^2$ and their Fourier transforms (FTs) measured at $T = 300$ K for $CoWO_4$ and $CuWO_4$ are shown in Fig. 6.21.

The amplitude of all peaks in FTs, especially beyond the first one, is strongly reduced in nanopowders, as expected. The effect is more pronounced at the W L_3-edge, indicating stronger relaxation of tungsten environment. There is no local order beyond 7 Å in $MeWO_4$ nanoparticles.

A comparison of the W L_3-edge and Cu K-edge EXAFS spectra (Fig. 6.22) obtained at 10 K and 300 K in $CuWO_4$ suggests that the effect of thermal disorder is relatively small, especially in the first coordination shell.

In this study we have analysed only the first coordination shell, which contains only single-scattering contributions, singled out by the back-FT procedure in the range of $\simeq$0.8-2.2 Å.

To extract structural information, the first shell EXAFS contributions $\chi(k)k^2$ were best-fitted using a model-independent approach [60, 61] allowing the reconstruction of the true radial distribution function (RDF) $G(R)$ (see Sections 3.4 and 4.2), in this case corresponding to the distribution of oxygen atoms within metal–oxygen octahedra.

The scattering amplitude $F_i(k, R_i)$ and phase shift $\phi_i(k, R_i)$ functions for metal–oxygen atom pairs were calculated by *ab initio* multiple-scattering code FEFF8 [50] using the complex exchange-correlation Hedin-Lundqvist potential. The calculations were performed based on the crystallographic structure of tungstates ($CoWO_4$ [175], $NiWO_4$ [176], $CuWO_4$ [179] and $ZnWO_4$ [177, 178]), considering a cluster of 8 Å size around the absorbing metal atom. Calculations of the cluster potentials were done in the muffin-tin (MT) self-consistent-field approximation using default values of MT radii as provided within the FEFF8 code [50]. The obtained RDFs are shown in Fig. 6.23.

A comparison of the reconstructed RDFs (Fig. 6.23) obtained at 10 K and 300 K in $CuWO_4$ suggests that the effect of thermal disorder leads to some peak broadening and is relatively small, in particular, in nanopowders where static relaxation dominates.

Both RDFs $G_{W-O}(R)$ and $G_{Me-O}(R)$ (Me = Co, Ni, Cu, Zn) for microcrystalline tungstates agree well with their crystallographic structure.

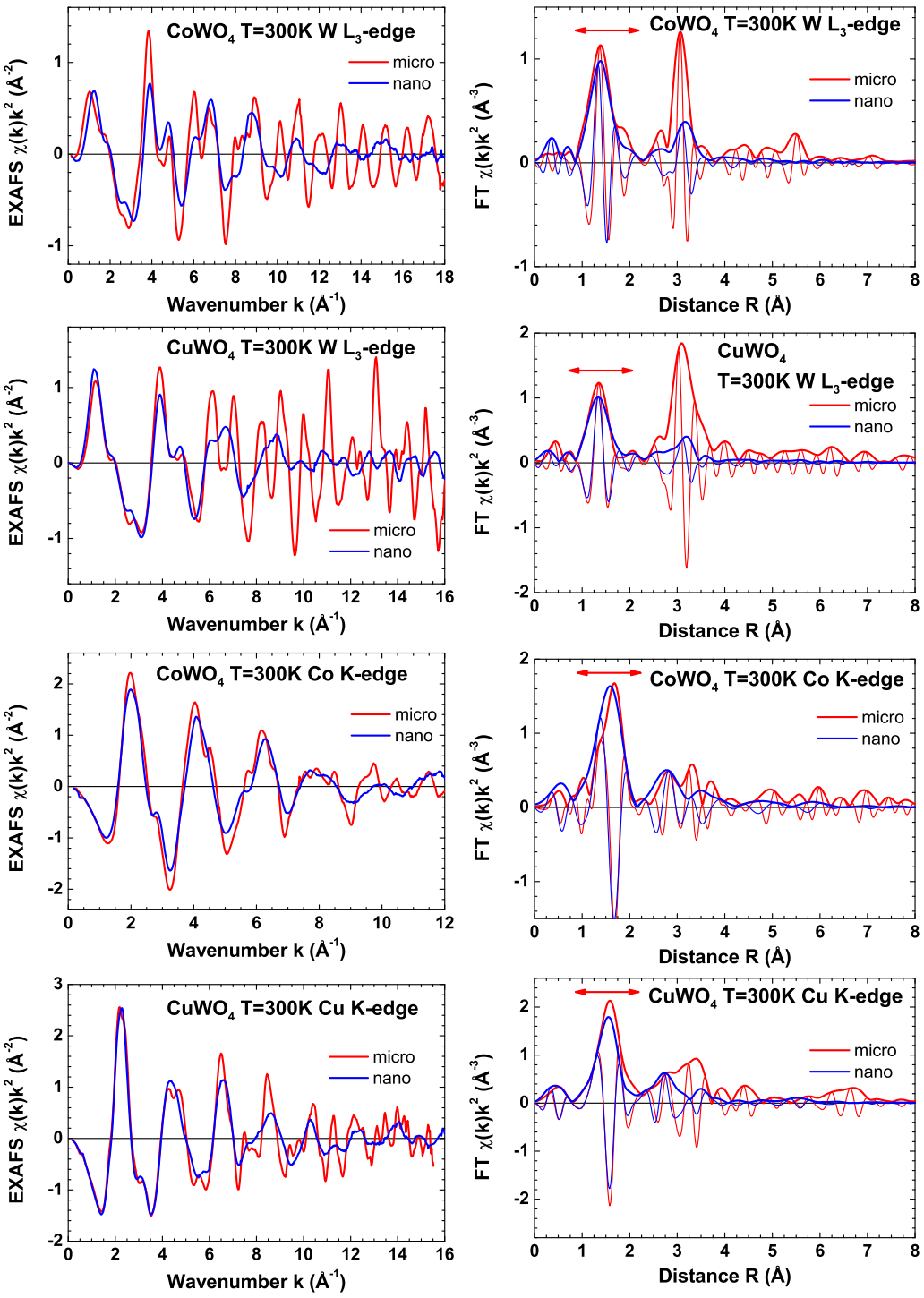

Figure 6.21: The experimental W L_3 and Co(Cu) K edge EXAFS spectra $\chi(k)k^2$ and their Fourier transforms for microcrystalline and nanocrystaline $CoWO_4$ and $CuWO_4$ at $T = 300$ K. Both modulus and imaginary parts of FTs are shown. Note that the positions of the FT peaks in Fig. 6.21 are shifted from their true crystallographic values because the FTs were calculated without phase-shift corrections.

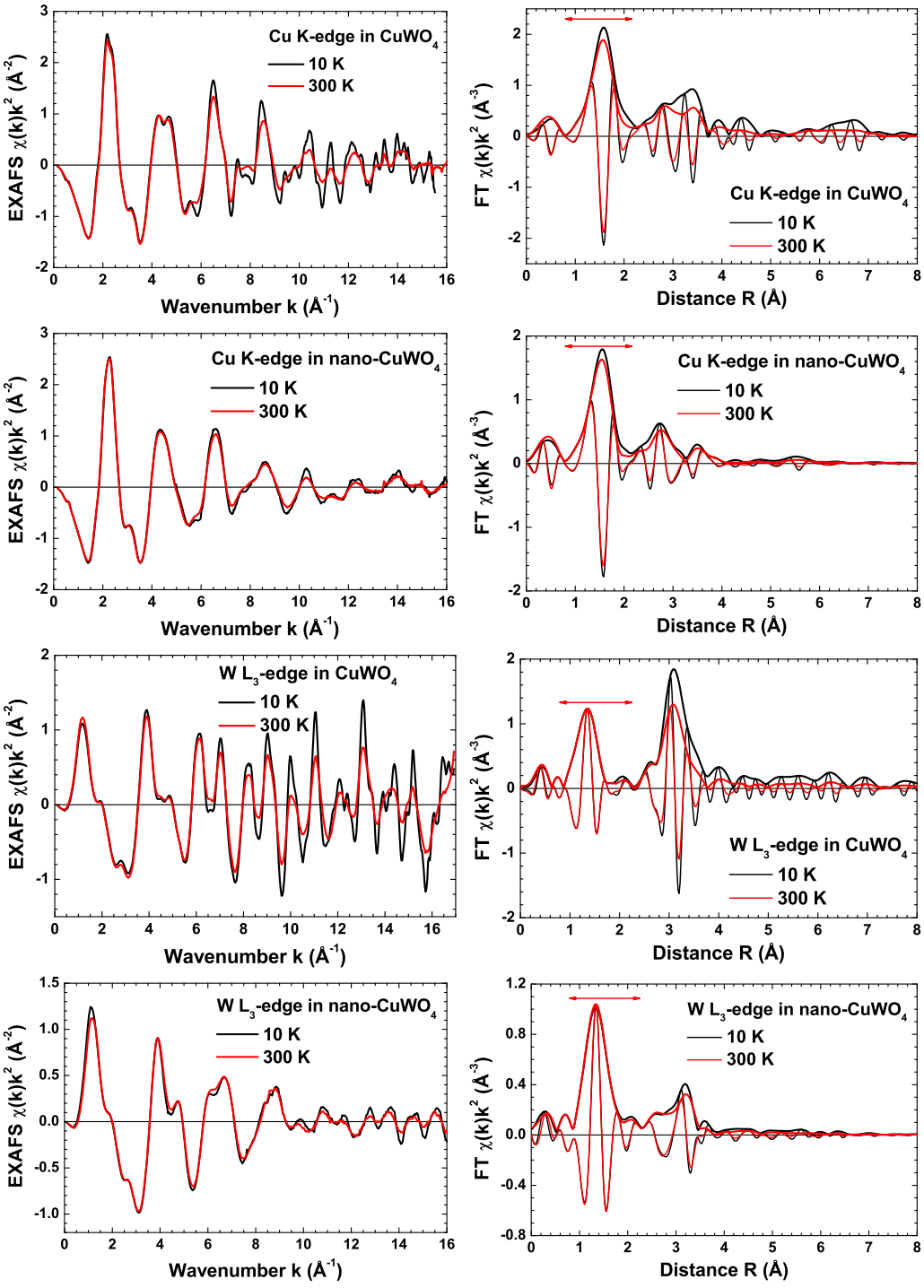

Figure 6.22: The experimental W L_3 and Co(Cu) K edge EXAFS spectra $\chi(k)k^2$ and their Fourier transforms for microcrystalline and nanocrystaline $CuWO_4$ at $T = 10$ K and 300 K. The range of the first coordination shell is indicated by arrows in FTs.

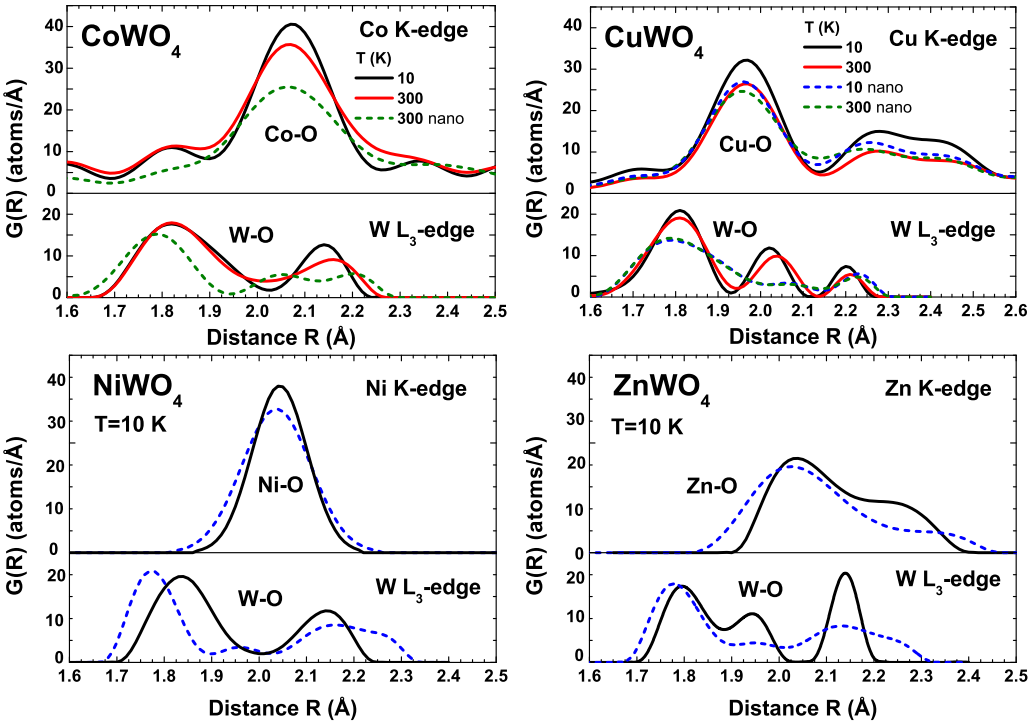

Figure 6.23: The reconstructed RDFs $G(R)$ for the first coordination shell of tungsten and transition metals in microcrystalline (solid lines) and nanocrystaline (dashed lines) $MeWO_4$ (Me = Co, Ni, Cu, Zn). The data for $NiWO_4$ and $ZnWO_4$ are taken from [94, 184].

In $CoWO_4$ and $NiWO_4$ the six oxygen atoms of MeO_6 octahedra contribute into one broad peak, centered at ∼2.08 Å in the RDF $G_{Co-O}(R)$ and at ∼2.05 Å in the RDF $G_{Ni-O}(R)$, but the six oxygens of the WO_6 octahedra are divided into two groups of four (at ∼1.83 Å) and two (at ∼2.15 Å) atoms [175, 176].

In microcrystalline $CuWO_4$ [179] the RDF $G_{Cu-O}(R)$ of CuO_6 octahedra is split into two peaks, composed of four and two oxygen atoms. At the same time, the distortion of WO_6 octahedra is the strongest one among all four tungstates: six oxygen atoms are divided into 3 groups of three (at ∼1.81 Å), two (at ∼2.02 Å) and one (at ∼2.20 Å) atoms.

The distortion of metal–oxygen octahedra in microcrystalline $ZnWO_4$ [177, 178] is stronger than in $CoWO_4$ and $NiWO_4$, but weaker than in $CuWO_4$. The oxygen atoms in both ZnO_6 and WO_6 octahedra are divided into three groups of two oxygen atoms

each. The group of nearest four oxygens is responsible for a single peak at ∼2.02 Å in the RDF $G_{Zn-O}(R)$, whereas remaining two oxygens give rise to the peak at ∼2.25 Å. In the case of the RDF $G_{W-O}(R)$, the three groups of oxygen atoms are well resolved and contribute into the three peaks at ∼1.80 Å, ∼1.95 Å and ∼2.14 Å, respectively.

In nanocrystaline tungstates, the RDFs $G_{Me-O}(R)$ are more broadened. Besides, the distortion of ZnO_6 octahedra becomes stronger in nano-$ZnWO_4$, leading to further separation of nearest four and distant two oxygen atoms. The modification of the RDFs $G_{W-O}(R)$ is more dramatic. The distortion of WO_6 octahedra increases in all tungstates in such a way that the nearest four oxygen atoms move slightly closer, whereas the distant two oxygens move away. This effect is most evident in the RDFs $G_{W-O}(R)$ for nanosized $NiWO_4$, $CoWO_4$ and $ZnWO_4$.

6.2.4 Discussion

The strongly broadened Bragg peaks in XRD patterns (Fig. 6.19) of as-prepared tungstates support their nanocrystalline structure. Taking into account nanoparticles stoichiometry, the size of metal–oxygen octahedra (∼4 Å) and their connectivity in crystalline tungstates, one can conclude that nanoparticles are built up of just a few tens of metal–oxygen octahedra.

Chemical bonding in microcrystalline tungstates can be successfully probed by Raman spectroscopy, providing an access to the half of vibrational modes (Fig. 6.20). An increase of the stretching W–O frequency from 882 cm^{-1} in $CoWO_4$ to 905 cm^{-1} in $ZnWO_4$ indicates some strengthening of tungsten–oxygen bonds [183], which compete with the Me–O bonding. Note that the corresponding W–O bond lengths are almost the same (∼1.79 Å) in the four tungstates [175, 176, 177, 178, 179].

Nanocrystalline tungstates are much weaker Raman scatterers (Fig. 6.20): the only visible broad band at ∼955 cm^{-1} was attributed previously to the double tungsten-oxygen W=O bonds at the nanoparticle surface [172]. The band has a single-peak shape in $CoWO_4$, $NiWO_4$ and $ZnWO_4$, but has more complex structure in $CuWO_4$, suggesting the presence of slightly inequivalent non-bridging W=O bonds. A well known correlation [183] between the force constant (or stretching frequency) and the length of the W–O bond suggests the W=O bond length of about 1.7 Å.

In fact, the existence of short tungsten–oxygen bonds in nanopowders is clearly visible in the RDFs $G_{W-O}(R)$ (Fig. 6.23). In general, the WO_6 octahedra distortion

originates from strong electron–lattice coupling, which leads to the second-order Jahn–Teller (SOJT) effect due to a covalent interaction of empty $5d$ orbitals in W^{6+} ions with filled $2p$ orbitals in the oxygen atoms [185]. An additional contribution into the WO_6 octahedron deformation comes from competing interaction of oxygens with the $3d$ orbitals in transition metal ions. It manifests most strongly in $CuWO_4$, where the axial distortion of CuO_6 octahedra is stabilized by the first-order Jahn–Teller (FOJT) effect caused by the $3d^9$ electron configuration of Cu^{2+} ions [162, 163, 164, 165]. As a result, the RDFs $G_{Cu-O}(R)$ have close shape in both microcrystalline and nanocrystalline powders, and the difference between the RDFs $G_{W-O}(R)$ is caused mainly by peak broadening.

In $CoWO_4$, $NiWO_4$ and $ZnWO_4$, the bonding between Me $3d$ and oxygen ions is less rigid, so that their local environment is able to relax in nanopowders, giving more freedom to tungsten ions to adapt themselves. Therefore, tungsten ions are able to attract four nearest oxygens, thus enhancing the distortion of WO_6 octahedra.

6.2.5 Conclusions

Summarizing the results of the Raman spectroscopy and EXAFS analysis for $MeWO_4$ samples, we can withdraw the following conclusions.

1. Temperature effect on the atomic structure dynamics is well pronounced for microcrystalline $MeWO_4$, but is masked in nanocrystalline samples by static disorder.

2. The analysis of the W L_3-edge and Me (Me = Co, Ni, Cu, Zn) K-edge EXAFS spectra by the regularization-like method (RDF reconstruction) has allowed us to reliably determine a distortion of WO_6 and MeO_6 octahedra in microscrystalline and nanosized tungstates.

3. The distortion of metal–oxygen octahedra is caused by the electron–lattice coupling, which depends on the electronic structure of Me^{2+} and W^{6+} ions.

4. Structure relaxation upon particles size reduction is the largest in WO_6 octahedra.

5. The surface of the nanoparticles is probable place for a formation of the double tungsten–oxygen bonds, being responsible for the broad band at ~955 cm^{-1} in Raman scattering spectra.

The obtained information on the structure relaxation in nanosized tungstates is relevant for understanding and tuning of their functional properties [94, 186, 187].

6.3 Microcrystalline and nanosized PbS

6.3.1 X-ray absorption spectroscopy

Lead sulfide (PbS) is an IV-VI semiconductor, having cubic sodium chloride type structure (space group $Fm\bar{3}m$, lattice constant $a_0 = 5.936$ Å [188]) and rather small bandgap ($E_g = 0.42$ eV at $T = 300$ K [189]), which is very suitable for infrared detection applications. Optical properties of PbS nanocrystals strongly depend on their size and shape, and the quantum confinement effect leads to an increase of effective band gap E_g to values beyond 1 eV. Therefore, nanosized PbS is a promising material for harvesting visible and infrared radiation and other opto-electronic applications [190].

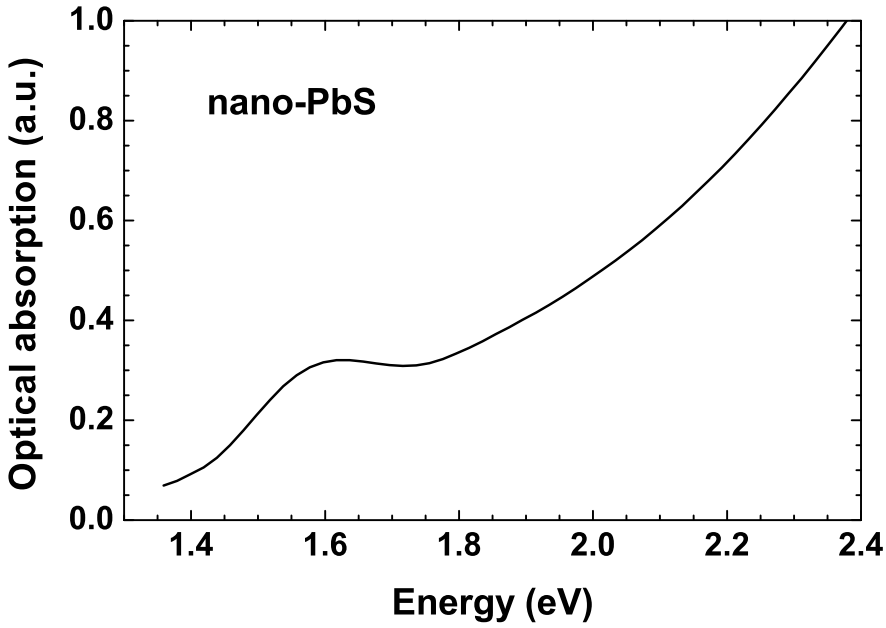

Figure 6.24: Optical absorption spectrum of nano-PbS. The energy of the first exciton peak is about 1.63 eV.

To our knowledge, there is limited number of X-ray absorption spectroscopy (XAS) studies of local structure in crystalline PbS [191, 192, 193] and no such studies for nanosized PbS. Therefore, we have performed the Pb L_3-edge XAS study of local environment both in microcrystalline and nanocrystalline PbS with the goal to estimate

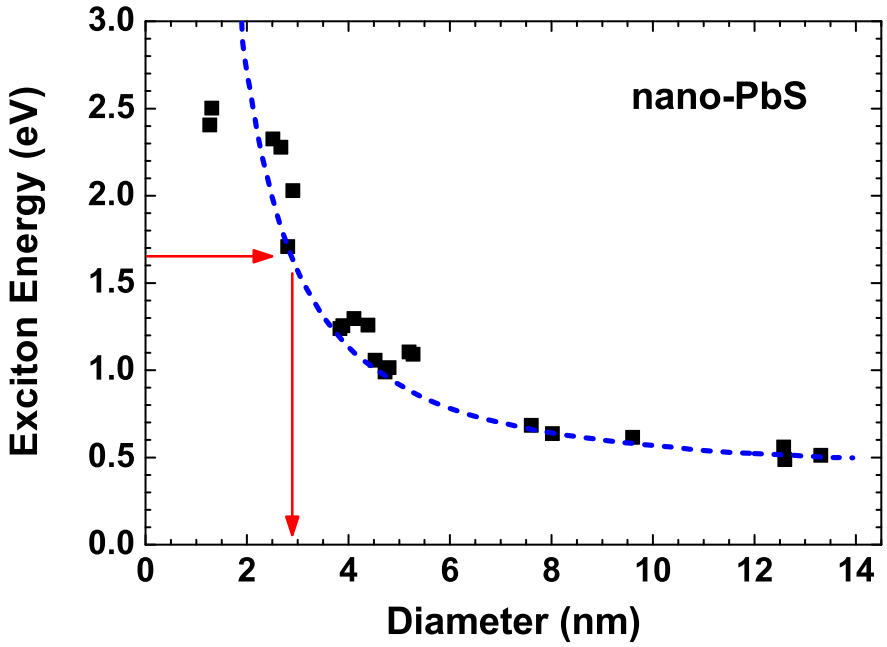

Figure 6.25: Size dependence of the exciton energy on the diameter of nanosized PbS according to [195]. Arrows indicate the position of the exciton peak and the corresponding size for our nano-PbS sample.

the relaxation of the local atomic structure around lead atoms due to a reduction of particles size.

Optical absorption spectra (Fig. 6.24) of our nanocrystalline PbS show well defined excitonic peak centered at about 1.63 eV (760 nm). There are well known relations linking particle size with optical band gap E_g [194] and position of the excitonic peak [195]. Using this relationship shown in Fig. 6.25 we estimated the average size of nanoparticles in nano-PbS to be about 3 nm.

The extended X-ray absorption fine structures (EXAFS) at the Pb L_3-edge were extracted and analyzed using the standard procedure described in [28] and the "EDA" software package [56]. The experimental Pb L_3-edge EXAFS spectra and their Fourier transforms for c-PbS and nano-PbS at $T = 300$ K are shown in Fig. 6.26. As one can see, there is strong structure relaxation in nanosized PbS, observed as a small phase shift of the EXAFS signal and a change in the peak positions and amplitudes in FT.

The phase shift of the EXAFS signal is well noticeable at $k > 5$ Å^{-1} and indicates changes in interatomic distances of nano-PbS compared with c-PbS. In the Fourier

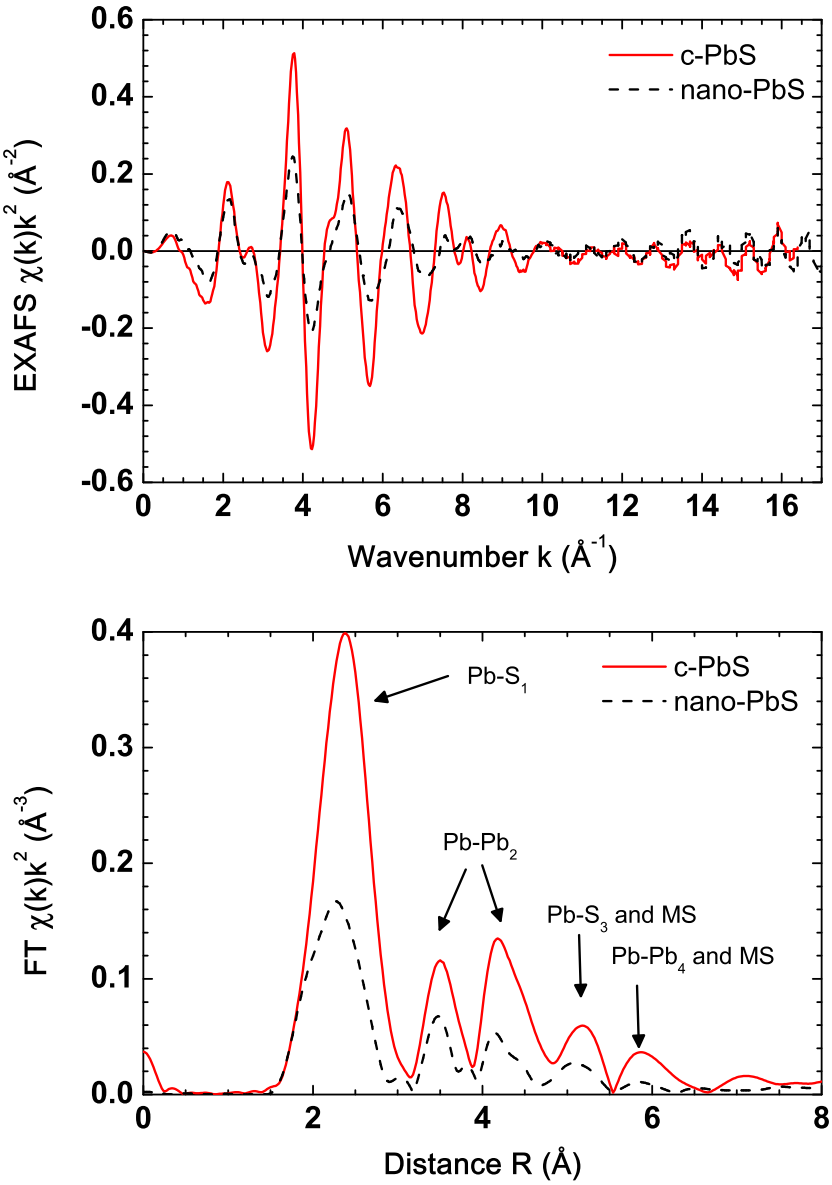

Figure 6.26: The experimental Pb L_3-edge EXAFS spectra $\chi(k)k^2$ and their Fourier transforms (FTs) for c-PbS and nano-PbS at $T = 300$ K.

Table 6.6: Structural parameters (N is the coordination number (± 0.5), R is the interatomic distance (± 0.01 Å), and σ^2 is the mean-square relative displacement (MSRD) (± 0.001 Å^2)) for the first two coordination shells in c-PbS and nano-PbS at $T = 300$ K, calculated by decomposition of the Pb–S and Pb–Pb pair distribution functions into Gaussian components.

	S_1	Pb_2	S_1	Pb_2
	c-PbS		nano-PbS	
N	6.0	12.0	3.2	7.9
R (Å)	2.95	4.22	2.93	4.23
σ^2 (Å^2)	0.017	0.020	0.021	0.028

transforms of the EXAFS spectra we can clearly recognize several peaks. The first peak in FT at 2.4 Å is the most pronounced and is due to the single-scattering signal from sulphur atoms in the first coordination shell of lead atoms (Pb–S_1). The signal from the second coordination shell (Pb–Pb_2) is split into two peaks with the maxima at 3.5 Å and 4.2 Å. Further peaks in the Fourier transforms have very strong influence of the multiple-scattering (MS) signals, which are mixed with the next coordination shells of lead atoms (Pb–S_3 and Pb–Pb_4). Therefore, the analysis of the first two coordination shells of Pb can be performed within the single-scattering approximation.

In the standard analysis [28], the contribution to the total EXAFS signal from the first two coordination shells (Pb–S_1 and Pb–Pb_2) was first isolated by the Fourier filtering procedure in the R-space range of 1.53–4.90 Å. Next, the two-component Gaussian model within the single-scattering approximation was used to best-fit the obtained EXAFS signal in the k-space range of 1.5–15 Å^{-1} (Fig. 6.27). To perform EXAFS calculations, one requires the knowledge of the scattering amplitude and phase shift functions for the Pb–S and Pb–Pb atom pairs, which were calculated by the ab initio FEFF8 code [50]. The calculations were performed for the cluster of 8 Å size, centered at absorbing lead atom and having the cubic PbS structure. The inelastic losses were taken into account using the complex exchange-correlation Hedin-Lundqvist potential [22]. The obtained structural parameters, such as the interatomic distances (R) and the mean-square relative displacements (MSRDs) (σ^2), are reported in Table 6.6.

These results reveal the noticeable structure relaxation in nano-PbS. The average distance in nano-PbS between the nearest neighbors (Pb–S_1) becomes smaller by

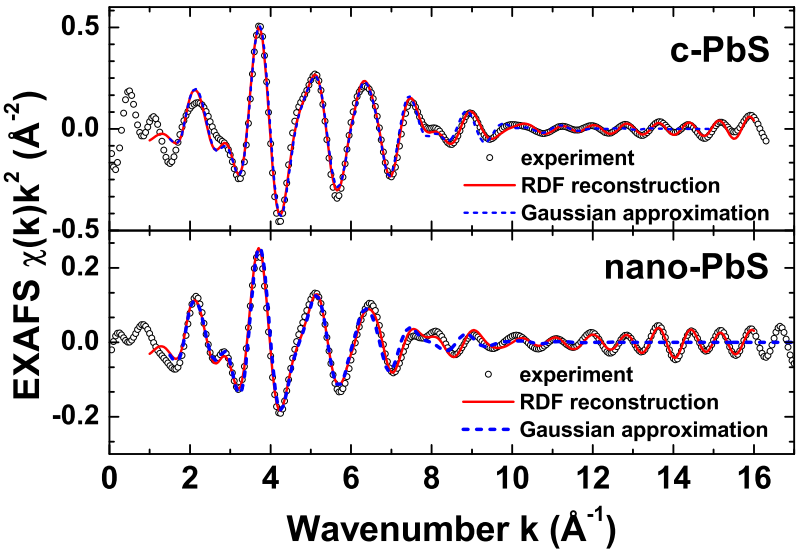

Figure 6.27: Experimental (empty circles) and best fitted Pb L_3-edge EXAFS spectra for the first two coordination shells of Pb. Solid line represents signal from RDF reconstruction and dashed line represents signal using Gaussian approximation.

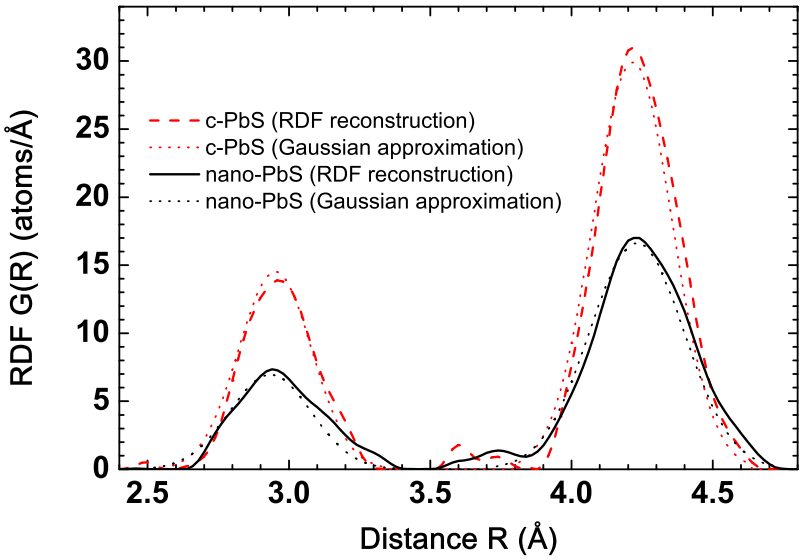

Figure 6.28: Radial distribution function (RDF) reconstruction for c-PbS and nano-PbS obtained using theoretical phases and amplitudes. Dotted lines show RDF approximation with the Gaussian shape obtained by the standard EXAFS fitting procedure for the first two coordination shells.

−0.02 Å and the distance between next neighbors (Pb–Pb_2) increases by +0.01 Å compared with c-PbS. At the same time, we can see significant increase of the mean-square relative displacement (MSRD) values for both coordination shells in nano-PbS compared with c-PbS.

In order to check these results we performed the radial distribution function (RDF) reconstruction, using the method described in Sec. 3.4, without an assumption of any model or shape for the RDF $G(R)$.

RDF reconstruction was done using the same theoretical amplitudes and phases for Pb–S and Pb–Pb atom pairs as those obtained by FEFF8 [50] and used in the standard fitting procedure (Fig. 6.27). As a result, non-Gaussian form of RDFs has been revealed in both c-PbS and nano-PbS (Fig. 6.28). The RDF asymmetry is caused by lone pair $6s^2$ electrons, which are responsible for high polarizability of Pb ions and anharmonic Pb–S interatomic potential. In Fig. 6.28 one can also see a comparison of the reconstructed RDFs with those obtained within the Gaussian approximation. RDF reconstruction confirms the structure relaxation in nano-PbS sample, where the average Pb–S_1 distance decreases, whereas the average Pb–Pb_2 distance slightly increases compared with c-PbS. This effect is similar to that in metal oxides.

6.3.2 Conclusions

Summarizing the results for lead sulfide, we can withdraw the following conclusions.

1. The Pb–S and Pb–Pb bonds in microcrystalline c-PbS and nanosized nano-PbS are largely anharmonic that results in asymmetric shape of peaks in the RDFs.

2. The reduction of PbS nanoparticles size down to ∼3 nm influences significantly the Pb L_3-edge EXAFS spectrum due to an increase in the number of atoms located at the surface relative to that in the bulk of the nanoparticles.

3. A pronounced relaxation of the atomic structure in PbS nanoparticles has been clearly detected. It is responsible for an increase of the static disorder reflected by the mean-square relative displacement (MSRD) parameters and for a change of interatomic distances in the first and second coordination shells of lead atoms.

7

Conclusions

In this thesis we have employed the extended X-ray absorption fine structure (EXAFS) method to study experimentally and using complex modeling approach the phenomenon of atomic structure relaxation upon a decrease of the size of particles down to nanoscale in nickel oxide (NiO), tungstates ($MeWO_4$, Me = Co, Cu) and lead sulfide (PbS).

A recently developed complex modeling approach [23, 24], combining *ab initio* EXAFS calculations [22, 25] with classical molecular dynamics (MD), further referenced as MD-EXAFS, has been adopted to nanomaterials [26, 27]. The advantage of the MD-EXAFS method is a significant reduction of a number of free model parameters, which are required to describe the structure and dynamics of nanoobjects [23, 26]. The only parameters we need are related to the geometry of the nanoobject and to the force-field model used in the molecular dynamics simulations. All interatomic distances, bond angles, thermal and static disorder effects are obtained from MD simulations by calculating configuration averages from snapshots of instant atomic positions.

Here we have used the MD-EXAFS method to reconstruct the structure of nanocrystalline NiO from experimental Ni K-edge EXAFS spectra taking into account the presence of defects, thermal disorder and structure relaxation in nanoparticles [26, 27]. It was found that there is noticeable structure relaxation in nanocrystalline NiO, which results in an expansion of the Ni–Ni distances in the second coordination shell of nickel atoms and in a contraction of the nearest neighbour Ni–O bonds as well as in an increase of the static disorder, evidenced by the mean-square relative displacement (MSRD) parameter. At the same time, the lattice dynamics, also probed by the MSRD, is close in both micro- and nanocrystaline NiO in the temperature range from 10 to 300 K.

It was shown using the MD-EXAFS method that the structure relaxation inside NiO nanoparticles is due to the presence of Ni vacancies [26, 27].

The MD-EXAFS method, based on classical MD and rather simply pair atomic potentials, is not applicable to the materials, whose structure is strongly influenced by the electronic or quantum effects. Therefore, we have employed more conventional analysis scheme to nanocrystaline tungstates and lead sulfide.

The study of the local atomic structure of tungsten and divalent metal atoms in nanocrystalline $MeWO_4$ (Me = Co, Cu) has been performed using the W L_3-edge and Me K-edge EXAFS and Raman spectroscopy. It was found that atomic structure of $MeWO_4$ relaxes compared with microcrystalline phase, leading to large and particular distortion of the WO_6 octahedra. In nanoparticles tungsten atoms have stronger and shorter bonds with the nearest four oxygen atoms, whereas other two oxygens become weakly bound. This result contradicts to the general rule stating that the lattice of nanoparticles gets distorted in such a way that the crystal symmetry tends to increase (size-induced reduction in an asymmetry parameter) [10]. In tungstates we can see that the asymmetry parameter (distortion of the octahedra) increases upon decreasing the size of the particles. It is also shown that the relaxation is affected by the Me^{2+} ion type.

Finally, our Pb L_3-edge EXAFS results indicate strong structure relaxation in nanosized lead sulfide (PbS) compared to microcrystalline PbS. The analysis of radial distribution functions (RDF) for Pb–S and Pb–Pb atom pairs revealed that they have non-Gaussian shape, indicating strong anharmonic Pb–S interaction. We found that the average Pb–S distance in the first coordination shell of lead atoms decreases, but the average Pb–Pb distance in the second coordination shell increases. This effect is similar to that found in NiO.

To conclude, we have demonstrated that x-ray absorption spectroscopy is a suitable tool for the investigation of structure relaxation phenomena in nanosized materials. Moreover, when combined with advanced simulation methods, the technique allows one to obtain additional original information (for example, concentration of vacancies) not accessible within conventional data analysis procedure.

Main theses

1. A method, combining classical molecular dynamics simulations with *ab initio* multiple-scattering EXAFS calculations (MD-EXAFS method), has been extended to the case of nanoparticles. It allows one to account for the effect of nanoparticle size, atomic structure relaxation, thermal disorder and the presence of defects using rather simple force-field model, based on the pair interatomic potentials with a few free parameters. Such approach allows straightforward incorporation of disorder effects into the multiple-scattering formalism and, thus, to perform the analysis of EXAFS spectra beyond the first coordination shell.

2. In nanosized NiO (in powders and thin films) there is noticeable structure relaxation, which results in an expansion of the Ni–Ni_2 bonds and a contraction of the Ni–O_1 bonds as well as an increase of the static disorder probed by the mean-square relative displacement (MSRD). At the same time, the lattice dynamics, also probed by the MSRD, is close in both microcrystaline and nanosized NiO in the temperature range from 10 to 300 K. It was shown using the MD-EXAFS method that the main source of the structure relaxation inside NiO nanoparticles is the presence of Ni vacancies.

3. The atomic structure of nanosized $MeWO_4$ (Me = Co, Cu) relaxes compared with microcrystalline phase, leading to a large and particular distortion of the WO_6 octahedra. Tungsten atoms make stronger and shorter bonds with nearest four oxygen atoms, whereas other two oxygens remain weakly coordinated to tungsten. It is also shown that the relaxation is affected by the Me^{2+} ion type.

Bibliography

[1] S. J. L. Billinge, I. Levin, Science **316**, 516 (2007). xxi, 1, 2, 11, 12

[2] H. J. Wasserman, J. S. Vermaak, Surf. Sci. **22**, 164 (1970). 1, 7

[3] H. J. Wasserman, J. S. Vermaak, Surf. Sci. **32**, 168 (1972). 1, 7

[4] C. W. Mays, J. S. Vermaak, D. Kuhlmann-Wisdorf, Surf. Sci. **12** 134 (1968). xiii, 1, 7, 8

[5] J. S. Vermaak, D. K. Wisdorf, J. Phys. Chem. **72**, 4150 (1968). 1, 7

[6] J. S. Vermaak, C. W. Mays, D. Kuhlmann-Wisdorf, Surf. Sci. **12**, 128 (1968). 1, 7

[7] A. Cimino, P. Porta, M. Valigi, J. Am. Ceram. Soc. **49**, 152 (1966). 1, 9, 41

[8] H. Mitani, H. Nagai, M. Fukuhara, J. Metal. Soc. Jpn. **41**, 27 (1977). 1, 9

[9] K. Uchino, E. Sadanaga, T. Hirose, J. Am. Ceram. Soc. **72**, 1555 (1989). 1, 9

[10] P. Ayyub, V. R. Palkar, S. Chattopadhyay, M. Multani, Phys. Rev. B **51**, 6135 (1995), 1, 9, 90

[11] S. Tsunekawa, K. Ishikawa, Z. Q. Li, Y. Kawazoe, A. Kasuya, Phys. Rev. Lett. **85**, 3440 (2000). 1, 9, 10, 11, 41

[12] M. Fukuhara, Phys. Lett. A **313**, 427 (2003). 1, 11, 41

[13] G. Li, J. Boerio-Goates, B. F. Woodfield, L. Li Appl. Phys. Lett. **85**, 2059 (2004). 1, 10, 11

[14] M. Fernández-García, A. Martínez-Arias, J. C. Hanson, J. A. Rodriguez, Chem. Rev. **104**, 4063 (2004). 2, 7, 12

[15] S. C. Ray, J. W. Chiou, W. F. Pong, M.-H. Tsai, Crit. Rev. Solid State Mater. Sci. **31**, 91 (2006). 2, 12

[16] S. J. L. Billinge, J. Solid State Chem. **181**, 1695 (2008). 2, 12

[17] S. J. L. Billinge, M. G. Kanatzidis, Chem. Commun. **2004**, 749 (2004). 2

[18] A. I. Frenkel, A. Yevick, C. Cooper, R. Vasic, Annu. Rev. Anal. Chem. **4**, 23 (2011). 2, 12

[19] H. Modrow, Appl. Spectroscopy Rev. **39**, 183 (2004). 2, 12

[20] P. A. Lee, P. H. Citrin, P. Eisenberger, B. M. Kincaid, Rev. Mod. Phys. **53**, 769 (1981). 2, 69

[21] G. Dalba, P. Fornasini, R. Grisenti, F. Rocca, D. Comedi, I. Chambouleyron, Appl. Phys. Lett. **74**, 281 (1999). 2

[22] J. J. Rehr, R. C. Albers, Rev. Mod. Phys. **72**, 621 (2000). xiii, 2, 13, 14, 16, 17, 18, 19, 36, 69, 86, 89

[23] A. Kuzmin, R. A. Evarestov, J. Phys.: Condens. Matter **21**, 055401 (2009). 2, 3, 30, 31, 36, 55, 89

[24] A. Kuzmin, R. A. Evarestov, J. Phys.: Conf. Series **190**, 012024 (2009). 2, 3, 30, 31, 89

[25] A. L. Ankudinov, C. E. Bouldin, J. J. Rehr, J. Sims, H. Hung, Phys. Rev. B **65**, 104107 (2002). 2, 19, 25, 28, 29, 89

[26] A. Anspoks, A. Kalinko, R. Kalendarev, A. Kuzmin, Phys. Rev. B **86**, 174114 (2012). 2, 3, 48, 52, 55, 59, 60, 62, 89, 90

[27] A. Anspoks, A. Kalinko, R. Kalendarev, A. Kuzmin, J. Phys.: Conf. Series **430**, 012027 (2013). 2, 3, 48, 55, 60, 62, 89, 90

[28] V. L. Aksenov, M. V. Kovalchuk, A. Yu. Kuzmin, Yu. Purans, S. I. Tyutyunnikov, Crystallogr. Rep. **51**, 908 (2006). 3, 14, 23, 25, 45, 48, 84, 86

[29] M. Newville, B. Ravel, D. Haskel, J. J. Rehr, E. A. Stern, Y. Yacoby, Physica B **208 & 209**, 154 (1995). 3, 29

[30] B. Ravel, M. Newville, J. Synchrotron Rad. **12**, 537 (2005). 3, 29

[31] A. Anspoks, A. Kuzmin, A. Kalinko, J. Timoshenko, Solid State Commun. **150**, 2270 (2010). 3, 33, 48, 55, 59, 68

[32] A. Anspoks, A. Kuzmin, J. Non-Cryst. Solids **357**, 2604 (2011). xiv, 3, 29, 33, 34, 36, 48, 55, 56, 59, 68

[33] A. Kuzmin, Latvian J. Phys. Tech. Sci. **2**, 7 (2006). 4

[34] C. Burda, X. Chen, R. Narayanan, M. A. El-Sayed, Chem. Rev. **105**, 1025 (2005). 7

[35] E. Roduner, Chem. Soc. Rev. **35**, 583 (2006). 7

[36] K. Heinemann, H. Poppa, Surf. Sci. **156**, 265 (1985). 7, 9

[37] S. Giorgio, C. R. Henry, C. Chapon, J. M. Penisson, J. Cryst. Growth **100**, 254 (1990). 7, 9

[38] R. Lamber, S. Wetjen, N. I. Jaeger, Phys. Rev. B **51**, 10968 (1995). 7, 9

[39] T. C. Huang, M. T. Wang, H. S. Sheu, W. F. Hsieh, J. Phys.: Condens. Matter **19**, 476212 (2007). xiii, 8, 10

[40] M. Dubiel, S. Brunsch, W. Seifert, H. Hofmeister, G. L. Tan, Eur. Phys. J. D **16**, 229-232 (2001). 9

[41] V. R. Palkar, P. Ayyub, S. Chattopadhyay, M. Multani, Phys. Rev. B **53**, 2167 (1996). 9, 11

[42] S. Tsunekawa, S. Ito, T. Mori, K. Ishikawa, Z. Q. Li, Y. Kawazoe, Phys. Rev. B **62**, 3065 (2000). 9, 10

[43] L. Li, Y. Su, G. Li, Appl. Phys. Lett. **90**, 054105 (2007). 10

[44] D. Errandonea, F. J. Manjón, M. Somayazulu, D. Häusermann, J. Solid State Chem. **177**, 1087 (2004). 10

[45] V. F. Petrunin, Yu. G. reev, T. N. Miller, Ya. P. Grabis, A. G. Ermolaev, F. M. Zelenyuk, Sov. Powder Metal. Ceram. **23**, 584 (1984) 10

[46] B. E. Warren, *X-ray diffraction*, Dover, New York (1990). 11

[47] B. L. Henke, E. M. Gullikson, J. C. Davis, Atom. Data Nucl. Data, **54**, 181 (1993). 13

[48] M. J. Berger, J. H. Hubbell, S. M. Seltzer, J. Chang, J. S. Coursey, R. Sukumar, D. S. Zucker, K. Olsen, XCOM: Photon Cross Sections Database, http://www.nist.gov/pml/data/xcom/. xiii, 14

[49] E. Fermi, Nuclear Physics, University of Chicago Press (1950). 16

[50] A. L. Ankudinov, B. Ravel, J. J. Rehr, S. D. Conradson, Phys. Rev. B **58**, 7565 (1998). 16, 17, 36, 77, 86, 88

[51] J. J. Rehr, A. L. Ankudinov, Coordin. Chem. Rev. **249**, 131 (2005). 16

[52] P. Fornasini, J. Phys.: Condens. Matter **13**, 7859 (2001). 17, 20

[53] G. Bunker, Nucl. Instrum. Meth. **207**, 437 (1983). 20

[54] P. Fornasini, F. Monti, A. Sanson, J. Synchrotron Radiat. **8**, 1214 (2001). 20

[55] A. Filipponi, A. Di Cicco, M. Benfatto, C.R. Natoli, Europhys. Lett. **13** 319 (1990). 20, 21

[56] A. Kuzmin, Physica B **208-209**, 175 (1995). 21, 23, 25, 27, 28, 45, 84

[57] A. Kuzmin, N. Mironova, J. Phys.: Condens. Matter **10**, 7937 (1998). 25, 55

[58] C. E. Shannon, Proc. IRE, **37**, 10 (1949). 28, 29

[59] H. Nyquist, AIEE Trans. **47**, 617 (1928). 28, 29

[60] A. Kuzmin, J. Phys. IV (France) **7**, C2-213 (1997). 28, 29, 77

[61] A. Kuzmin, J. Purans, J. Phys.: Condens. Matter **12**, 1959 (2000). 29, 77

[62] A. Kuzmin, P. Parent, J. Phys.: Condens. Matter **6**, 4395 (1994). 29

[63] S. Rossano, A. Ramos, J.-M. Delaye, S. Creux, A. Filipponi, Ch. Brouder, G. Calas, Europhys. Lett. **49**, 597 (2000). 30

[64] D. Cabaret, M. Le Grand, A. Ramos, A. M. Flank, S. Rossano, L. Galoisy, G. Calas, D. Ghaleb, J. Non-Cryst. Solids **289**, 1 (2001). 30

[65] A. Witkowska, J. Rybicki, A. Di Cicco, J. Alloy Compd. **401**, 135 (2005). 30

[66] A. Witkowska, J. Rybicki, A. Di Cicco, J. Non-Cryst. Solids **351**, 380 (2005). 30

[67] G. Mountjoy, J. Non-Cryst. Solids **353**, 2029 (2007). 30

[68] P. Kidkhunthod, A. C. Barnes, J. Phys.: Conf. Series **190**, 012076 (2009). 30

[69] F. Jalilehvand, D. Spangberg, P. Lindqvist-Reis, K. Hermansson, I. Persson, M. Sandström, J. Am. Chem. Soc. **123**, 431 (2001). 30

[70] P. J. Merkling, A. Munoz-Paez, J.M. Martinez, R. R. Pappalardo, E. Sanchez Marcos, Phys. Rev. B **64**, 012201 (2001). 30

[71] R. Spezia, M. Duvail, P. Vitorge, T. Cartailler, J. Tortajada, G. Chillemi, P. D'Angelo, M. P. Gaigeot, J. Phys. Chem. A **110**, 13081 (2006). 30

[72] R. Spezia, M. Duvail, P. Vitorge, P. D'Angelo, J. Phys.: Conf. Series **190**, 012056 (2009). 30

[73] A. Witkowska, J. Rybicki, S. De Panfilis, A. Di Cicco, J. Non-Cryst. Solids **352**, 4351 (2006). 30

[74] Y. Okamoto, Nucl. Instrum. Meth. A **526**, 572 (2004). 30

[75] J. Timoshenko, A. Kuzmin, J. Purans, Comp. Phys. Commun. **183**, 1237 (2012). 30

[76] J. Timoshenko, A. Kuzmin, J. Purans, J. Phys.: Conf. Ser. **430**, 012012 (2013). 30

[77] R. Laskowski, J. Rybicki, M. Chybicki, A. Di Cicco, Phys. stat. sol. (b) **217**, 737 (2000). 30

[78] A. Di Cicco, M. Minicucci, E. Principi, A. Witkowska, J. Rybicki, R. Laskowski, J. Phys.: Condens. Matter **14**, 3365 (2002). 30

[79] B. Mierzwa, J. Alloy Compd. **401**, 127 (2005). 30

[80] A. Sanson, Phys. Rev. B **81**, 012304 (2010). 30

[81] O. M. Roscioni, N. Zonias, S. W. T. Price, An. E. Russell, T. Comaschi, C. K. Skylaris, Phys. Rev. B **83**, 115409 (2011). 30

[82] J. Timoshenko, A. Kuzmin, J. Purans, Cent. Eur. J. Phys. **9**, 710 (2011). 30

[83] A. Kuzmin, V. Efimov, E. Efimova, V. Sikolenko, S. Pascarelli, I.O. Troyanchuk, Solid State Ionics **188**, 21 (2011). 30

[84] J. Purans, A. Kuzmin, E. Cazzanelli, G. Mariotto, J. Phys.: Condens. Matter **19**, 226206 (2007). 35

[85] J. D. Gale , A. L. Rohl, Mol. Simulat. **29**, 291 (2003). 35

[86] I. T. Todorov, W. Smith, K. Trachenko, M. T. Dove, J. Mater. Chem. **16**, 1611 (2006). 35

[87] S. A. Makhlouf, F. T. Parker, F. E. Spada, A. E. Berkowitz, J. Appl. Phys. **81**, 5561 (1997). 37

[88] H. Sato, T. Minami, S. Takata, T. Yamada, Thin Solid Films **236**, 27 (1993). 37, 41, 62

[89] O. Kohmoto, H. Nakagawa, Y. Isagawa, A. Chayahara, J. Magn. Magn. Mater. **226**, 1629 (2001). 37, 41, 62

[90] S. Mrowec, Z. Grezesik, J. Phys. Chem. Solids **64**, 1651 (2004). 37, 41

[91] J. Yu, K. M. Rosso, S. M. Bruemmer, J. Phys. Chem. C **116**, 1948 (2012). 37, 41, 62

[92] J. Tang, L. Brzozowski, D. A. R. Barkhouse, X. Wang, R. Debnath, R. Wolowiec, E. Palmiano, L. Levina, A. G. Pattantyus-Abraham, D. Jamakosmanovic, E. H. Sargent, ACS Nano **4**, 869 (2010). 37

[93] G. Huang, Y. Zhu, Mater. Sci. Eng. B **139**, 201 (2007). 37

[94] A. Kalinko, A. Kuzmin, J. Non-Cryst. Solids **357**, 2595 (2011). xviii, 37, 74, 75, 80, 83

[95] K. Rickers, W. Drube, H. Schulte-Schrepping, E. Welter, U. Brüggmann, M. Herrmann, J. Heuer, H. Schulz-Ritter, AIP Conf. Proc. **882**, 905 (2007). 38

[96] C. G. Shull, W. A. Strauser, E. O. Wollan, Phys. Rev. **83**, 333 (1951) 41

[97] W. L. Roth, Phys. Rev. **110**, 1333 (1958). 41

[98] L. C. Bartel, B. Morosin, Phys. Rev. B **3**, 1039 (1971). 41

[99] D. Wang, R. Xu, X. Wang, Y. Li, Nanotechnology **17**, 979 (2006). 41

[100] G. A. Niklasson, C. G. Granqvist, J. Mater. Chem. **17**, 127 (2007). 41, 42, 71

[101] C. Luyo, R. Ionescu, L.F. Reyes, Z. Topalian, W. Estrada, E. Llobet, C.G. Granqvist, P. Heszler, Sensor. Actuator. B **138**, 14 (2009). 41

[102] T.-G. Seong, J.-S. Kim, K.-H. Cho, M. K. Yang, W. Kim, J.-K. Lee, J. W. Moon, J. Roh, S. Nahm, Jpn. J. Appl. Phys. **49**, 121103 (2010). 41

[103] K. M. Kim, D. S. Jeong, C. S. Hwang, Nanotechnology **22**, 254002 (2011). 41

[104] J.M. Slaughter, M. DeHerrera, B.N. Engel, N.D. Rizzo, J. Salter, M. Durlam, R.W. Dave, J. Janesky, B. Butcher, K. Smith, G. Grynkewich, P. IEEE **91**, 703 (2003). 41

[105] H. J. M. Swagten, G. J. Strijkers, P. J. H. Bloemen, M. M. H. Willekens, W. J. M. de Jonge, Phys. Rev. B **53**, 9108 (1996). 41

[106] W. F. Egelhoff, P. J. Chen, C. J. Powell, M. D. Stiles, R. D. McMichael, C.-L. Lin, J. M. Sivertsen, J. H. Judy, K. Takano, A. E. Berkowitz, T. C. Anthony, J. A. Brug, J. Appl. Phys. **79**, 5277 (1996). 41, 42

[107] M.-Y. Cheng, B.-J. Hwang, J. Power Sources **195**, 4977 (2010). 41

[108] C. G. Granqvist, Sol. Energy Mater. Sol. Cells **91**, 1529 (2007). 41

[109] H. Ohta, M. Hirano, K. Nakahara, H. Maruta, T. Tanabe, M. Kamiya, T. Kamiya, H. Hosono, Appl. Phys. Lett. **83**, 1029 (2003). 41

[110] B. O. Jung, Y. H. Kwon, D. J. Seo, D. S. Lee, H. K. Cho, J. Cryst. Growth **370**, 314 (2013). 41

[111] T. Suzuki, Z. Hasan, Y. Funahashi, T. Yamaguchi, Y. Fujishiro, M. Awano, Science **325**, 852 (2009). 41

[112] Z. Grzesik, S. Mrowec, Pol. J. Chem. **79**, 907 (2005). 41, 62

[113] L. Li, L. Chen, R. Qihe, G. Li, Appl. Phys. Lett. **89**, 134102 (2006). xv, 41, 42, 53, 59, 62

[114] M. Ghosh, K. Biswas, A. Sundaresan, C. N. R. Rao, J. Mater. Chem. **16**, 106 (2006). xv, 41, 42, 53, 59

[115] X. G. Zheng, H. Kubozono, H. Yamada, K. Kato, Y. Ishiwata, C. N. Xu, Nature Nanotech. **3**, 724 (2008). xv, 41, 42, 52, 53, 59

[116] S. A. Makhlouf, M. A. Kassem, M. A. Abdel-Rahim, J. Mater. Sci. **44**, 3438 (2009). xv, 41, 42, 53, 59

[117] A. G. McKale, G. S. Knapp, S. K. Chan, Phys. Rev. B **33**, 841 (1986). 42

[118] A. Kuzmin, N. Mironova, J. Purans, A. Rodionov, J. Phys.: Condens. Matter **7**, 9357 (1995). 42

[119] R. V. Vedrinskii, V. L. Kraizman, A. A. Novakovich, Sh. M. Elyafi, S. Bocharov, Th. Kirchner, G. Dräger, Phys. statṡol. (b) **226**, 203 (2001). 42, 46

[120] J. A. Rodriguez, J. C. Hanson, A. I. Frenkel, J. Y. Kim, M. Perez, J. Amer. Chem. Soc. **124**, 346 (2002). 42

[121] P. Luches, E. Groppo, C. Prestipino, C. Lamberti, C. Giovanardi, F. Boscherini, Nucl. Instr. Meth. Phys. Res. B **200**, 371 (2003). 42

[122] P. Luches, E. Groppo, S. DAddato, C. Lamberti, C. Prestipino, S. Valeri, F. Boscherini, Surf. Sci. **566-568**, 84 (2004). 42

[123] E. Groppo, C. Prestipino, C. Lamberti, R. Carboni, F. Boscherini, P. Luches, S. Valeri, S. D'Addato, Phys. Rev. B **70**, 165408 (2004). 42

[124] A. Kuzmin, J. Purans, A. Rodionov, J. Phys.: Condens. Matter **9**, 6979 (1997). 43, 46

[125] E. Avendaño, A. Kuzmin, J. Purans, A. Azens, G. A. Niklasson, C. G. Granqvist, Phys. Scripta **T115**, 464 (2005). 43

[126] W. L. Jang, Y. M. Lu, W. S. Hwang, T.-L. Hsiung, H. P. Wang, Appl. Phys. Lett. **94**, 062103 (2009). 43, 62, 64

[127] W. L. Jang, Y. M. Lu, W. S. Hwang, C. L. Dong, P. H. Hsieh, C. L. Chen, T. S. Chan, J. F. Lee, Europhys. Lett. **96**, 37009 (2011). 43

[128] Y. Hattori, T. Konishi, K. Kaneko, Chem. Phys. Lett. **355**, 37 (2002). 43

[129] C. T. Meneses, W. H. Flores, J. M. Sasaki, Chem. Mater. **19**, 1024 (2007). 44

[130] S. Mandal, S. Banerjee, K. S. R. Menon, Phys. Rev. B **80**, 214420 (2009). 44, 64

[131] P. Kizler, Phys. Rev. B **46**, 10540 (1992). 46

[132] J. P. Hill, C.-C. Kao, D. F. McMorrow, Phys. Rev. B **55**, R8662 (1997). 46

[133] H. Modrow, S. Bucher, J. J. Rehr, A. L. Ankudinov, Phys. Rev. B **67**, (2003) 035123. 46

[134] Z. Y. Wu, D. C. Xian, T. D. Hu, Y. N. Xie, Y. Tao, C. R. Natoli, E. Paris, A. Marcelli, Phys. Rev. B **70**, 033104 (2004). 46

[135] A. Kuzmin, J. Purans, R. Kalendarev, Phys. Status Solidi (c) **72**, 665 (2005). 46

[136] C. Gougoussis, M. Calandra, A. Seitsonen, Ch. Brouder, A. Shukla, F. Mauri, Phys. Rev. B **779**, 045118 (2009). 46

[137] D. Rodic, V. Spasojevic, V. Kusigerski, R. Tellgren, H. Rundlof, Phys. stat. sol. (b) **218**, 527 (2000). 48

[138] M. Vaccari, P. Fornasini, J. Synchrotron Radiat. **13**, 321 (2006). 51

[139] H. X. Gao, L. M. Penga, J. M. Zuo, Acta Cryst. A **55**, 1014 (1999). 51

[140] T. Okazawa, Y. Nakagawa, Y. Kido, Phys. Rev. B **69**, 125412 (2004). 52

[141] B. Bergman, J. Ågren, J. Am. Ceram. Soc. **68**, 444 (1985). 52

[142] J. A. Hoffmann, A. Paskin, K. J. Tauer, R. J. Weiss, J. Phys. Chem. Solids **1**, 45 (1956). 52

[143] C. A. J. Fisher, Scr. Mater. **50**, 1045 (2004). 56

[144] J. Nowotny, A. Sadowski, J. Am. Ceram. Soc. **62**, 24 (1979). 62

[145] P. Lunkenheimer, A. Loidl, C. R. Ottermann, K. Bange, Phys. Rev. B **44**, 5927 (1991). 62

[146] A. M. Ferrari, C. Pisani, J. Chem. Phys. **127**, 174711 (2007). 62, 64

[147] S. Park, H.-S. Ahn, C.-K. Lee, H. Kim, H. Jin, H.-S. Lee, S. Seo, J. Yu, S. Han, Phys. Rev. B **77**, 134103 (2008). 62, 64

[148] H. Grassmann, H.G. Moser, E. Lorenz, J. Lumin. **33**, 21 (1985). 71

[149] V. V. Laguta, M. Nikl, S. Zazubovich, IEEE T. Nucl. Sci. **55**, 1275 (2008). 71

[150] D. L. Stern, R. K. Grasselli, J. Catal. **167**, 570 (1997). 71

[151] D.G. Barton, S.L. Soled, E. Iglesia, Top. Catal. **6**, 87 (1998). 71

[152] V. Dusastre, D. E. Williams, J. Mater. Chem. **9**, 965 (1999). 71

[153] G. Eranna, B. C. Joshi, D. P. Runthala, R. P. Gupta, Crit. Rev. Solid State **29**, 111 (2004). 71

[154] A. A. Kaminskii, H. J. Eichler, K. Ueda, N.V. Klassen, B.S. Redkin, L.E. Li, J. Findeisen, D. Jaque, J. García-Sole, J. Fernández, R. Balda, Appl. Optics **38**, 4533 (1999). 71

[155] T. T. Basiev, A. A. Sobol, Yu. K. Voronko, P. G. Zverev, Opt. Mater. **15**, 205 (2000). 71

[156] S. H. Yang, F. S. Tsai, J. X. Chen, J. Solid State Electr. **14**, 937 (2010). 71

[157] C.G. Granqvist, Sol. Energy Mater. Sol. Cells **60**, 201 (2000). 71

[158] A. Kuzmin, R. Kalendarev, A. Kursitis, J. Purans, J. Non-Cryst. Solids **353**, 1840 (2007). 71

[159] A. W. Sleight, Acta Cryst. B **28**, 2899 (1972). 71, 72

[160] H. Weitzel, Solid State Commun. **8**, 2071 (1970). 72

[161] A. D. Walkingshaw, N. A. Spaldin, E. Artacho, Phys. Rev. B **70**, 165110 (2004). 72

[162] A. Kuzmin, A. Kalinko, R. Evarestov, Acta Mater. **61**, 371 (2013). 72, 76, 82

[163] J. Ruiz-Fuertes, D. Errandonea, R. Lacomba-Perales, A. Segura, J. González, F. Rodríguez, F. J. Manjón, S. Ray, P. Rodríguez-Hernández, A. Muñoz, Z. Zhu, C. Y. Tu, Phys. Rev. B **81**, 224115 (2010). 72, 82

[164] J. Ruiz-Fuertes, A. Friedrich, J. Pellicer-Porres, D. Errandonea, A. Segura, W. Morgenroth, E. Haussühl, C.-Y. Tu, A. Polian, Chem. Mater. **23**, 4220 (2011). 72, 82

[165] J. Ruiz-Fuertes, A. Segura, F. Rodríguez, D. Errandonea, M. N. Sanz-Ortiz, Phys. Rev. Lett. **108**, 166402 (2012). 72, 82

[166] P. F. Schofield, K. S. Knight, S. A. T. Redfern, G. Cressey, Acta Cryst. B **53**, 102 (1997). 72

[167] A. Kuzmin, J. Purans, J. Phys.: Condens. Matter **5**, 267 (1993). 72

[168] A. Kuzmin, J. Purans, R. Kalendarev, Ferroelectrics **258**, 21 (2001). 72

[169] A. Kuzmin, J. Purans, Radiat. Meas. **33**, 583 (2001). 72, 74

[170] A. Kuzmin, A. Anspoks, A. Kalinko, J. Timoshenko, J. Phys.: Conf. Ser. **430**, 012109 (2013). 72

[171] A. Kuzmin, J. Purans, R. Kalendarev, D. Pailharey, Y. Mathey, Electrochim. Acta **46**, 2233 (2001). 72, 75

[172] A. Kalinko, A. Kuzmin, J. Lumin. **129**, 1144 (2009). 74, 75, 81

[173] A. Kalinko, A. Kuzmin, R. A. Evarestov, Solid State Commun. **149**, 425 (2009). 74

[174] A. Kalinko, A. Kotlov, A. Kuzmin, V. Pankratov, A. I. Popov, L. Shirmane, Centr. Eur. J. Phys. **9**, 432 (2011). 74, 75

[175] J. B. Forsyth, C. Wilkinson, J. Phys.: Condens. Matter **6**, 3073 (1994). 75, 77, 80, 81

[176] H. Weitzel, Z. Kristallogr. **144**, 238 (1976). 75, 77, 80, 81

[177] D. M. Trots, A. Senyshyn, L. Vasylechko, R. Niewa, T. Vad, V. B. Mikhailik, H. Kraus, J. Phys.: Condens. Matter **21**, 325402 (2009). 75, 77, 80, 81

[178] P. F. Schofield, K. S. Knight, G. Cressey, J. Mater. Sci. A **31** 2873 (1996). 75, 77, 80, 81

[179] J. B. Forsyth, C. Wilkinson, A. I. Zvyagin, J. Phys.: Condens. Matter **3**, 8433 (1991). 75, 77, 80, 81

[180] A. Kuzmin, A. Kalinko, R. A. Evarestov, Centr. Eur. J. Phys. **9**, 502 (2011). 76

[181] Y. Liu, H. Wang, G. Chen, Y. D. Zhou, B. Y. Gu, B. Q. Hu, J. Appl. Phys. **64**, 4651 (1988). 76

[182] H. Wang, F. D. Medina, Y. D. Zhou, Q. N. Zhang, Phys. Rev. B **45**, 10356 (1992). 76

[183] M. F. Daniel, B. Desbat, J. C. Lassegues, B. Gerand, M. Figlarz, J. Solid State Chem. **67**, 235 (1987). 76, 81

[184] A. Kuzmin, V. Pankratov, A. Kalinko, A. Kotlov, L. Shirmane, A. I. Popov, J. Phys. Conf. Ser. (accepted) (2013). xviii, 80

[185] M. Kunz, I. Brown, J. Solid State Chem. **115**, 395 (1995). 82

[186] S. M. Montemayor, A. F. Fuentes, Ceram. Int. **30**, 393 (2004). 83

[187] P. Schmitt, N. Brem, S. Schunk, C. Feldmann, Adv. Funct. Mater. **21**, 3037 (2011). 83

[188] Y. Zhang, X. Ke, C. Chen, J. Yang, P. R. C. Kent, Phys. Rev. B **80**, 024304 (2009). 83

[189] R. B. Schoolar, J. R. Dixon, Phys. Rev. **137**, A667 (1965). 83

[190] S. A. McDonald, G. Konstantatos, S. Zhang, P. W. Cyr, E. J. D. Klem, L. Levina, E. H. Sargent, Nature Materials **4**, 138 (2005). 83

[191] Z. Wang, B. A. Bunker, Phys. Rev. B **46**, 11277 (1992). 83

[192] A. Lebedev, I. Sluchinskaya, I. Munro, J. Synchrotron Rad. **8**, 800 (2001). 83

[193] Y. Hashimoto, N. Yamaguchi, M. Takaoka, K. Shiota, Sci. Total Environ. **409**, 1001 (2011). 83

[194] I. Moreels, K. Lambert, D. Smeets, D. De Muynck, T. Nollet, J. C. Martins, F. Vanhaecke, A. Vantomme, C. Delerue, G. Allan, Z. Hens, ACS Nano **3**, 3023 (2009). 84

[195] I. Kang, F. W. Wise, J. Opt. Soc. Am. B **14**, 1632 (1997). xviii, 84

Author's publication list

Main publications:

1. **A. Anspoks**, A. Kalinko, R. Kalendarev, A. Kuzmin, **Atomic structure relaxation in nanocrystalline NiO studied by EXAFS spectroscopy: Role of nickel vacancies.** *Physical Review B* **86** (2012) 174114:1-11.

2. **A. Anspoks**, A. Kalinko, R. Kalendarev, A. Kuzmin, **Local structure relaxation in nanocrystalline $Ni_{1-x}O$ thin films.** *Thin Solid Films* **553** (2013) 58-62

3. **A. Anspoks**, A. Kuzmin, **Interpretation of the Ni K-edge EXAFS in nanocrystalline nickel oxide using molecular dynamics simulations.** *Journal of Non-Crystalline Solids* **357** (2011) 2604-2610.

4. **A. Anspoks**, A. Kuzmin, A. Kalinko, J. Timoshenko, **Probing NiO nanocrystals by EXAFS spectroscopy.** *Solid State Communications* **150** (2010) 2270-2274.

5. **A. Anspoks**, A. Kalinko, R. Kalendarev, A. Kuzmin, **Probing vacancies in NiO nanoparticles by EXAFS and molecular dynamics simulations.** *Journal of Physics: Conference Series* **430** (2013) 012027:1-4.

6. A. Kuzmin, **A. Anspoks**, A. Kalinko, J. Timoshenko, **Effect of cobalt doping on the local structure and dynamics of multiferroic $MnWO_4$ and $Mn_{0.7}Co_{0.3}WO_4$.** *Journal of Physics: Conference Series* **430** (2013) 012109:1-4.

7. **A. Anspoks**, A. Kalinko, P. Kulis, A. Kuzmin, B. Polyakov, J. Timoshenko, **X-ray absorption spectroscopy study of the local atomic structure in PbS nanocrystals.** *Journal of Physics: Conference Series* (2013), accepted.

8. A. Kuzmin, **A. Anspoks**, A. Kalinko, J. Timoshenko, **Influence of thermal and static disorder on the local atomic structure in $CuWO_4$.** *Journal of Physics: Conference Series* (2013), accepted.

9. **A. Anspoks**, A. Kalinko, J. Timoshenko, A. Kuzmin, **Local structure relaxation in nanosized tungstates**, *Solid State Communications* **183** (2014) 22-26

Related publications:

1. A. Kalinko, A. Kuzmin, **A. Anspoks**, J. Timoshenko, R. Kalendarev, **EXAFS study of antiperovskite-type copper nitride.** *Journal of Physics: Conference Series* (2013), accepted.

2. **A. Anspoks**, D. Bocharov, J. Purans, F. Rocca, A. Sarakovskis, V. Trepakov, A. Dejneka, M Itoh, **Local structure studies of $SrTi^{16}O_3$ and $SrTi^{18}O_3$.** *Physica Scripta* **89** (2014) 044002

3. J. Timoshenko, **A. Anspoks**, A. Kalinko, A. Kuzmin, **Analysis of EXAFS data from copper tungstate by reverse Monte Carlo method**, *Physica Scripta* **89** (2014) 044006

4. A. Kuzmin, **A. Anspoks**, A. Kalinko, J. Timoshenko, R. Kalendarev, **EXAFS spectroscopy and first-principles study of $SnWO_4$**, *Physica Scripta* **89** (2014) 044005

Participation in conferences

1. **A. Anspoks**, A. Kuzmin, A. Kalinko, J. Timoshenko, **Probing NiO nanocrystals by EXAFS spectroscopy**, International Baltic Sea Region Conference 'Functional Materials and Nanotechnologies' (FM&NT), 2010, Riga, Latvia.

2. **A. Anspoks**, A. Kuzmins, A. Kalinko, **NiO nanokristālu struktūras relaksācijas pētījumi ar EXAFS** ISSP 27th Scientific Conference, 2011, Riga, Latvia.

3. **A. Anspoks**, R. Kalendarev, A. Kuzmin, **Structure, morphology and dynamics of $Ni_{1-x}O$ thin films**, International Baltic Sea Region Conference 'Functional Materials and Nanotechnologies' (FM&NT), 2011, Riga, Latvia.

4. **A. Anspoks**, A. Kuzmins, A. Kalinko, **Local structure relaxation and lattice dynamics in polycrystalline and nanocrystalline NiO**, International Baltic Sea Region Conference 'Functional Materials and Nanotechnologies' (FM&NT), 2011, Riga, Latvia.

5. **A. Anspoks**, A. Kuzmins, A. Kalinko, **Nanokristālu struktūras pētījumi ar EXAFS**, ISSP 28th Scientific Conference, 2012, Riga, Latvia.

6. **A. Anspoks**, A. Kalinko, P. Kulis, A. Kuzmin, B. Polakov, J. Timoshenko, **X-ray absorption spectroscopy of the local atomic structure in PbS quantum dots**, International Baltic Sea Region Conference 'Functional Materials and Nanotechnologies' (FM&NT), 2012, Riga, Latvia.

7. **A. Anspoks**, A. Kalinko, A. Kuzmin, J. Timoshenko, **X-ray absorption spectroscopy of local structure and lattice dynamics in multiferroic $MnWO_4$**

and $Mn_{1-c}Co_cWO_4$, International Baltic Sea Region Conference 'Functional Materials and Nanotechnologies' (FM&NT), 2012, Riga, Latvia.

8. **A. Anspoks**, A. Kalinko, R. Kalendarev, A. Kuzmin, **Probing vacancies in NiO nanoparticles by EXAFS and molecular dynamics simulations**, The 15th International Conference on X-ray Absorption Fine Structure (XAFS15), 2012, Beijing, China.

9. **A. Anspoks**, D. Bocarovs, J. Purans, F. Rocca, V. Trepakov, **Local structure analysis of $SrTiO_3$ and $SrTi^{18}O_3$ by x-ray absorption spectroscopy**, ISSP 29th Scientific Conference, 2012, Riga, Latvia.

10. **A. Anspoks**, D. Bocarovs, J. Purans, F. Rocca, A. Sarakovskis, V. Trepakov, **X-ray absorption spectroscopy and second harmonic generation analysis of $SrTi^{18}O_3$**, ISSP 29th Scientific Conference, 2012, Riga, Latvia.

11. **A. Anspoks**, A. Kalinko, A. Kuzmin, J. Timoshenko, **Local structure studies of $SrTiO_3$ and $SrTi^{18}O_3$**, International Baltic Sea Region Conference 'Functional Materials and Nanotechnologies' (FM&NT), 2013, Tartu, Estonia.

12. **A. Anspoks**, A. Kalinko, R. Kalendarev, A. Kuzmin, **Local structure relaxation in nanocrystalline NiO thin films**, European Materials Research Society (E-MRS) 2013 Spring Meeting, Strasbourg, France.

Participation in schools with posters

1. **A. Anspoks**, R. Kalendarev, A. Kuzmin, **Structure, morphology and dynamics of $Ni_{1-x}O$ thin films**, X. Research Course on New X-ray Sciences "Ultrafast X-ray science", March 28-31, 2011, Hamburg, Germany.

2. **A. Anspoks**, A. Kuzmins, A. Kalinko, **Local structure relaxation and lattice dynamics in polycrystalline and nanocrystalline NiO**, PSI Summer School 2011 - Phase Transitions, August 14-22, 2011, Zug, Switzerland.

3. **A. Anspoks**, A. Kalinko, A. Kuzmin, J. Timoshenko, **Local structure and lattice dynamics in multiferroic $MnWO_4$ and $Mn_{1-c}Co_cWO_4$**, 5th European School on Multiferroics (ESMF 5), January 29 - February 3, 2012, Monte Verita, Switzerland.

4. **A. Anspoks**, A. Kalinko, P. Kulis, A. Kuzmin, B. Polakov, J. Timoshenko, **EXAFS spectroscopy of the local environment in PbS quantum dots**, First Baltic School on Application of Neutron and Synchrotron Radiation in Solid State Physics and Material Science (BSANS-2012), October 1-4, 2012, Riga, Latvia.